

**A STUDY OF HYBRID SOLAR PHOTOVOLTAIC AND
THERMOELECTRIC ENERGY GENERATION IN THE
LAKE VICTORIA ENVIRONMENT**

GIDEON GUYO KIDEGHO

**DOCTOR OF PHILOSOPHY
(Energy Technology)**

**JOMO KENYATTA UNIVERSITY OF
AGRICULTURE AND TECHNOLOGY**

2022

**A study of hybrid solar photovoltaic and thermoelectric energy
generation in the Lake Victoria environment**

Gideon Guyo Kidegho

**A Thesis Submitted in Partial Fulfilment of the Requirements for the
Degree of Doctor of Philosophy in Energy Technology of the Jomo
Kenyatta University of Agriculture and Technology**

2022

DECLARATION

This thesis is my original work and has not been presented for a degree in any other University

Signature.....Date.....

Name: Gideon Guyo Kidegho

This thesis has been submitted for examination with our approval of my university supervisors

Signature.....Date.....

Prof. Robert Kinyua, PhD

JKUAT, Kenya

Signature.....Date.....

Prof. Christopher Maina Muriithi, PhD

MUT, Kenya

DEDICATION

This work is dedicated to my family; wife Margaret Njeghe Kidegho, my son Samuel Guyo, son Gabriel Peter Pelu and daughter Olive Machocho for their patience and understanding during the entire research period. May all the Glory be to my God JEHOVAH.

In memory, I remember my late father Dishan Mwasagua Guyo, Sisters Judith Gombe Bosire and Serah Nzighe, my grandmother Mercy Gombe Kidegho, step-mother Judith Nacharo Guyo and My Mother Olive Machocho Guyo who are not able to witness this God ordained success. I miss them in this celebration.

ACKNOWLEDGEMENTS

I would like to acknowledge the priceless guidance, assistance and encouragement provided by my supervisors; Professor Robert Kinyua and Professor Christopher Muriithi during the research period and development of this thesis document. I also would like to recognize the Technical University of Mombasa for funding my studies and the Jomo Kenyatta University of Agriculture and Technology and VicInAqua project for facilitating the study.

I also acknowledge the support by Dr. Francis Njoka and the entire staff of the Institute of Environmental and Energy Technology at JKUAT for according me a good working environment. Not to forget the Ministry of fisheries in Kisumu for their assistance in data collection.

This work was supported by the European Union's Horizon 2020 research and innovation program under grant agreement No 689427.

TABLE OF CONTENTS

DECLARATION.....	ii
DEDICATION.....	iii
ACKNOWLEDGEMENTS.....	iv
TABLE OF CONTENTS.....	v
LIST OF TABLES	xi
LIST OF FIGURES	xii
LIST OF SYMBOLS	xvii
LIST OF APPENDICES	xviii
ACRONYMS AND ABBREVIATIONS.....	xix
ABSTRACT.....	xxiii
CHAPTER ONE	1
INTRODUCTION.....	1
1.1 Background of the study.....	1
1.1.1 Solar Photovoltaic Power Generation Technology in Kenya.....	2
1.1.2 Use of Thermoelectric Technology in Power Generation.....	2
1.2 Statement of the problem.....	3
1.3 Justification of the study.....	4

1.4 Objectives	6
1.4.1 Objective	6
1.4.2 Specific objectives.....	6
1.5 Research Questions.....	6
1.6 Scope of Study	7
1.8 Thesis Structure	7
CHAPTER TWO	9
LITERATURE REVIEW.....	9
2.1 Introduction:	9
2.2 Solar Photovoltaic Power Generation Technology in Kenya.....	10
2.3 Solar Photovoltaic Power Generation Technology.....	11
2.3.1 PV cell technology	11
2.3.2 Temperature effects on the performance of the solar cell.....	12
2.3.3 Mitigation of the negative effects of temperature	15
2.4 The thermoelectric technology	27
2.4.1 Thermoelectric technology in waste heat recovery.....	35
2.4.2 Thermoelectric technology use in photovoltaic systems.....	37

2.5 Effects of temperature mismatch in hybrid TEG systems and mitigation methods	40
2.6 Summary of Gaps	44
CHAPTER THREE	46
METHODS AND MATERIALS	46
3.1 Preliminary Data Collection at JKUAT –IEET for PV-TEG Hybrid System Development	46
3.1.1 Introduction:	46
3.1.2 Weather Monitoring Station Setup.....	47
3.1.3 Specific Setups for PV Temperature and Voltage Measurement.....	49
3.1.3.1 PV Module Characterization	49
3.2 Site Studies for Design of the PV-TEG Hybrid System to Run the Autonomous Aquaculture System	55
3.2.1 Introduction	55
3.2.2 Instruments Sensors Components and Fixtures.....	56
3.2.3 Weather Monitoring Station Setup in Kisumu	57
3.2.4 Specific Setups for PV Temperature and Voltage Measurement.....	60
3.3 TEG Modeling and Test Bench Fabrications	63
3.3.1. Introduction	63

3.3.2 TEG Numerical Model Development	63
3.3.2.2 The Electric Model of a TEG	65
3.3.2.3 The Thermal Model of a TEG.....	69
3.3.2.4 Model Development and Simulation.....	71
3.3.2.5 Model Development Assumptions	74
3.3.3 TEG Bench Setup Fabrication.....	75
3.3.4 Field PV-TEG Power System Design	77
3.4 Evaluation of Thermal Interface Materials in Mediating PV Cell Temperature Mismatch in PV-TEG Power Generation Systems	80
3.4.1 Introduction	80
3.4.2 PV-TEG System Model and Governing equations	80
3.4.3 Simulation and Experimental Procedures	84
3.4.4 PV Module Preliminary Cell Mapping and Temperature Measurement Setup	86
3.4.5 Systematic Solar PV Cell Temperature Measurements Setups under TIMs	88
3.4.6 PV-TEG Temperature and Voltage Measurements under TIMs	89
3.5 Economic Analysis and Viability of the PV-TEG Hybrid System.....	92
3.5.1 Introduction	92

3.5.2 PV-TEG System Materials and Cost Analysis.....	93
3.5.3 System Economic Analysis.....	94
CHAPTER FOUR.....	96
RESULTS AND DISCUSSIONS	96
4.1 Preliminary Data Collection at JKUAT –IEET for PV-TEG Hybrid System	96
4.3 TEG Modeling and Test Bench Fabrications	107
4.3.1 Model Validation and Simulation Outcomes	107
4.3.2 Bench Setups Outcomes.....	109
4.3.3 Final System Design Implications.....	112
4.4 Evaluation of Thermal Interface Materials in Mediating PV Cell Temperature Mismatch in PV-TEG Power Generation	112
4.4.1 Numerical Analytical Solution and Preliminary PV Module Cell Temperature Measurement	113
4.4.2 Systematic PV Cell Temperature Measurement under TIMs	115
4.4.3 PV cell temperature and TEG voltage measurements under TIMs.....	118
4.5 Economic Analysis of the PV-TEG Hybrid System.....	125
CHAPTER FIVE.....	127
CONCLUSIONS AND RECOMMENDATIONS TO FURTHER WORK.....	127
5.1 Conclusions.....	127

5.1.1 Data Collection at JKUAT –IET for PV-TEG Hybrid System Development.....	127
5.1.2 Site Studies for Design of the PV-TEG Hybrid System to Run the Autonomous Aquaculture System	128
5.1.3 TEG Modeling and Test Bench Fabrications	129
5.1.4 Evaluation of Thermal Interface Materials in Mediating PV Cell Temperature Mismatch in PV-TEG Power Generation Systems	129
5.1.5 Economic Analysis and Viability of the PV-TEG Hybrid System	130
5.2 Recommendations for Future Work	131
REFERENCES	132
APPENDICES	146

LIST OF TABLES

Table 1.1: Feed-in-Tariffs policy for wind, biomass, small hydro's, geothermal, biogas and solar.....	2
Table 3.1: List of Instruments, Sensors and Devices	56
Table 3.2: Internal Parameters of a TEG Module	66
Table 3.3: External parameters of a TEG module.....	66
Table 3.4: The RAS electrical load	78
Table 3.5: Illustration of Models for Determination of PV Cell Temperature (Jakhrani A.Q et al., 2011).....	86
Table 3.6: Component Technical Specifications and Cost	93
Table 4.1: Summary of Results	103
Table 4.2: Bare cell matrix temperature variance	115

LIST OF FIGURES

Figure 1.1: Thesis structure flow chart.....	8
Figure 2.1: (a) I-V and (b) P-V Characteristics of a PV Module at constant irradiance of 1000 W/m ² (Razak et al., 2016)	15
Figure 2.2: Cooling system for solar panels of residential applications – (Peng et al., 2017b).....	17
Figure 2.3: Fabrication of the heat spreader and cotton wick structures for cooling PV cells (Chandrasekar & Senthilkumar, 2015).....	19
Figure 2.4: Back view of the PV setup (left) PV + PCM (top right) PV + Fin (bottom right) Reference PV (Bayrak et al., 2020)	21
Figure 2.5: Micro –channel heat sink setup (a) Schematic of the module parts (b) Thermocouple locations on test points (Al Siyabi et al., 2018).....	22
Figure 2.6: Cross-section of an optical water filter for PV modules (Al-Shohani et al., 2016).....	25
Figure 2.7: 4MW Tracking type floating system Jamestown Australia (Divya Mittal et al., 2017)	27
Figure 2.8: Schematic diagram of a thermoelectric generator pellet (Y. Deng et al., 2013).....	29
Figure 2.9: Voltage Current (IV) and Voltage Power (VP) characteristic curves of a TEG (Montecuccio et al., 2014)	30

Figure 2.10: A Roadmap for the exploitation of thermoelectric technology, where ZT is the thermoelectric figure of merit and Z the efficiency (Robert Freer & Anthony V. Powell, 2019)	33
Figure 2.11: Schematic of waste heat recovery using TEG technology (Enescu, 2019).....	35
Figure 2.12: TEG integration into the exhaust system of the BMW X 6 prototype model (Zoui et al., 2020).	37
Figure 2.13: Efficiency of PV-TE as a function of concentrating ratio: (a) c-Si PV, (b) p-Si TFPV, (c) polymer PV, (d) CIGS. (J. Zhang et al., 2014).	39
Figure 2.14: Correlation of load line and output power of TEMs. The virtual load line can be controlled by DC-DC converter (H. Nagayoshi & T. Kajikawa, 2006)	43
Figure 3.1: The CMP-3 Pyranometer on the IEET building roof	48
Figure 3.2: Schematic of the Weather Station data logging setup	48
Figure 3.3: Characterization of the PV Modules	50
Figure 3.4: PV Module Temperature Measurement under Air Cooling	51
Figure 3.5: PV Module Temperature and Voltage Measurement.....	51
Figure 3.6: PV Module Temperature and Voltage Measurement.....	52
Figure 3.7: Battery Charging Voltage and Current Measurement	53
Figure 3.8: Battery Loading Lighting Bank.....	54

Figure 3.9: Battery Charging PV Temperature, Voltage and Current Measurement	54
Figure 3.10: Water Pool on site Kisumu.....	57
Figure 3.11: CMP-3 Pyranometer in Nyalenda Kisumu.....	58
Figure 3.12: COMBILOG 1022 Logger in Nyalenda Kisumu	59
Figure 3.13: PV Module Temperature Measurement	59
Figure 3.14:. PV Parameter Measurements (a) Air (b) Water cooled.....	61
Figure 3.15:. PV Module Temperature and Voltage Measurements	62
Figure 3.16. PV Module Temperature and Voltage Measurements.....	62
Figure 3.17: Thermoelectric Generator model block diagram.....	65
Figure 3.18: Thermoelectric Generator Physical Structure	66
Figure 3.19: Thermoelectric Generator PN Pellet Structure.....	71
Figure 3.20: TEG Simulation State Flowchart.....	73
Figure 3.21: Schematic TEG Block-Set Model in MATLAB Simulink.....	74
Figure 3.22: TEG Electrical Connection Schematic	76
Figure 3.23: Laboratory TEG setups; (a) single, (b) two and (c) four TEGs.....	76
Figure 3.24: Schematic representation of the electrical connection of the TEG Modules: a) One, b) Two, and c) Four TEG Modules	77

Figure 3.25: A schematic of an electrical-thermal connector in PV and TEG System (Concept adopted from (Fisac et al., 2014))	81
Figure 3.26: A schematic of equivalent TEG Cell.....	82
Figure 3.27: Cell mapping on the 36 Cell 13 Wp PV Module.....	87
Figure 3.28: Cell mapping and temperature distribution measurements; (a) PV cell mapping, (b) Thermocouple placement.....	88
Figure 3.29: Systematic temperature distribution measurements using various TIMs; (a) Graphite (b) Heat spreader (c) Aluminum foil (d) Complete setup of the three sets.	89
Figure 3.30: Air cooled PV-TEG setups (a) graphite (b) heat spreader (c) aluminum foil (d) bare cells (e) TEGs mounted (f) Complete setup.....	91
Figure 3.31: Water cooled PV-TEGs setups for the three TIMs and the reference case	92
Figure 4.1: Open circuit voltage characterization.....	97
Figure 4.2: PV cell temperature and open circuit voltage both air cooled.....	98
Figure 4.3: PV cell temperature and open circuit voltage air cooled and water cooled	99
Figure 4.4: PV cell temperature and open circuit voltage air cooled and water cooled	101
Figure 4.5: PV cell temperature and Battery Charging DC Power output.....	102
Figure 4.6: Nyalenda Kisumu Annual Weather Pattern and Irradiation.....	104

Figure 4.7: Roof Mount PV Temperature Measurements.....	105
Figure 4.8: Roof Mount PV Voltage Measurements	106
Figure 4.9: 275 Wp PV Ground Mount Temperature and Voltage Measurements	107
Figure 4.10: Validation of present work; (a) Voltage, (b) Current, (c) Power and (d) Efficiency.....	109
Figure 4.11: TEG Bench Setup output measurements; (a) Voltages / ΔT , (b) Voltages / T_h (c) Currents/ ΔT , (d) Currents / T_h (e) Power / ΔT and (f) Power / T_h	111
Figure 4.12: (a) Irradiance & temperatures, (b) Measured & numerical temperature (c) Matrix temperature variance.	114
Figure 4.13: Variance on PV cell temperature distribution under different TIMs (a) graphite sheet (b) heat- spreader (c) aluminum foil	117
Figure 4.14: PV-TEG Cell temperature distribution under air-cooled environments (a) bare cell (b) graphite sheet (c) heat spreader (d) aluminum foil....	119
Figure 4.15: TEG voltages under air cooled TIMs (a) bare cell (b) graphite (c) heat spreader (d) aluminum foil	120
Figure 4.16: Cell temperature distribution under water-cooled environment (a) bare cell (b) graphite (c) heat spreader (d) aluminum foil	122
Figure 4.17: TEG voltages under water cooled TIMs (a) bare cell (b) graphite (c) heat spreader (d) aluminum foil	123

LIST OF SYMBOLS

Symbol	Description	Units
α	Seebeck Coefficient	V/K
α'	Effective Seebeck Coefficient	V/K
C_p	Heat Capacity	KJ/K
ΔT	Temperature Gradient	$^{\circ}\text{C}$
ΔH	Enthalpy of Transition	KJ
I_{sc}	Short Circuit Current	A
K	Thermal Conductivity	W/mK
ρ	Electrical Resistivity	$\Omega\text{-cm}$
V_{oc}	Open Circuit Voltage	V
V_{sb}	Seebeck Voltage	V
Qjoule	Joule Heat	J

LIST OF APPENDICES

Appendix I: Contribution of the Thesis	146
Appendix II: Instruments Sensors and Components	147
Appendix III: Heat Spreader Catalogue Extract.....	157
Appendix IV: Coefficients of Linear Thermal Expansion for some common materials:	159
Appendix V: Graphite Sheet Technical Specifications	160
Appendix VI: Kenya Electricity Schedule of Tariffs 2018	164

ACRONYMS AND ABBREVIATIONS

CF	Capacity Factor
CIGS-PV	Copper Indium Gallium Selenide Photovoltaic
c-Si PV	Crystalline Silicon Photovoltaic
CoP-21	Conference of the Parties
CPVT	Concentrated Photovoltaic Thermal
CTE	Coefficient of Thermal Expansion
DNI	Direct Nominal Irradiation
DOA	Days of Autonomy
DPP	Differential Power Processing
DSC	Differential Scanning Calorimetry
DC-DC	Direct Current to Direct Current
ECLEDS	Enhancing Capacity of Low Emission Development Strategy
EPRA	Energy and Petroleum Regulatory Commission
FDTM	Finite Difference Time Domain
FiT	Feed in Tariff
GHG	Green House Gases
GHI	Global Horizontal Irradiation
GOK	Government of Kenya
HDPE	High Density Thermoplastic Polyethylene
HTF	Heat Transfer Fluid
IEA	International Energy Agency

IEET	Institute of Energy and Environmental Technology
IR	Infra-Red
IRR	Internal Rate of Return
IV	Current Voltage
KNBS	Kenya National Bureau of Statistics
KPLC	Kenya Power and Lighting Company
kPa	Kilo Pascal's
LCOE	Levelized Cost of Energy
LED	Light Emitting Diode
LPM	Liters per Minute
MBR	Membrane Bio Reactor
MCHS	Micro-Channel Heat Sink
MET	Meteorological Department of Kenya
MIT	Massachusetts Institute of Technology
MLM	Multi-Layer Multi-Channel
MOE	Ministry of Energy
MPPT	Maximum Power Point Tracking
NOCT	Nominal Operating Cell Temperature
NPV	Net Present Value
O&M	Operation and Maintenance
OVC	Open Circuit Voltage
OWF	Optical Water Filter

PCM	Phase Change Materials
P-si TFPV	Poly-Silicon Thin Film Photovoltaic
PSH	Peak Sun Hours
PV	Photovoltaic
PVF	Polyvinyl Fluoride
PV-T	Photovoltaic and Thermal
PV+TEG	Photovoltaic and Thermoelectric Generator
PVPS	Photovoltaic Power System Program
RAS	Recirculation Aquaculture System
RE	Renewable Energy
SC	Small Commercial
SOS	Save Our Souls
TCR	Thermal Coupling Resistance
TCV	Temperature Coefficient of Voltage
TEG	Thermoelectric Generator
TEM	Thermoelectric Material
TIM	Thermal Interface Material
UNEP	United Nations Environmental Program
UNFCCC	United Nations Framework Convention on Climate Change
USA	United States of America
USAID	United States Agency for International Development
UV	Ultraviolet

VAT	Value Added Tax
VP	Voltage and Power
VicInAqua	Victoria Lake Basin Aquaculture
ZGNR	Zigzag Grapheme Nano Ribbons
Zt	Figure of Merit

ABSTRACT

Renewable power generation has drawn a lot of interest in Kenya in the field of electrical power generation, especially for standalone electricity power supply systems, hence necessitating the in-depth study of the different systems in the renewable energy sector. In particular, solar power generation has attracted immense attention for both standalone isolated grid systems and also for hybrid PV/wind, PV/diesel and grid connect systems. Thermoelectric generation (TEG) is a fairly new technology of electricity generation which has been used in hybrid with Solar PV where the PV waste heat has been used to generate additional power in the TEGs. Using data collected on site a standalone hybrid of solar photovoltaic and thermoelectric (PV+TEG) power plant has been developed capable of generating sufficient electricity to run an autonomous integrated aquaculture system at the Lake Victoria Region of Kenya. During the study, the hybrid PV+TEG generation system has been designed, sized, harmonized and enhanced to run the autonomous aquaculture system. The heat for running the thermoelectric generation system is sourced from the solar PV array waste heat and interfaced using thermal interface materials to improve the overall system efficiency. A 3-tier study has been conducted to evaluate TEG power, voltage, current and temperature distribution and the overall performance of the hybrid system. Medium temperature gradient (10 °C - 100 °C) TEG has been selected and numerical simulations imposed in Simulink using MATLAB R2010b. Bench setups have been fabricated to study the system performance using weather conditions of Nyalenda Kisumu using three types of thermal interface materials. The results obtained confirm that by accurately modelling the TEG and matching its internal resistance to the load and using the right thermal interface materials in the PV-TEG system, PV output could be improved by up to 6.85% and the TEG alone generating an additional 22% of the PV output in a 30kWp system to sustain a combined sanitation and recirculation aquaculture system for wastewater treatment and reuse. It is recommended that future studies on improvement of the TEG figure of merit and better thermal interface materials will make PV-TEG systems more efficient.

CHAPTER ONE

INTRODUCTION

1.1 Background of the study

The emerging renewable energy technologies among them Solar Photovoltaic (PV) and wind power generation generally rely on environmental conditions that make them clean and friendly but also unpredictable. This characteristic demand hybrid operation to improve reliability, availability and efficiency especially for standalone systems. Therefore, the hybrid combination and operation must be selected wisely so that the benefits of the primary system like solar PVs low running costs are not eroded by the complementing system. The technologies that constitute hybrid systems are supposed to complement one another to maintain an almost seamless power supply to the load.

Technologies like solar PV has been operated in a hybrid combination with diesel plants for quite a long time now, but the diesel technology always ends up converting the hybrid system to semi renewable with the running cost of the diesel plant eroding the benefits of the PV plant. Solar PV and wind power technologies have also been operated in hybrid systems but the unpredictability of the practical cut-in wind speed pattern have remained an impediment to the reliability of such hybrid systems necessitating the inclusion of large battery storage back-up in most system designs.

Novel emerging electricity generation technologies like the Thermoelectric Generators (TEG) are fast gaining popularity as the efficiency of the thermoelectric materials improve, and are provoking immense interest for use in hybrid solar PV systems. The present research adopts two technologies based on solar PV and TEG hybrid system for sanitation and aquaculture system application in the Lake Victoria region in Kenya.

1.1.1 Solar Photovoltaic Power Generation Technology in Kenya

The government of Kenya has already put an enabling policy and regulatory framework by enacting the energy Act of 2019, the Climate Change Action Plan, the Updated Least Cost Energy Production Plan and the Power Purchase Agreements that will encourage faster solar photovoltaic power generation growth in the country (*Energy Act, 2019*). Besides the aforesaid, the government has also put in place regulations for Feed-in Tariffs (FiT) for wind and solar PV power plants that shall favor development of such plant's country wide.

Presently, the feed in tariff for solar PV is 12 US cents /kWh for grid connected plants and 20 US cents for standalone mini grid systems as in Table 1.1. The government through the Energy and Petroleum Regulatory Authority (EPRA) have also zero-rated import duty for all solar products and removed Value Added Tax (VAT) on imported Renewable Energy (RE) equipment and accessories (MOE, 2018).

Table 1.1: Feed-in-Tariffs policy for wind, biomass, small hydro's, geothermal, biogas and solar

	Installed capacity (MW)	Standard FiT (USD/kWh)	Percentage Scalable portion of the tariff	Minimum Capacity (MW)	Maximum Capacity (MW)	Maximum Cumulative Capacity (MW)
Wind	10.1-50	0.11	12%	10.1	50	500
Geothermal	35-70	0.88	20% for first 12 years	37	70	500
Hydro	10.1-20	0.0825	8%	10.1	20	200
Biomass	10.1-40	0.10	15%	10.1	40	400
Solar (grid)	10.1-40	0.12	12%	10.1	40	100

Source: MOE, 2nd revision on Feed in Tariffs for Renewable Resources, December, 2012 (MOE, 2018)

1.1.2 Use of Thermoelectric Technology in Power Generation

Thermoelectric generators (TEGs) are some of the most current technologies in the field of thermal electrical power generation. The technology is growing fast in the developed

countries where it has been applied to harvest waste heat mostly in automobiles and in the thermal industry. The technology is slowly penetrating developing countries like in Africa, being imported from Europe, Asia and the USA.

TEG technology was initially used in the automobile industry to generate power for low power demand accessories like; menial internal lighting, air conditioning and for battery charging, where the heat from the automobile exhaust gases is used to heat the TEG while the cooling is done naturally by the ambient environment as the automobile moves (Saqr et al., 2008). But now the use of TEG technology has expanded with development of materials that have higher figure of merit and is currently targeting higher power loads for commercial and industrial systems to exploit the waste heat generated during manufacturing processes (Frobenius et al., 2016).

With widespread development of PV technology in Kenya, TEG technology will find immense application to perform the dual purpose of cooling PV cells and generating electricity. The expected growth of PV and PV hybrid systems in the country shall provoke a lot of study in the area of power loss due to elevated cell temperatures and temperature distribution in matching of PV-TEG systems. Kenya is located along the equator and heating of PV cells is prevalent resulting in substantial power loss.

1.2 Statement of the problem

By the end of 2019, solar PV power generations was only 70 MW or 1.8% of the total electricity generation in Kenya 30MW short of the 2020 PV generation target (Samoita et al., 2020)[6]. The Kenyan strategic plans and vision 2030 projected that Solar PV shall provide 500 MW or 2.6% of the total electricity generation in the country by 2030 (Kerr & Benard Muok, 2014). This is an effort towards freeing the unfavorable fossil fuel generation segment that currently stands at 25.5% in the generation mix. Research has shown that PV power generation is also adversely affected by the prevalent high ambient temperatures in the tropical environment (Atsu & Dhaundiyal, 2019; Razak et al., 2016; Sargunanathan et al., 2016; Temaneh-Nyah & Mukwekwe, 2015), resulting in

increased cell temperature that in-turn reduces the PV power output (Adeeb et al., 2019; Filip Grubišić-Čabo et al., 2016).

Thermoelectric generators (TEG) have been appropriate in absorbing the PV cell temperature and use it to generate electricity by creating a temperature gradient between its surfaces (J. Zhang et al., 2020a). In this study, a pilot solar PV and thermoelectric (PV-TEG) power generation hybrid plant has been designed, developed and tested to generate power for running an autonomous sanitation and aquaculture system (RAS) for waste water treatment and reuse at the Lake Victoria Region of Kenya. This has been done in an effort to improve PV power generation efficiency and PV power generation segment in the country.

Thermal interface materials (TIMs) have been used to investigate cell temperature distributions methods in PV-TEG systems. Preceding research had insufficiently explored TEG modelling and their interconnection and PV cell temperature distribution including methods of mitigating cell temperature mismatch and its effects to TEG power generation (K. Li et al., 2014; Montecucco et al., 2014; Tina & Abate, 2008; J. Zhang et al., 2020b).

1.3 Justification of the study

The Kenyan electricity generation mix currently consists of 26.62% fossil thermal power, with the emerging technologies wind and solar PV occupying 11.77% and 1.81% respectively. Though solar power generation is currently low, there is immense potential in the country. According to the Kenyan vision 2030 that is now almost 10 years to set target, Kenya has projected a shortage of electrical power generation as compared to the projected industrial growth targets and hence laid suitable strategies to meet the power demand come 2030. It is expected that by the year 2030, solar PV power generation shall have reached a peak of 600 MW constituting about 2.6% of the expected national peak generation. Going by the recent PV power plants development trend, there are high hopes that this target of 600 MWp shall be realized.

As the development of PV progresses in Kenya, PV power generation losses shall increase proportionally, therefore the need to conduct in-depth studies on cell temperature mitigation and hybrid technologies that result in temperature effects mitigation. TEG technology shall come in appropriate as a matching technology to absorb the PV cell waste heat and use it to generate additional electricity. This shall result in increasing PV+TEG power generation that will replace the fossil power portfolio in the Kenyan electricity generation mix

Since 2010, Kenya has been making efforts to increase its RE power generation portfolio to reduce Green House Gas (GHG) emission as targeted by the vision 2030. And in 2015, at the Paris Conference of the Parties (CoP-21) of 2015, at the United Nations Framework Convention on Climate Change (UNFCCC) in Paris, Kenya pledged to reduce its GHG emission by 30% by 2030 in comparison to the 2015 emission levels (Dalla Longa & van der Zwaan, 2017). Also in 2014 the country benefited from the United States Agency for International Development (USAID) “Enhancing Capacity of Low Emission Development Strategy” (ELEDs) to develop low emission initiatives in clean energy and also to conduct audits on carbon emission in the country (Newell et al., 2014).

However, even with the envisaged PV development in the country and globally, very little studies have been done in the area of PV cell temperature distribution and modelling of matching hybrid technologies like the thermoelectric generator. The interconnection patterns of the TEG and the losses due to interconnection patterns have also not been studied very well.

This prototype PV-TEG hybrid system could later be replicated in other areas with similar environmental conditions or where there is ample sunlight and cooling water to generate power supply to autonomous sanitation and aquaculture systems.

1.4 Objectives

1.4.1 Objective

To design, develop and study a solar PV-TEG hybrid system for an autonomous sanitation and aquaculture process in the Lake Victoria region of Kenya.

1.4.2 Specific objectives

The specific objectives are to;

1. To assess temperature and irradiance profiles at JKUAT and the Nyalenda Kisumu lake side site and study the effects of temperature on PV-TEG hybrid systems.
2. To design and simulate a PV-TEG in MATLAB Simulink and test it for autonomous power supply.
3. To numerically and experimentally investigate PV-TEG thermal coupling strategies for mitigation of PV cell temperature effects on electricity generation.
4. To implement, test and determine the solar PV-TEG system economic viability.

1.5 Research Questions

The main research questions that have been addressed during this study are primarily three;

1. Whether there is adequate irradiation able to operate a hybrid solar PV + TEG power generation plant to run an autonomous aquaculture system at the Nyalenda Kisumu site?

2. Whether solar PV cells on the PV+TEG system shall develop adequate waste heat under the Nyalenda Kisumu site environmental conditions, enough for the TEGs to generate significant electrical power to complement the PV power?
3. Whether the hybrid PV+TEG technology shall be economically viable on site and used for further replication elsewhere in sites with similar environmental conditions?

1.6 Scope of Study

The scope of this research study is limited to preliminary solar irradiance and temperature data collection from the JKUAT -IEET Juja and finally at the project site at Nyalenda Kisumu. This data has been utilized in the design of the solar PV +TEG hybrid system to supply power to an autonomous aquaculture and recirculation system in Nyalenda Kisumu. This data has also been used in the simulation, synthesizing, mapping, integration and subsequent design and sizing of the solar PV+TEG hybrid system. An economic analysis of the system has also been carried out to determine the viability of the hybrid system.

1.8 Thesis Structure

This thesis document has been structured into five (5) interrelated chapters all building and culminating into the findings of the research exercise conducted, results found, conclusion drawn and recommendations made in the study. The flow chart Figure 1.1 shows the flow. The Appendices follow immediately after the fifth chapter the references.

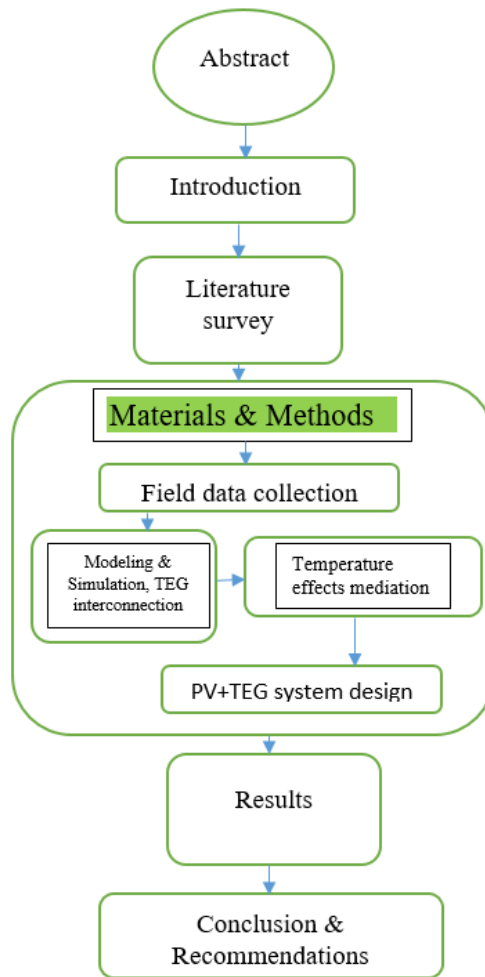


Figure 1.1: Thesis structure flow chart

CHAPTER TWO

LITERATURE REVIEW

2.1 Introduction:

Solar PV power generation has been in existence since 1954 when the solar cell was invented by Gerald Pearson of Bell Laboratories (MIT) in the United States of America (Reiss H et al., n.d.). For quite some time, the commercial application and benefits of the solar PV cell technology were not explored beyond the laboratory research environment until the diminishing trend of fossil fuel resources emanated and became noticeable in the late 1970s provoking the global quest for alternative, sustainable and renewable sources of energy (Fattouh et al., 2019).

The thermoelectric power generation (TEG) concept has been emergent for close to 200 years since its discoveries by Johann Seebeck in 1821 and Charles Peltier in 1834 and later in 1855 when Thomson combined the two concepts and brought to light the thermoelectric phenomena (Karami & Moubayed, 2014). These discoveries remained undeveloped until the late 21st century when thoughtful studies and tests were done to make TEG a commercially viable technology for electrical power generation.

Since then, further research work has been done and today emerging alloys of semiconductor materials are being used in the manufacture of thermoelectric materials (TEMs). Intensive studies have so far been carried out on both solar PV materials and thermoelectric materials with an effort to improve efficiency and also reduce the cost of these materials.

In solar PV technology, studies have been done to increase the cell power output using multilayer cell technology for wider electromagnetic radiation spectrum coverage and also to reduce the negative effects of temperature on the output voltage of the solar cell like the six junction III-V cells (Geisz et al., 2020). In the field of thermoelectric technology, studies have been carried out to manufacture using nanotechnology,

materials that have low thermal conductivity and the highest possible electrical conductivity that will result in the improvement of the generation efficiency of the TEG systems (G. Li et al., 2016). And as a result, better materials have been developed consisting of a combination of one or two natural materials like bismuth, lead, telluride and silicon.

This chapter shall present the two technologies and also discuss specific accomplishments made in both technological fields and mitigation methods used to the challenges in hybridizing the technologies.

2.2 Solar Photovoltaic Power Generation Technology in Kenya

Solar PV power generation was first introduced in Kenya in 1982, after the international environmental conference held at the UNEP Nairobi in 1981 brought awareness to the development of new and renewable sources of energy in the world. These discussions initiated the installation of small standalone solar home systems of 12 W peak mainly in the agricultural tea and coffee growing regions of the country (UNEP, 1981). Subsequently, the technology started attracting more attention resulting in individuals and institutions installing standalone systems of up to 10kW by the close of the 20th century.

So far, there are many larger PV systems installed, mostly grid connected like; the 550 kW UNEP system installed in 2014, 60 kWp Mombasa SOS system of 2014, 600 kWp Strathmore University system of 2016, 1 MWp Kay salt company system at Gongoni Malindi of 2016 and the 1.2 MWp Changoi Williamson tea system of 2015 just to name but a few. Other smaller isolated solar PV grid systems are the 300 kWp located in Mandera, the 60 kWp in Hola, 60 kWp in Habasweni 70 kWp in Timau and 50 kWp in Elwak (Bernard Muok & Debajit Palit, 2015).

Additionally, by 2016, the Kenya government had projected to develop solar PV electricity generation to 600 MWp by 2030 and projected to achieve this by developing

new solar plants. The solar PV plants projected were; Samburu solar 40 MWp, Kopere Solar Park in Kisumu 22.7 MWp, Witu Solar Park in Kwale 40 MWp, Garissa Solar project 55 MWp (completed in 2021), Isiolo Solar 40 MWp and Nakuru Solar 25 MWp. Other such plants are in Eldoret 40 MWp and Nandi Solar at 50 MWp (Rose et al., 2016). These plants would add an extra solar PV generation of 312.7 MWp to the generation of 70 MWp.

Though there is a wide uptake of solar PV generation, Hybrid plants like PV+TEG are yet to come up in Kenya and also in Africa.

Solarice and the German Solar Association carried out a study on the solar market in ten African countries. The countries were Algeria, Angola, Egypt, Ethiopia, Ghana, Morocco, Namibia, Nigeria, South Africa and Tanzania. They found out that Africa had only installed 5110 MWp by 2019 and projected the installed capacity to grow to 29 GWp by 2030 (Joshua Hill, 2019).

2.3 Solar Photovoltaic Power Generation Technology

2.3.1 PV cell technology

The sun is a huge “*ball of fire*” burning in a massive thermonuclear fusion reaction where mass is converted to energy according to Einstein’s formulation, $E = mc^2$, at a temperature of approximately 5800 K and provides the energy needed to sustain life in the entire solar system such that in one hour, the earth receives enough energy to supply a whole years energy needs on the globe (Roger A Messenger (last) & Jerry Ventre, 2010).

Since the first discovery of the photovoltaic effect by the French Physicist Edmond Becquerel in 1839 and later the invention of the first practical solar cell by Bell laboratories in 1954, the use of the silicon solar cell to capture and convert the suns radiant energy has continued growing undeterred (Lincot, 2017). Subsequent to these discoveries, the efficiency of the solar cells has been improving gradually from an

efficiency of 1% in 1952 to now a high efficiency of 24.4% and still improving (Lincot, 2017). The solar photovoltaic cell is essentially a P-N junction whose electrical characteristics can be described by Equation (2.1) as (Lincot, 2017);

$$I = I_0 \left(\exp \left(\frac{qV}{nKT} \right) - 1 \right) - I_l \quad (2.1)$$

where I is the current density per unit area, I_0 is the saturation current, V is the voltage across the junction, q the charge of the electron, K the Boltzmann constant, T the absolute temperature, n the ideality factor of the diode which varies between 1 and 2 and is 1 for silicon. The performance of a photovoltaic cell and its efficiency are normally inversely proportional to the temperature of the cell such that as the temperature increases, the band gap of the intrinsic semiconductor shrinks reducing the open circuit voltage (V_{oc}) causing a lower power output at a given photocurrent as the charge carriers are liberated at a lower potential.

Though the temperature has a positive temperature coefficient to the short circuit current (I_{sc}) in entirety, the effects of temperature increase results in reducing the theoretical maximum power output ($P_m = I_{sc} \times V_{oc}$) of the solar cell (Jakhrani A.Q et al., 2011).

Practically the solar cell is only capable of converting part of the electromagnetic spectrum between 400 nm -1100 nm into electricity while the rest of the spectrum converts into heat that raises the cell temperature (Sargunanathan et al., 2016).

2.3.2 Temperature effects on the performance of the solar cell

When a solar cell is exposed to sunlight, it heats up due to its energy band gap limitation on the absorption of the electromagnetic spectrum especially when used in the tropical regions where ambient temperatures are generally higher. The PV cells can only convert a portion of the incident photons of the electromagnetic spectrum into electricity as per

the cell's efficiency and band-gap energy requirements. The remaining photons therefore result into heat that ends up heating up the solar cell (Kane & Verma, 2013).

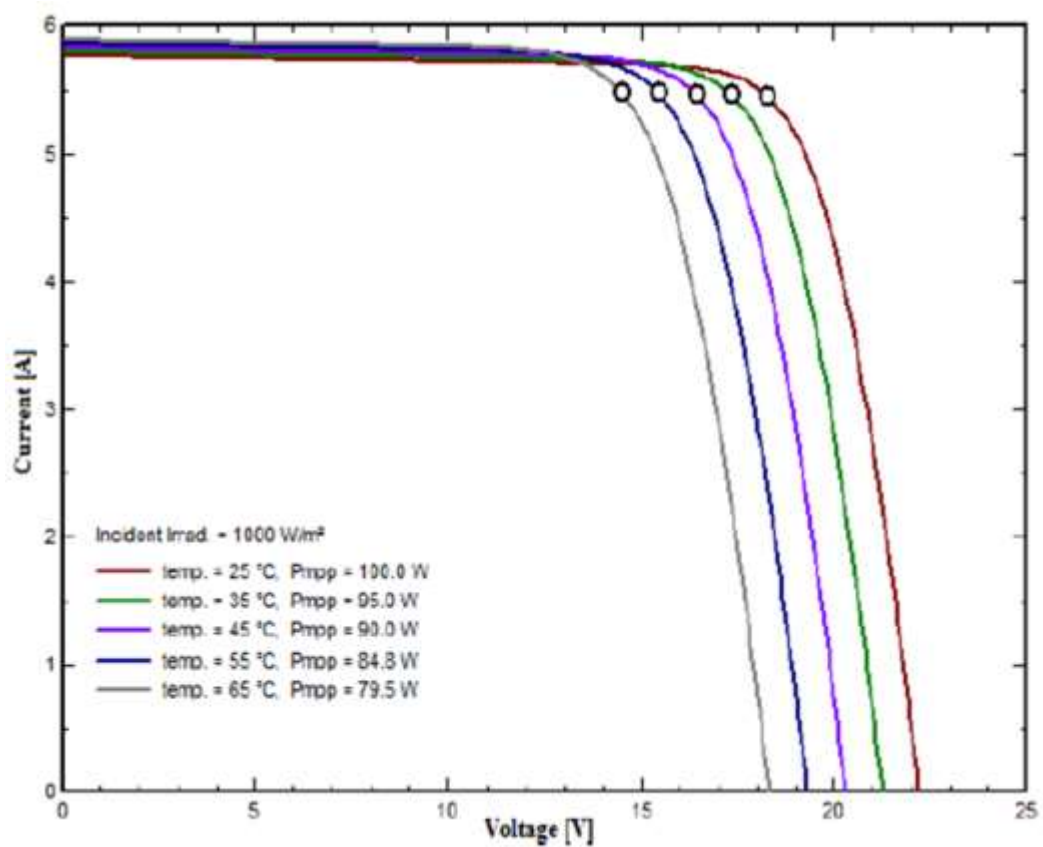
The electromagnetic radiation spectrum that supplies radiant energy to the PV systems consists of ultraviolet, visible light and infrared wavelengths where ultraviolet occupies 3% at 100 - 400 nm, visible light 44% at 400 nm - 700 nm and infrared 53% at above 700 nm, of the radiant energy spectrum. A typical polycrystalline silicon cell has an upper sensitivity boundary of $\lambda_{\max} = 1110$ nm corresponding to its band gap energy, so beyond that wavelength, the spectrum converts to thermal energy that adversely affects the cell (Rajkumar et al., 2015).

Currently, the most popular cells are silicon solar cells with upper limit efficiency of 24.4 % due to the limitations of the absorbed solar photon energy (N.K.Kasim et al., 2019). Studies on the negative effects of elevated temperatures on PV cells have shown that the voltage output of a solar cell could reduce by 4% -5% for every 1 °C temperature rise (D Atsu) (Atsu & Dhaundiya, 2019). Studies carried out by Razak Amelia et al (2016) showed that PV modules' elevated temperature reduced the output voltage and subsequently its power production (Razak et al., 2016). In their studies, Temaneh, and Mukwekwe (2015) showed that a 37.8 kWp solar PV system operating at an average module temperature of 35.4 °C in Namibia lost at least 3.21% of its rated system power output (Temaneh-Nyah & Mukwekwe, 2015). In their study on experimental verification of thermal behavior of PV modules, Tina GM et al (2008) observed that distribution of temperature along the surface of the module is not uniform. The temperature is maximum at the central cells and minimum along the border of the PV module.

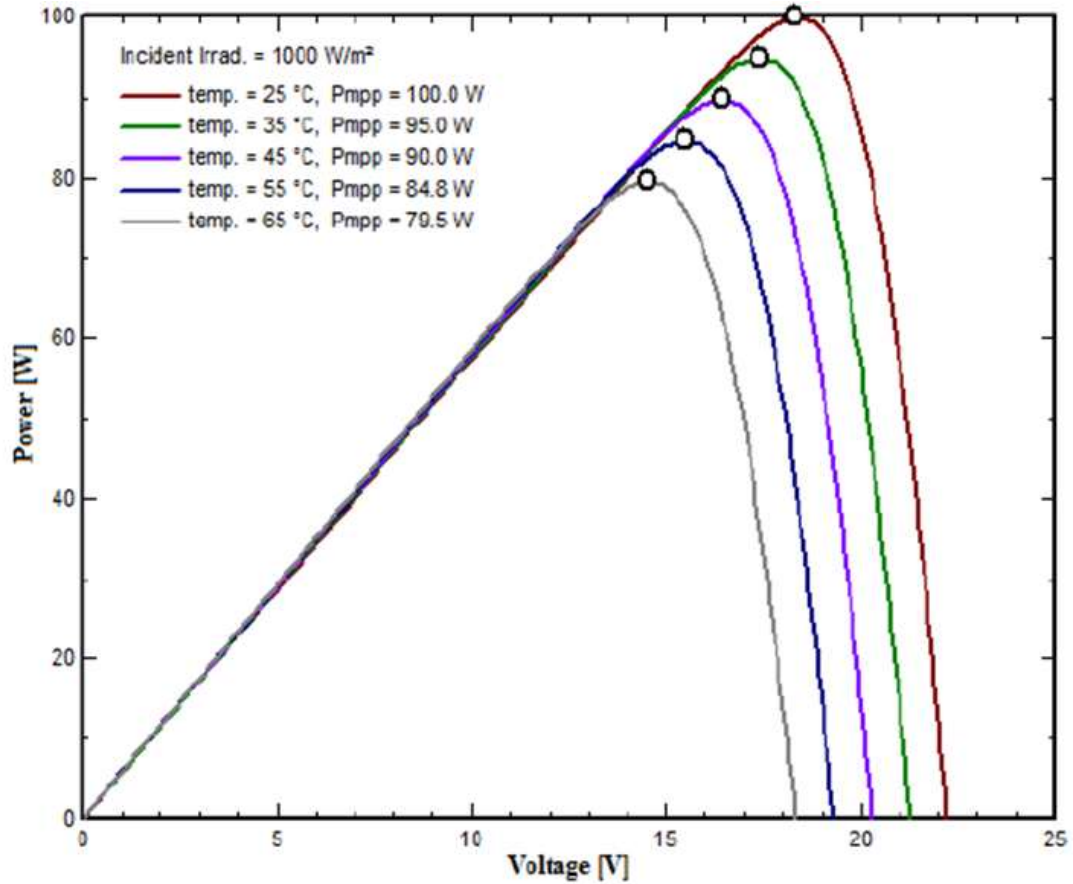
Figure 2.1 shows standard solar PV module Current –Voltage (I-V) and Power –Voltage (P-V) response curves at a constant irradiance of 1000 W/m² as the cell temperature increased from 25 °C to 65 °C. The IV curves' characteristics confirm that the solar cell has negative temperature coefficient of voltage implying that the cell voltage reduces as the cell temperature increases, resulting in corresponding reduction in its power output.

Besides the reduction in the power output, elevated cell temperatures also accelerate the cell degradation process leading to its premature failure (Ferrara & Philipp, 2012).

When we analyze the PV module I-V and P-V characteristic curves in Figure 2.1, we observe that as the PV module temperature increases by 10 °C, the voltage reduces by 1 volt and the power output reduces by a corresponding 5 watts. Therefore, the maximum power of the PV module is reduced to 79.5 watts at 65 °C from the rated 100 watts at 25 °C reducing the actual peak power output of the PV module.



(a) I-V Curve



(b) P-V Curve

Figure 2.1: (a) I-V and (b) P-V Characteristics of a PV Module at constant irradiance of 1000 W/m² (Razak et al., 2016)

2.3.3 Mitigation of the negative effects of temperature

Numerous studies have been carried out to mitigate this condition of PV system power loss due to elevated cell temperatures and improve power generation efficiency especially in tropical and sub-tropical regions. As a result of these studies, methods have been developed to try and diminish high PV cell temperatures like; creating adequate cooling air flow between the module's back plates and the mounting surface, cooling the PV modules using Nano fluids, use of micro channel heat sinks, use of phase change

materials (PCM), use of cooling panels and even floating the PV modules on water bodies (Al Siyabi et al., 2018; F. Kawtharani, M. Hammoud et al., 2017; Hussien et al., 2013; Yadav et al., 2016). The methods are briefly discussed here.

i. Nano fluids air and water for cooling PV cells

Nano fluids are types of fluids developed from dissolving conducting substances into a base fluid to increase their heat conductivity and are ordinarily applied to convey heat across surfaces hence referred to as heat transfer fluids (HTF). They have been used in heat exchangers in power generation stations, heating and cooling systems for buildings (HVAC), vehicle air conditioners and in transportation systems (N. Ali et al., 2018). In mitigating the negative temperature effects, (Soltani et al., 2017) examined five cooling methods experimentally using; natural air, $\text{SiO}_2/\text{water}$ nanofluid, forced air and $\text{Fe}_3\text{O}_4/\text{water}$ nanofluid cooling. They observed that $\text{SiO}_2/\text{water}$ nanofluid cooling yielded the best efficiency improvement of 3.35% followed by $\text{Fe}_3\text{O}_4/\text{water}$ nanofluid with 3.13%.

Abu-Rahmeh T. M. et al (2017) evaluated the efficiency of a PV module using different cooling methods; nanofluids, tap water and fins and observed that cooling PV modules enhanced heat transfer and improved their electrical efficiency (Abu-Rahmeh, 2017). He also observed that among the cooling media used to cool the PV module, the nanofluid (0.04% wt TiO_2) gave the best results out of the three. In their work on PV efficiency optimisation using active cooling methods, Peng Z. et al (2017) observed that a PV system with integrated cooling increased its energy output by 34.6% while the same system with cooling and hot water production from the PV cooling system, increased its energy production by an extra 72.4% (Peng et al., 2017a). Figure 2.2 shows the experimental design of the cooling system for solar panels used in residential PV systems where the water used for cooling the PV modules is used for domestic hot water purposes where it serves a dual purpose and offers double gains.

Further,(Musthafa, 2015), used an experimental set-up of a water cooled PV system using water absorption sponge and reported a cell temperature reduction of 4 °C that resulted in 6.4% power increase and an output efficiency increase of 2.6%.

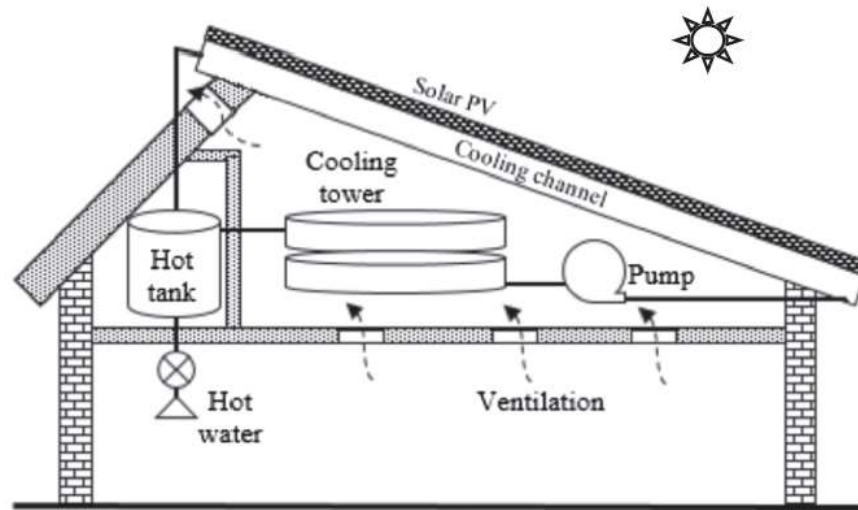


Figure 2.2: Cooling system for solar panels of residential applications – (Peng et al., 2017b)

Another case in point was in Baghdad (2014), where researchers (Hashim et al., 2016), set up to investigate the thermal efficiency of PV modules versus temperature using Nano-fluid as a cooling medium at a constant mass flow rate of 0.2 liters/second. Results obtained from this study showed that the electrical conversion efficiency improved with the application of the Nano-fluid to cool the module reducing the temperature from 72.9 °C to 42.2 °C. Under these conditions with a solar irradiation of 1000 Watts/meter square and a 24 minutes' test time, the temperature of the module reduced to 42.2 °C and the module electrical efficiency increased from the previous 8% to 12.1% while the thermal efficiency of the module increased to 34.4%.

ii. Thermal interface materials for cooling PV cells

Use of thermal interface materials (TIM) to cool PV modules has been explored severally. Soliman A. M. A. et al (2018) in their study used a three dimensional theoretical model of a PV module coupled with a 125 mm x 125 mm, 10 mm thick heat spreader to study the effects of using the heat spreader on the performance of a PV module and they realised a 15 °C decrease in the cell temperature and a corresponding 9% power increase when the heat spreader was used (Soliman et al., 2020).

In another study to cool PV modules using heat spreader with cotton wick structure, Chandrasekhar M. et al (2015) observed that the cooling setup was able to reduce the maximum cell temperature from 49.2 °C to 43.3 °C and increase the PV power yield by 14% (Chandrasekar & Senthilkumar, 2015). In their setup, the thermal loss coefficient increased to a high value of 77.5 W/m²K due to the increase in leeward surface convective coefficient caused by evaporation cooling and fin effect. Previously, (Cuce et al., 2011) had demonstrated that aluminium heat sink could reduce the PV module temperature by 19.95%, while (Alami, 2014) had demonstrated a 19% PV module temperature improvement by using passive evaporation cooling techniques. Figure 2.3 shows the fabrication process of the heat spreader and cotton wick structures complete with stiffeners and inlet and outlet headers for cooling PV modules by Chandrasekhar and his team.

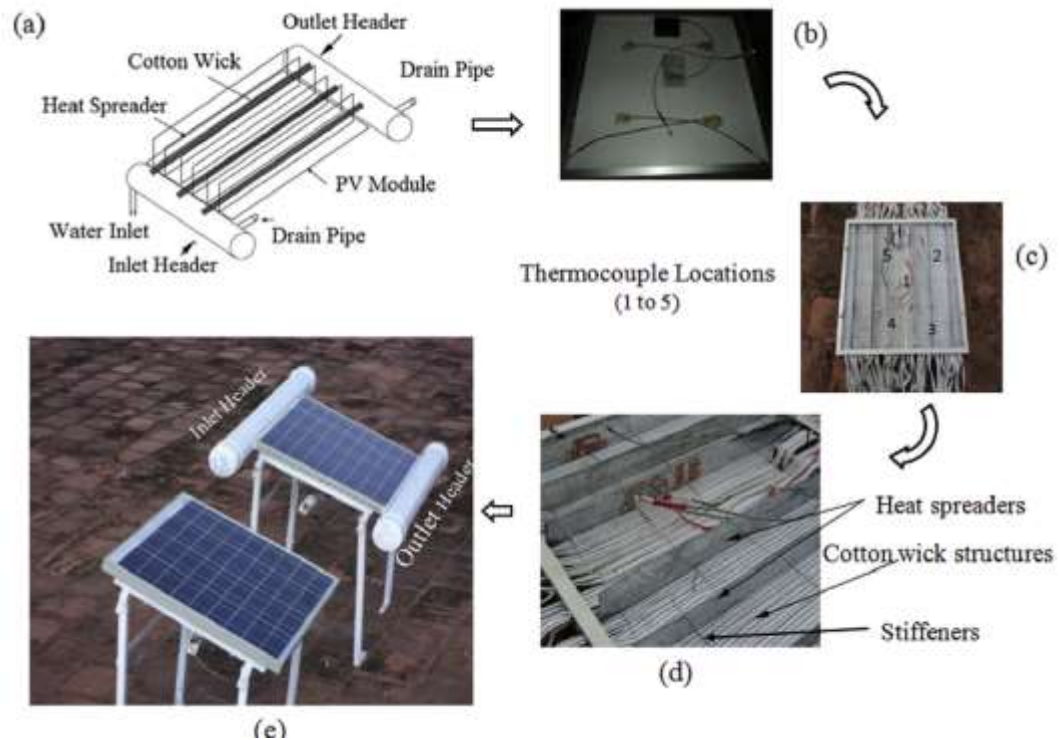


Figure 2.3: Fabrication of the heat spreader and cotton wick structures for cooling PV cells (Chandrasekar & Senthilkumar, 2015)

iii. Use of phase change materials, fins and thermoelectric materials

A lot of efforts have also been made to use phase change materials (PCM) and fins to reduce the adverse effects of elevated PV cell temperature in PV power generation. PCMs absorb, store, and release large amounts of energy in the form of latent heat at constant temperature so they are very ideal in temperature regulation. PCMs may be categorized as three subsets: organic compounds which consist of paraffin's, fatty acids, alcohols and waxes, inorganic compounds like hydrated salts and eutectic mixtures.

These compounds have different phase change temperature ranges that actually determine their application. They function on the principle of the differential scanning calorimetry (DSC) curve of heat flux versus temperature level or time which can be used to calculate the enthalpy of transitions ΔH by integrating the peak corresponding to a

given transition (ISO 6946:2007, 2007) as in Equation (2.2) (Ewa Klugmann-Radziemska & Patrycja Wcisło-Kucharek, 2017);

$$\Delta H(T) = \int_{T_0}^T C_P(T) dt \quad (2.2)$$

where ΔH [KJ] is the enthalpy of transition, $C_P(T) \left[\frac{KJ}{K} \right]$ is the heat capacity at constant

pressure and T [K] is the temperature level. Klugmann-Radziemska E. et al (2017) set to study the effects of PV/PCM systems as compared to conventional PV systems and observed that for constant solar irradiance, the conventional PV system heats up to higher temperatures as compared to the PV/PCM system. They used different PCMs; Paraffin 42-44, Rubitherm RT22 and Ceresin and the best results were obtained using Paraffin 42-44 with a thickness of 2 cm and water cooling that lowered the PV module temperature by 7 K for a period of 5 hours (Ewa Klugmann-Radziemska & Patrycja Wcisło-Kucharek, 2017).

Bayrak F. et al (2020) also conducted a study to compare the effects of passive cooling methods; PCM, Aluminum fins and TEG cooling on PV modules. They set up systems as PV + Fin1 B3, PV + PCM + Fin 2 (C + B) and PV + TEM (E) and subjecting the systems under the same environmental conditions, obtained the best results from the (B3) system at 47.88 W, followed by the combined (C+B) system at 44.36 W and lastly the hybrid system (E) at 44.26 W (Bayrak et al., 2020). Figure 2.4 shows the setup fabricated by Bayrak et al (2020).



Figure 2.4: Back view of the PV setup (left) PV + PCM (top right) PV + Fin (bottom right) Reference PV (Bayrak et al., 2020)

iv. Micro channel heat sinks and Fins for cooling PV cells

Researchers (Al Siyabi et al., 2018) carried out an experimental and numerical study of a multi-layered micro-channel (MLM) heat sink for concentrated solar PV temperature regulation and investigated the effects of the number of layers and heat transfer fluid (HTF) flow rate on performance of the MLM heat sink at various heat fluxes. Figure 2.5 shows their setup where Figure 2.5 (a) shows the schematic of the test module parts and Figure 2.5 (b) shows the thermocouple locations at the test points on the test module.

They observed that increasing the number of layers has a major impact on reducing the heat sink thermal resistance and the heat source temperature. Also, the thermal resistance decreases by 17% as the number of layers increased while the thermal efficiency is improved significantly to 20% due to increase in the HTF outlet

temperature by increasing the layers from 1 to 3 layers. When the input power was increased from 5 watts to 30 watts, the heat sink total thermal resistance increased with a corresponding increase in source temperature and the heat sink showed ability to accommodate a wide range of power rates with a slight change in thermal resistance (Al Siyabi et al., 2018).

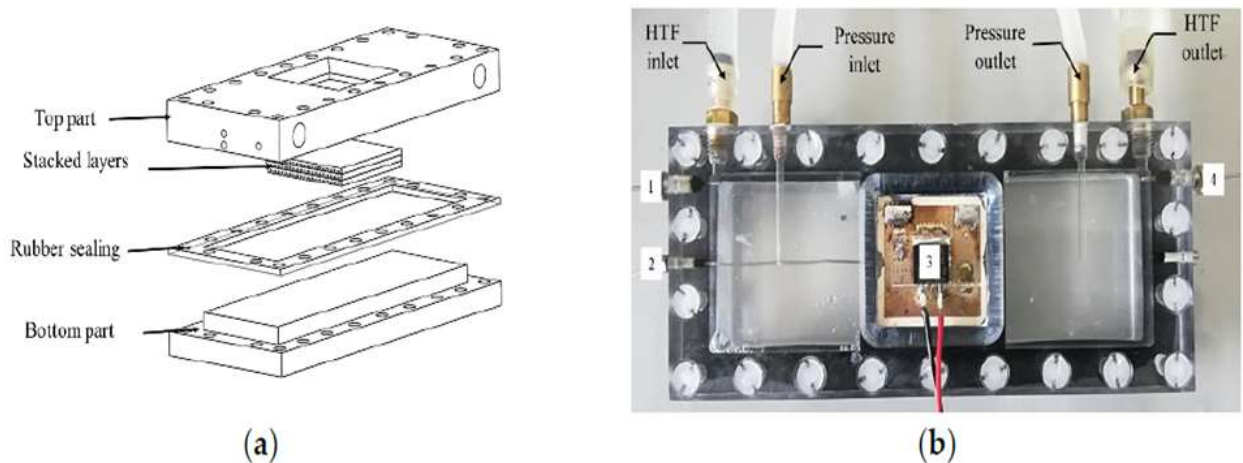


Figure 2.5: Micro –channel heat sink setup (a) Schematic of the module parts (b) Thermocouple locations on test points (Al Siyabi et al., 2018)

In similar work, (M. Ali et al., 2015) used two 35 Watts PV modules to investigate performance of micro-channel heat sinks in Taxila, Pakistan at flow rates of 0, 0.15, 0.55, 1.25, and 3 litres per minute (LPM) under uniform irradiance and observed a high temperature difference of 15 °C at 3 LPM when the average irradiance was 915 W/m² and the ambient temperature was 39.3 °C, and a corresponding power output increase of 14% and 3% increase in efficiency (Soltani et al., 2017). With a lower average irradiance of 548 W/m² and ambient of 37.3 °C, a temperature drop of 4 °C was observed in the same setup. He also (M. Ali et al., 2015) developed a comprehensive three dimensional model for PV layer integrated with micro channel heat sinks and using a numerical model and applying Equation (2.3) by (Radwan & Ahmed, 2017), the heat

generated per unit volume of the layer due to solar irradiance absorption was determined.

$$q_i = \frac{(1 - \eta_{sc})\alpha_i G \tau_j A_i}{V_i} \quad (2.3)$$

where η_{sc} is the solar cell efficiency, α_i , A_i , and V_i are the absorptivity, area and volume of the layer i , respectively and τ_j is the net transmissivity of the layer i . They also calculated the silicon layer efficiency as in Equation (2.4) by (Xu et al., 2015);

$$\eta_{sc} = \eta_{ref} \left(1 - \beta_{ref} (T_{sc} - T_{ref}) \right) \quad (2.4)$$

where η_{ref} and β_{ref} are the solar cell efficiency and temperature coefficient at the reference temperature of $T_{ref} = 25$ °C.

Elsewhere, Ruijin W. et al (2018) designed a micro-channel heat sink (MCHS) using V-ribs and water based nano fluid as the coolant and carried out numerical simulations with Reynolds number ranging between 200 and 1000 to investigate the flows and heat transfers in the MCHS. They observed that MCHS with V-ribs improve heat transfer capabilities due to the chaotic convection in the micro channel capable of improving the heat transfer performance by about 124% to 202% as compared to MCHS with no ribs (Wang et al., 2019).

v. Use of light absorption and multi-junction PV cells

In their work, Geisz et al (2020) presented a 47.1% solar conversion efficiency six junction III-V semiconductors cell made using a monolithic series connected inverted metamorphic multi-junction devices (Geisz et al., 2020). They further alluded that further reduction of the limiting series resistance should result in cell efficiencies above 50% at higher concentration. Investigations carried out by Xu et al on ultra-broadband (300 - 2500 nm) photon management for crystalline silicon thin film solar cells using Finite Difference Time Domain (FDTM) proposed a novel thin film cell structure (Xu et al., 2015). The light absorption in 300-1100 nm and high transmission in 1100-2500 nm are obtained Omni-directionally by incorporating anti-reflection and light-trapping concepts.

By assuming that every photon is absorbed in crystalline silicon, the light absorption capability was estimated by calculating the short circuit current (photon current) J_{sc} at

AM 1.5 G using equation (2.5),

$$J_{sc} = \int_{300nm}^{\lambda_0} x j_{sc} d\lambda = e \int_{300nm}^{\lambda_0} \alpha(\lambda) F(\lambda) d\lambda \quad (2.5)$$

where e is the electron charge, $\alpha(\lambda)$ is absorption in silicon dependent on wavelength, $F(\lambda)$ is the energy density at AM 1.5G, λ_0 is the wavelength corresponding to the band-

gap of the crystalline silicon. This feature has provoked a lot of studies on PV cell cooling using both passive and active methods to recover the energy lost under elevated cell temperature.

vi. Use of optical water filters

Among the methods used to mitigate high PV cell temperatures, optical water filters (OWF) methods are developing very first after researchers like Al Shohani et al, presented investigations of a novel optical water filter (OWF) for PV-thermal (PVT) and

concentrated PV-thermal (CPVT) module systems using a water layer of wavelength range of (0.35 μm -1 μm) and thickness of (1 cm – 5 cm) and observed that the water layer enhanced the PV performance and also prevented cyclical thermal stresses on the PV cells. They further conducted experiments aimed at reducing heat accumulation in a PV module using OWF and observed that PV module temperatures decreased with increasing thickness of the OWF layer (Al-Shohani et al., 2016).

Figure 2.6 show a cross-section of an optical water filter consisting of three layers; two of glass sandwiching the water layer. Elsewhere, Rosa M. et al (2016) also investigated use of OWF method on photovoltaic-thermal (PV-T) systems and observed that their implementation resulted in a small reduction in electrical energy, but contributed significantly on thermal energy subsequently increasing the overall system efficiency (Rosa-Clot et al., 2016).

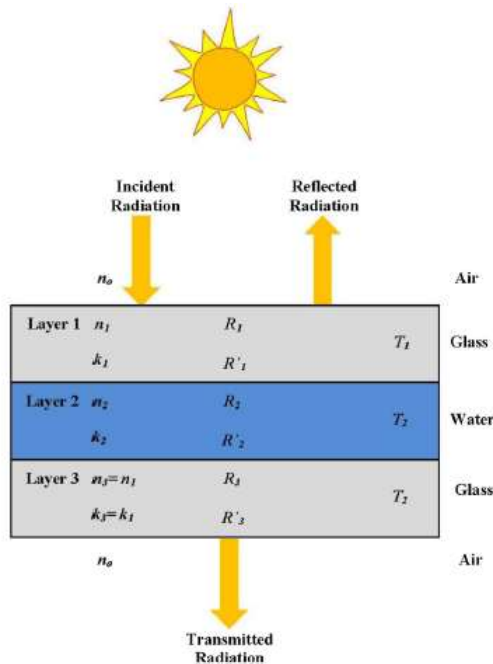


Figure 2.6: Cross-section of an optical water filter for PV modules (Al-Shohani et al., 2016)

vii. Use of water floating PV systems

Floating systems are currently a common form of PV array system cooling layouts since the first plant was installed in 2008 at the Far Niente Wineries in California USA. After this pioneer installation, many such floating PV systems have been developed mainly for cooling the PV systems and especially in countries where availability of land is scarce. Japan, Italy, India, china and USA are some of the leading countries in the development of such floating systems. Most of these systems use suspended PV modules above the water surface using buoyant structures like High Density Thermoplastic Polyethylene (HDPE) where the cooling is convectional and some of the plants even integrate single axis tracking systems to optimise the design peak power generation of the plant (Trapani & Redón Santafé, 2015).

Yadav N. et al, used a 250 Watts PV system floating on high density thermoplastic polyethylene (HDPE) blocks to experimentally study its performance in Manit Bhopal. The 250 W system was tested with varying irradiance between 125 W/m^2 and 945 W/m^2 and reported an improved generating efficiency of 0.79% compared to the conventional PV systems (Yadav et al., 2016). They further proposed solar tracking water floating system where the azimuth and the tilt angles could be varied with the earth movement. Divya M. et al (2017) carried out a feasibility at Kota Rajasthan India and presented two 1 MW peak water floating systems, one at Kota barrage and the other at the Kishore Sagar Lake in Kota, Rajasthan.

They projected the plant at Kota barrage to produce an estimated 1,838,519 kWh annually equivalent to offsetting 1,714 tonnes of CO_2 and the Kishore plant would produce an estimated 1,858,959 kWh annually offsetting about 1,733 tons of carbon dioxide annually. Figure 2.7 shows a 4 MW water floating PV plant in Jamestown Australia (Divya Mittal1 et al., 2017).



Figure 2.7: 4MW Tracking type floating system Jamestown Australia (Divya Mittal et al., 2017)

2.4 The thermoelectric technology

The TEG devices are made from Thermoelectric Materials (TEMs) of two dissimilar semiconductors that generate electricity from heat-flux following the Seebeck phenomenon. The semiconductor materials are fused to form a P-N junction using one P-type and N-type elements and the junction formed generates electricity following the Seebeck phenomenon when a temperature gradient (ΔT) is created between the hot and cold surfaces of the device (D. Rowe, 1999).

This suggests that thermoelectric generators essentially apply the thermocouple principle to generate electricity. The pairs of P-N junctions or pellets formed are then connected in an electrically series and thermally parallel formation so as to form a complete thermoelectric generator module that often comprises of 127 pellets (Kwan & Wu, 2017). When a temperature gradient ΔT is created between the two outer ceramic surfaces of the module, a voltage is generated and current flows with the N element assuming the positive and the P element the negative polarity as shown in Figure 2.8(Y. Deng et al., 2013).

The appropriate materials used for making TEGs are materials that possess low thermal conductivity and high electrical conductivity properties for them to perform the function of electricity generation efficiently. Such materials are like; Bismuth telluride (Bi_2Te_3) operating at 450 K, Lead telluride (PbTe) operating at 850 K and Silicon germanium (SiGe) at 1300 K, whose figure of merit (Zt) is ranging between 1 and 2.0 (David M Rowe, 2006). With the emergent demand for more efficient thermoelectric materials, studies in the field of Nano- technology are focused primarily on the manufacture of such materials that will improve the efficiency of the thermoelectric generators for popular commercial viability.

Essentially, for a thermoelectric generator to generate electricity, there must be the TEG module, a heat source or heat exchanger preferably waste-heat and a cooling system. Most thermoelectric generator systems comprise of two heat exchangers; one for heating the hot side of the TEG and another for cooling the cold side of the TEG to create a temperature gradient that facilitates generation of electromotive force (EMF). All thermoelectric generators yield direct current voltage that is proportional to the temperature gradient between the cold and hot surface of the TEG.

Thermoelectric generators have advantages in that they generate electricity without producing any noise at all, they have a durability of up to 30 years and they are also very compact in nature. Besides the aforementioned, they are light in weight, portable, inexpensive and are effortlessly scalable or modular in structure so they can be interconnected to increase power generation (Yazawa & Shakouri, 2016).

The thermoelectric technology is associated with refrigeration and thermoelectric generation, where in refrigeration, the Peltier phenomenon is explored and in thermoelectric generation, the Seebeck phenomenon is similarly explored (David M Rowe, 2006).

Among the two, thermoelectric generation (TEG) has attracted enormous attention in the area of waste heat recovery and system efficiency improvement where waste heat is

utilised for electricity generation. The voltage generated by a TEG is a product of the temperature gradient and the Seebeck coefficient where the temperature gradient is expressed as in Equation (2.6), (David M Rowe, 2006) and Figure 2.8 shows the TEG schematic diagram.

$$\Delta T = T_h - T_c \quad (2.6)$$

where T_h and T_c are the hot side and cold side temperatures respectively.

And the Seebeck voltage or open circuit voltage is expressed as in Equation (2.7), (David M Rowe, 2006);

$$V_{oc} = \Delta T \alpha \quad (2.7)$$

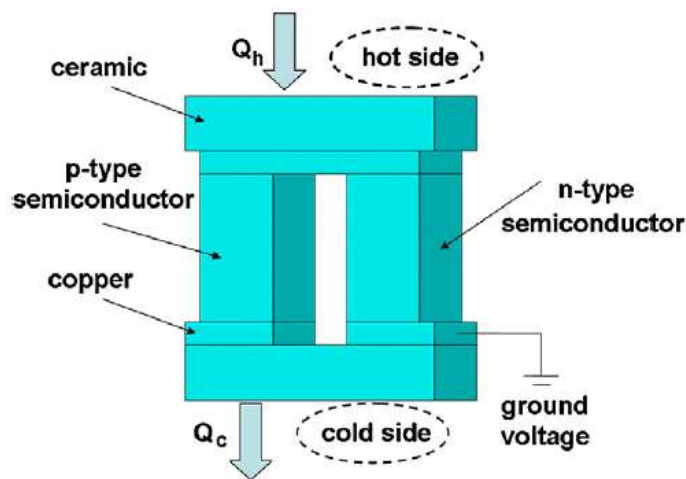


Figure 2.8: Schematic diagram of a thermoelectric generator pellet (Y. Deng et al., 2013)

The voltage and current characteristic curve of a TEG follows a linear response while the power and voltage follow a smooth normal curve with maximum power at a specific

voltage and current as shown in Figure 2.9 for (product code: GM250-449-10-12 by European Thermodynamics Ltd.) composing of 449 couples with each TEG physical size of 55mm×55 mm when operated at a ΔT of 220 °C (Montecucco et al., 2014). Both the voltage and power output are plotted on the same axis against current so as to see their response as current increases, it also helps to show the maximum power point of the thermoelectric generator.

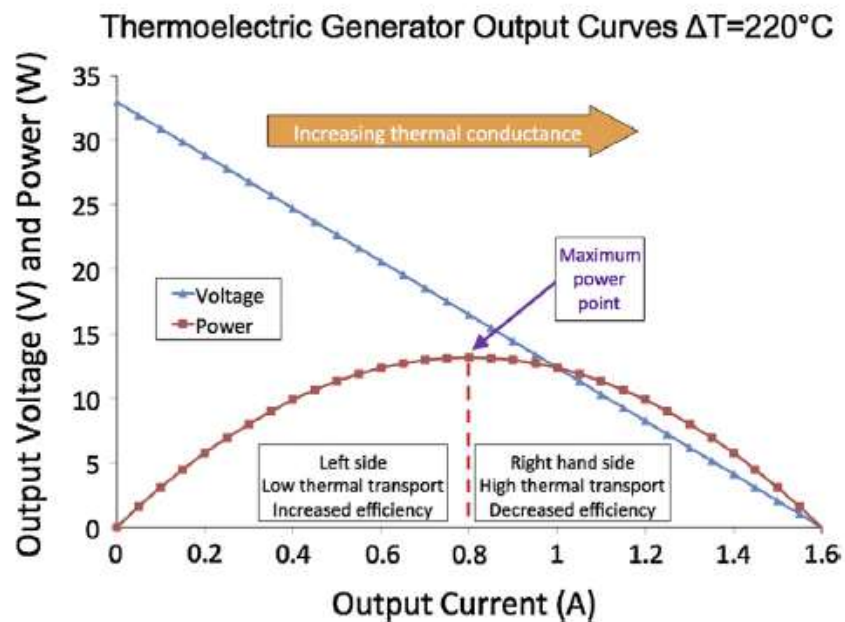


Figure 2.9: Voltage Current (IV) and Voltage Power (VP) characteristic curves of a TEG (Montecucco et al., 2014)

For a long time the efficiency of TEG has been low due to unavailability of suitable materials that have high figure of merit (Zt) at $Zt \geq 1$, but with advancement of nano technology, development of materials with higher Zt is anticipated (Sark, 2011). The efficiency of a TEG can be expressed using materials figure of merit as in Equation (2.8), (Musthafa, 2015).

$$\eta_{TEG} = \frac{\Delta T}{T_h} \left(\frac{\sqrt{1 + Zt\bar{T}} - 1}{\sqrt{1 + Zt\bar{T}} + \frac{T_c}{T_h}} \right) \quad (2.8)$$

where $\frac{\Delta T}{T_h} = \eta_c$ is the Carnot efficiency of the material, Zt is the figure of merit, $\bar{T} = (T_h + T_c)/2$, T_c is the cold side temperature and T_h is the hot side temperature of the TEG module where the Carnot efficiency can further be expressed as in Equation (2.9), (Sark, 2011);

$$\eta_c = 1 - \frac{T_c}{T_h} \quad (2.9)$$

There are five main parameters that govern the thermoelectric technology and within which it revolves; Seebeck phenomenon, Peltier effect, Thomson effect, Figure of merit and the Joule effect. Among them, only the Seebeck phenomenon, figure of merit and Joule effect are of interest for this study.

i. Seebeck phenomenon

The Seebeck phenomenon is due to the Seebeck coefficient of the pellet pairs of the thermoelectric materials (TEM) used, and is the link between the temperature difference across the TEM elements and the output voltage difference. The Seebeck coefficient depends on the thermal and electrical conductivity of the TEM and so determines the performance of the TEM and hence Seebeck voltage is developed at the couple junction as in Equation (2.10), (Enescu, 2019).

$$V_{sb} = \left(\frac{\alpha_A - \alpha_B}{\alpha_{AB}} \right) x \left(\frac{T_h - T_c}{\Delta T} \right) \quad (2.10)$$

where α_A and α_B are the Seebeck coefficients for conductor A and B in $V.K^{-1}$ and T_h and T_c are the hot side and cold side temperatures of the couple junction respectively.

ii. Figure of merit

The thermoelectric converter is basically a heat engine and hence obeys the laws of thermodynamics. Therefore, the figure of merit Z_T of a TEM is a dimensionless parameter of the material that determines its thermal conversion process from a temperature gradient to an equivalent electrical output. The figure of merit is symbolized by the letters Z_T as in Equation (2.11), (David M Rowe, 2006).

$$Z_T = \frac{\alpha^2 \rho}{K} \quad (2.11)$$

where α is the Seebeck coefficient of the material, ρ is the electrical resistivity of the material and k is the thermal conductivity of the TEM. The parameter $\alpha^2 \rho$ is referred as

the power factor that defines or evaluates the performance of the TEM. Currently, Bismuth telluride Bi_2Te_3 TEGs with Z_T of 1.5, lead telluride $PbTe$ with Z_T of 1.3 and silicon germanium $SiGe$ with Z_T of 1.2 are among the leading thermoelectric materials available for use (Sark, 2011; Selvan et al., 2019). But technology is developing materials that have Z_T ranging from 0.1 to 2.5 and research work in the field of Nano technology is very optimistic that materials of Z_T of 4 could be achieved in zigzag graphene Nano ribbons (ZGNR) by using line defects and edge roughness ZGNR (T. Zhang et al., 2017).

Recent studies also show Zt values up to 1.4 with graphene and C_{60} clusters synthesized by chemical vapor deposition (Olaya et al., 2019). Theoretical investigations reveal that higher Zt values of 2.2, 2.7, and even 6.1 at 300 K made from twisted bilayer graphene nano ribbons junction could also been realized (S. Deng et al., 2019). Figure 2.10 shows a road map for the progress made in TEG technology that shall result in improved figure of merit (Robert Freer & Anthony V. Powell, 2019).

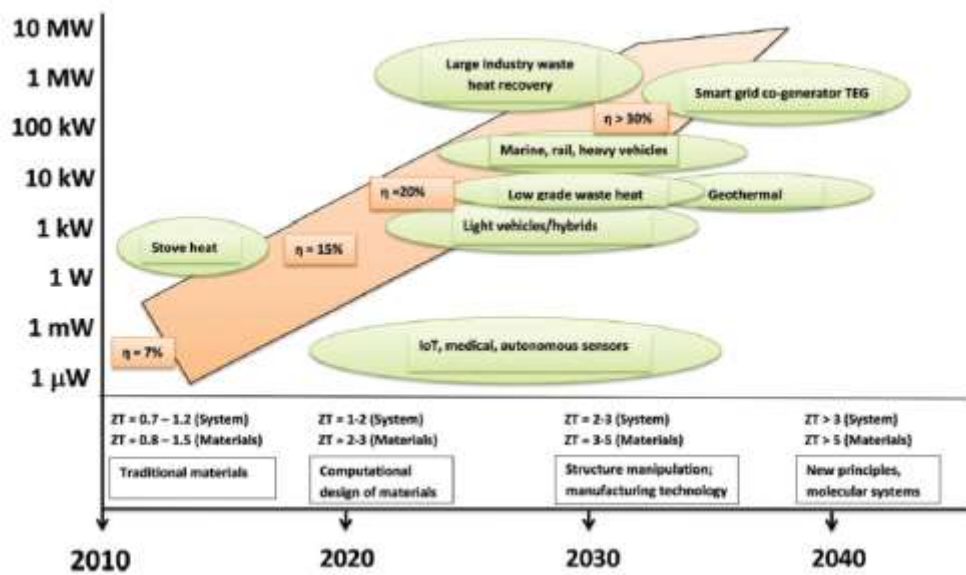


Figure 2.10: A Roadmap for the exploitation of thermoelectric technology, where ZT is the thermoelectric figure of merit and Z the efficiency (Robert Freer & Anthony V. Powell, 2019)

iii. The Joule effects

The joule effect is the joule heating that occurs when an electric current flow through a conductor and produces heat. The joule heating effect and heat conduction have a positive entropy change process and so the processes are irreversible in obedience to the thermodynamic laws. This effect occurs in TEGs when electric current flows through

conductors and semiconductors in the TEG pellet pairs due to the electric contact resistance and also when the TEGs dissipate heat to the surrounding environment (Enescu, 2019). Joule heat can be expressed as in Equation (2.12), by (Kanimba & Tian, 2016; Karami & Moubayed, 2014).

$$Q_{Joule} = I^2 R_{TEM,E} \quad (2.12)$$

where R represents all the electrical resistances in the TEM; internal resistance, conductor and contact resistance

iv. The Peltier effects

The Peltier effect was first observed by Jean-Charles-Athanase- Peltier a French physicist in 1834. He observed that when an electric current is passed through a single junction of a thermocouple consisting of different conducting materials A and B, heat is generated or removed at the junction. This effect has been exploited in the manufacture of heat pumps and in refrigeration for medical cooling equipment where multiples of such junctions are applied (A. Chen & Wright, 2012).

v. The Thomson effects

This effect was first observed by William Thomson in 1851. The effect explains why heating or cooling occurs in a current carrying conductor when a temperature gradient exists. The Thomson effect essentially combines both the Seebeck and Peltier effects. In their studies, (Giaretto & Campagnoli, 2020) concluded that increase of the Thomson effect could positively affect the Peltier performance if the Joule heat is reduced simultaneously.

2.4.1 Thermoelectric technology in waste heat recovery

The performance of TEGs is most suited for recovery of waste heat which would otherwise escape to the environment or result in reducing efficiencies of the systems developing it like in the case of PV power generation. Most processes and operations that use fossil fuels ranging from engines, boilers, furnaces, kilns, turbines and extruders, operate at very low efficiencies because of the excess heat that escapes to the surrounding environment. Figure 2.11 shows how TEG technology comes in handy in harvesting that waste heat (Enescu, 2019). By 2016, about 70% of the world's energy production escaped into the atmosphere as waste heat substantially contributing to global warming (Kanimba & Tian, 2016).

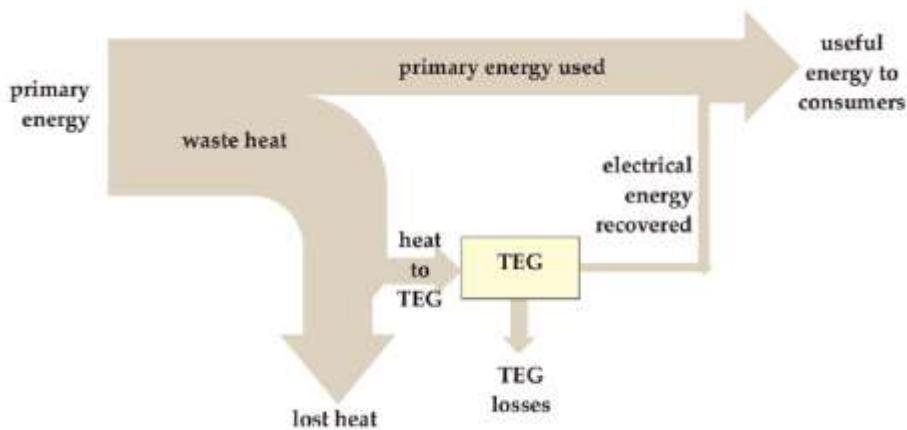


Figure 2.11: Schematic of waste heat recovery using TEG technology (Enescu, 2019)

In an effort to recover industrial and commercial waste heat, TEG technology has been applied for the recovery process in the space and airline industry as Radioisotope Thermoelectric Generators (RTGs) since the early 1960 to date, in the USA, Asia and Europe and extensively in countries like the former Soviet Union and present day Russia (Zoui et al., 2020). The technology has found wide application in the automobile and transport industry in Europe, USA and Japan where the exhaust heat is harvested before escaping to the environment (Shen et al., 2019). Nabil K. et al in their study in

modelling approach and validation of thermoelectric generator, they were able to model and simulate the effects of Seebeck and thermal effects in MATLAB Simulink. They were also able to develop equations that pave way for maximum power point tracking on TEG devices.

Figure 2.12 shows waste heat recovery TEG application in a BMW X6 model car in Europe where the TEG system recovers exhaust and flue gas waste heat to be used for battery charging and vehicle accessories. The TEG system is harvesting the waste heat from the automobile exhaust system and improves the efficiency of the automobile. Elsewhere, (K. Li et al., 2014) set up to develop a 1 kW thermoelectric generation system for industrial waste heat recovery where the TEG array consisted of 600 TEG modules of five parallel and twenty series modules. This technology has also been used in the marine and power generation industry (geothermal, thermal and photovoltaic) plants to harvest the waste heat for generation of electricity and to a lesser extent medical industry, in domestic appliances and watch manufacturing industry like Seiko and Citizen (Kishi et al., 1999).



Figure 2.12: TEG integration into the exhaust system of the BMW X 6 prototype model (Zoui et al., 2020).

2.4.2 Thermoelectric technology use in photovoltaic systems

As previously explained in the preceding section 2.2, solar PV cells are only capable of absorbing part of the electromagnetic spectrum from 100 nm which is the lower Ultra-Violet (UV) range to 1100 nm which is also the lower Infra-Red (IR) range and the rest of the spectrum radiant energy ends up heating the cell significantly reducing its efficiency at high cell temperatures (Xu et al., 2015). This phenomenon results in generation losses and has hence provoked a lot of global studies concentrating on redeeming the losses caused by the high temperatures especially in the tropical and sub-tropical regions.

Many methods have been developed and some used so far ranging from passive water floating PV to active pumped cold water PV cooling, use of nano fluids, micro channel heat sinks, phase change materials, fins and even design of high absorption and multi-junction PV cells in an effort to mitigate the effects of high PV cell temperatures as mentioned in section 2.2.2. The use of Thermoelectric Generators (TEG) to absorb the heat from the hot PV modules and generate electricity is developing into a suitable alternative method as it enables the full utilization of the solar radiation spectrum (G. Li et al., 2017).

Li .K. et al (2014) demonstrated that besides cooling and generating electricity, TEG modules are noise free, static, environmentally non-polluting, highly reliable and compact in stature making them very suitable for hybrid application with PV systems who have similar features (K. Li et al., 2014). Studies by Dallan, et al (2017) observed that TEG modules can absorb the heat from the PV modules and convert it into electricity hence can increase the electricity generation efficiency of the PV + TEG system by up to 3.9% depending on the temperature gradient achieved (B.S Dallan et al., 2015). Elsewhere, Hashim H. et al (2015) developed a model for PV-TEG hybrid system

geometry optimisation to achieve increased overall power output and conversion efficiency (Hashim et al., 2016).

Jin Zhang et al (2014) conducted a study to investigate the performance of PV-TEG hybrid systems where they used c-Si PV cells, p-Si TFPV cells, CIGS PV cells and polymer solar cells. The study was conducted using an optical concentrator where the concentration ratio was varied and its effects on the system efficiency observed as in Figure 2.13. Increase of concentration ratio resulted in noticeable increase in the PV-TEG system for the silicon and CIGS PV systems while the same action lowered the efficiency of the polymer PV. The same action did not increase the efficiency of the c-Si PV as compared to the other systems. They also observed that temperature is a dominant factor that affects the conversion efficiency of such hybrid systems and that thermal contact resistance also highly influenced the efficiency of the systems.

In their conclusion, among the systems investigated, the hybrid CIGS-PV system had the highest efficiency though its cost is higher compared to the other systems and generally the TEG enhanced the system efficiency remarkably (J. Zhang et al., 2014).

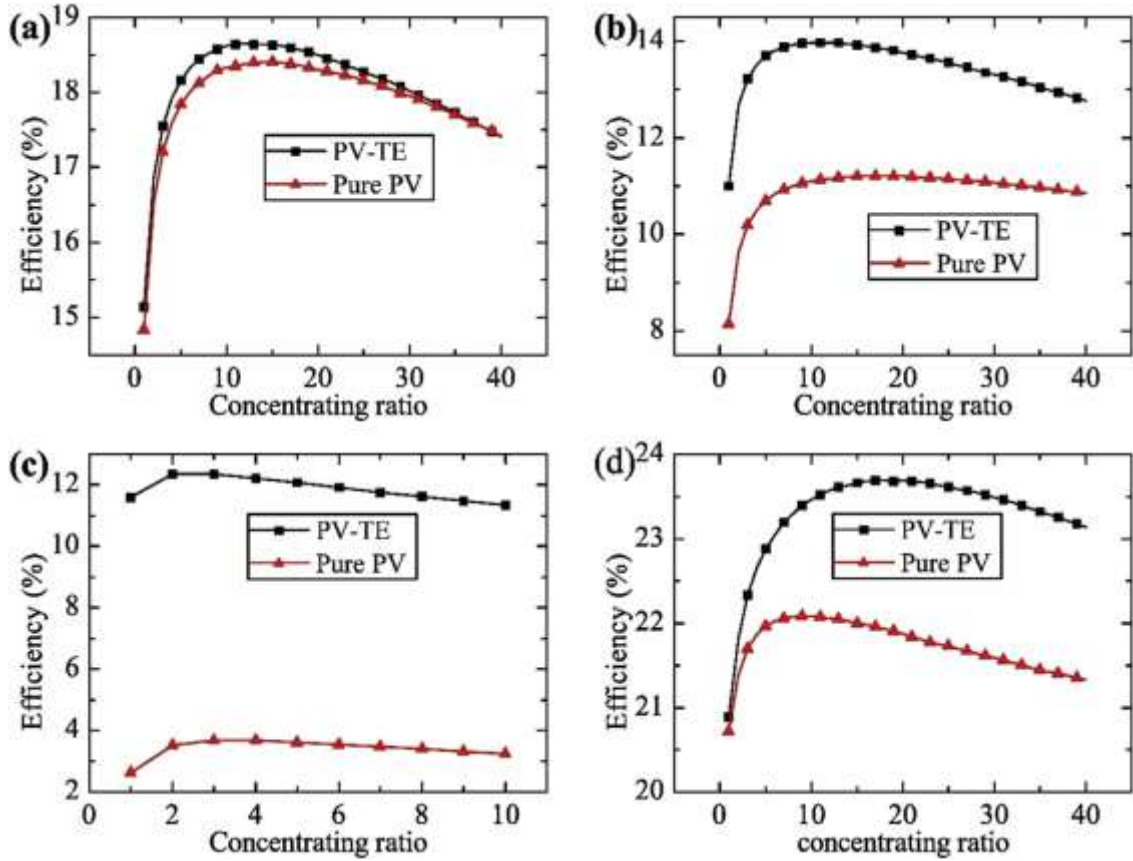


Figure 2.13: Efficiency of PV-TE as a function of concentrating ratio: (a) c-Si PV, (b) p-Si TFPV, (c) polymer PV, (d) CIGS. (J. Zhang et al., 2014).

Akbar R.N. et al (2017) implemented a TEG cooling in extreme temperatures and observed that TEGs are capable of absorbing the energy of the Alpha, Beta and Gamma particles in addition to the complete electromagnetic spectrum to generate electricity (Nejad et al., 2017). In his studies, Van Sark (2012) showed that the efficiency of a PV-TEG system could be improved by between 8% to 23% using thermoelectric materials (TEM) with a figure of merit, Zt of 1, and further improvements could be achieved when the cold side temperature of the TEG is maintained at 25 °C (Sark, 2011).

2.5 Effects of temperature mismatch in hybrid TEG systems and mitigation methods

Though TEG technology is gaining popularity in the field of PV systems cooling to improve the system efficiency and also utilize the heat to generate electricity, its penetration in the field is challenged by improper thermal coupling between the heat generator (PV) and the TEG systems resulting into unsatisfactory results. Normally PV cells temperature rises during operation and the temperature distribution is not uniform over the entire face of the PV module.

In their study, (Tina & Abate, 2008) conducted an experimental study to verify thermal behaviour of PV modules cells by measuring the temperature of 3 separate cells on the same module when subjected to uniform irradiance and obtained a temperature difference of between 2 °C and 5 °C between the cells. This non-uniform distribution of temperature causes hot spots and results in reduction of efficiency and eventual structural damage due to thermal fatigue caused by thermal cycles and stresses (Ferrara & Philipp, 2012). When this non-uniform cell temperature is subjected to TEG modules, they sense different hot side temperature, T_h that directly affect the temperature gradient, ΔT which is responsible for voltage generation.

Montecucco A. et al (2014) carried-out studies to investigate the effects of temperature mismatch on both parallel- and series-connected TEG arrays and observed a power loss of 9.22% and 12.9% for the series and parallel connected arrays, respectively, compared to the expected maximum power output. Their experimental results showed that power lost under mismatch conditions (temperature, mechanical loading, manufacturing tolerances and aging) can be significant and was observed to be lower for series connected arrays compared to the parallel connected arrays. This was because in the parallel connected TEG the voltage is lower and current higher as compared to the series connected arrays, and this increases the I^2R losses (Joule heat) in the wiring circuit.

They were able to provide a mathematical formulation (from experimental characterization of TEGs) and electrical circuit equations that together can be used to predict the electrical power output in any temperature mismatch situation. They analysed 3 TEGs but their results could be adapted for more TEGs (Montecucco et al., 2014).

Zhou J. et al (2016) further analysed a solar cell temperature distribution using a simulation model and observed that under 1000 W/m^2 irradiance, 1 m/s wind speed and 300 K ambient temperature, the temperature of the cell is highest at the centre at 331.76 K and lower along the side edges with a difference of 0.68 K and much lower at the diagonal corners with a higher difference of 1.2 K (Zhou et al., 2015).

In mitigating the undesirable effects, Z.B Tang et al (2015) set up a test bench at the University of Technology in Wuhan China to study the effects of mismatch conditions for thermoelectric materials and thermoelectric generators using an automotive engine. They set up six $50 \text{ mm} \times 50 \text{ mm}$ sets of thermoelectric modules and connected them in a series formation first and later in a parallel formation. The thermoelectric modules were clamped using a spring-loaded clamping device and observed for direct heating; from a bare heated surface and insulated heating from an insulated and heated surface. While working on TEG electrical performance under temperature mismatch conditions they observed that proper mechanical pressure on the module improves the electrical performance of the TEG and its power loss reduced from 11% to 2.4% and the power output increased 17.3 W, 22.5% more than the power generated when the TEG has no thermal insulation (Tang et al., 2015).

Miguel F. et al (2013) also developed a model combining the PV and TEG technologies in one semiconductor and obtained satisfactory results in increasing the efficiency of the PV-TEG under extreme temperature conditions (Fisac et al., 2014). Essentially, temperature mismatch on TEGs could result due to inadequate mechanical clamping force, poor thermal contact of the TIM and even due to the thermal conductivity (k) of the TIM used where in many occasions system designers are never aware of its effects which ultimately result in avoidable system power loss (Montecucco et al., 2014). In

their study, Yin E. et al (2017) recommended the use of adhesive TIM between the PV cell and TEG module for good thermal conductivity (Yin et al., 2017). Zhou et al (2017) investigated the performance of tempered glass and aluminium alloy sheets as module back sheet for temperature distribution by varying their thickness and observed that Type 6061 aluminium alloy sheet performed better than other back sheet materials (Zhou et al., 2017).

Cheng-Ting H. et al (2016) proposed a concept of “effective Seebeck coefficient” to address the effects of temperature mismatch in Bi₂Te₃ TEG modules and used different clamping forces 18 Kg/W (0.634 Kg/cm²) and 12 Kg/W (0.432 Kg/cm²) in their setups and observed that the amount of clamping force changed the Seebeck coefficient making it superior when higher clamping force is applied. They further investigated the effects of thermal resistance by analysing the resistance and they subsequently constructed a thermal resistor network that was used to obtain the proposed “effective Seebeck coefficient”. The investigation enabled them conclude that there is more than 30% inconsistency between theoretical coefficient α_T and the measured one α_M so proceeded

to define “effective Seebeck coefficient” α' (Hsu et al., 2011) as in Equation (2.13),

$$\alpha' = \frac{V}{\Delta TEG} = \frac{V}{0.8742(T_h - T_c)} \quad (2.13)$$

Elsewhere, Nagayoshi H. et al (2006) developed a novel MPPT control method for mitigation of power loss due to temperature mismatch in TEG power systems. In their study they used the virtual load conductance of the load as feedback so as to control and maintain the same value of conductance in the TEG system using a DC-DC converter

circuit between the TEG array and the load. Their prototype DC-DC converter circuit exhibited very good tracking performance against the load changes and temperature difference with wide matching ability of the load (H. Nagayoshi & T. Kajikawa, 2006). Figure 2.14 shows plotted curves of how the DC-DC converter would control the virtual load line of the TEG while operating in back and boost modes to mitigate the effects of power loss due to temperature mismatch in TEG systems.

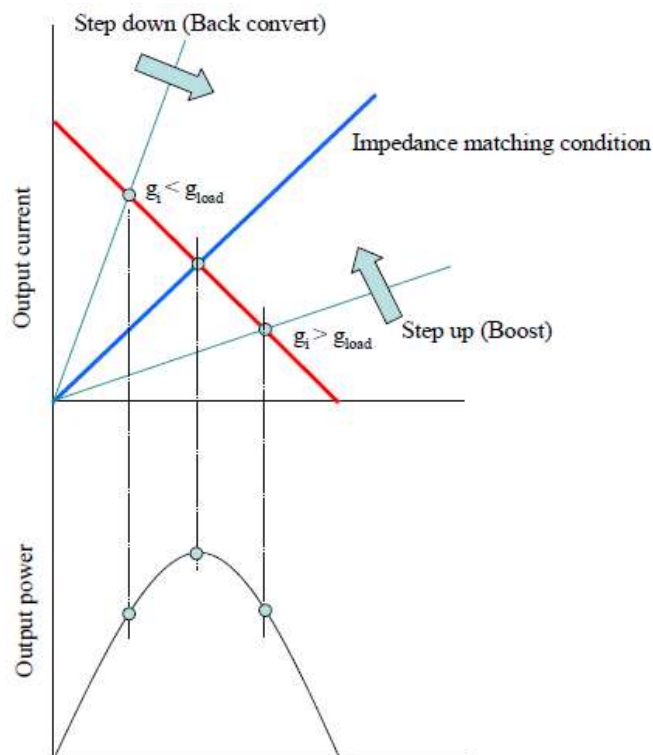


Figure 2.14: Correlation of load line and output power of TEMs. The virtual load line can be controlled by DC-DC converter (H. Nagayoshi & T. Kajikawa, 2006)

Further, Kai Sun et al (2016) set up to study and develop methods that would improve the poor conversion power efficiency that is caused by power mismatch due to unbalanced temperature difference distribution on a conventional series connected TEG with a centralized converter system. They proposed to use two methods based on differential power processing (DPP); the centralized –distributed hybrid structure and

the cascaded power transfer structure both of which would realize the Maximum Power Point Tracking (MPPT) of each TEG module. The architecture, topology and operation principle were analyzed and experimental verification was done (Kai Sun, & Zhaoxin Qiu, Hongfei Wu, 2016).

2.6 Summary of Gaps

In the review done it has been observed that modeling of TEG P-N pellet pairs in MATLAB Simulink has been attempted by very few researchers making the understanding of the internal behavior of the device very limited in the field. Nabil Karami et al (2014) developed a model to study the performance of TEGs to study the effects of matching the internal resistance to the load but did not carry out laboratory measurements on series TEGs. Montecucco A. et al (2014) did some studies on the effects of parallel and series interconnection of TEGs but the features are still highly uncharted.

The effects of PV cell temperature mismatch and methods of mitigating them have also not been investigated especially using cell mapping techniques on an entire PV module including analytical cell temperature techniques. Li kewen et al (2017) conducted studies on TEG efficiency at different figures of merit and varying temperature in geothermal environment only. Elsewhere, Jin Zhang et al (2014) observed high thermal resistance resulting from the surfaces roughness of PV and TEGs, but did not investigate effects and mitigation methods.

Tina G.M carried out studies and observed PV cell temperature difference but did not conduct intensive cell temperature mapping and measurements including the effects of mismatch on TEG voltage. Nagayoshi et al (2006) only undertook to resolve effects of power loss due to temperature mismatch using DC-DC converters as mentioned.

It has therefore been observed that rigorous PV cell temperature mismatch studies and measurements have not been done and also TEG modelling in MATLAB Simulink and

interconnection methods have not been conducted exhaustively, and these gaps in TEG modeling in MATLAB Simulink, PV cell temperature mapping and measurements have been the impetus for this research work. MATLAB Simulink was preferred over other simulation software's because of its compatibility with other PV design software's and it is also rich in mathematical functions

Further, our comprehensive review to the best of our knowledge, reveal that, studies on mediating temperature mismatch due to varying individual PV cell temperatures has not been carried out extensively. This temperature mismatch and good thermal coupling of PV-TEG matrices significantly affects the performance of these two technologies when operated as a hybrid.

CHAPTER THREE

METHODS AND MATERIALS

3.1 Preliminary Data Collection at JKUAT –IEET for PV-TEG Hybrid System Development

This chapter deals with materials and methods used to design the PV+TEG standalone system for a recirculation aquaculture system in Nyalenda Kisumu. The research work starts with collecting preliminary data at the JKUAT IEET awaiting the acquiring and securing of the site in Nyalenda Kisumu and later when the site is secured, data collection continues on site and construction is done. Studies are done both on site and laboratory environment to mitigate effects of temperature on PV cells and also effects of PV temperature mismatch on TEG power generation. Thermal interface materials are used to study the effects of PV cell temperature mismatch and TEG voltage generation.

3.1.1 Introduction:

The objective of this section of the study is to collect preliminary data at the Institute of Energy and Environmental Technology (IEET) JKUAT site that would be used to carry out the initial studies on PV system and PV-TEG systems behavior under cooling environments. This initial data would create the roadmap towards the design and developments of the PV-TEG hybrid system that would be used to supply electrical power to the autonomous Recirculation Aquaculture System (RAS) in Nyalenda Kisumu.

This exercise was carried out in Juja, awaiting the acquiring and securing of the actual Nyalenda site for data collection, to provide preliminary local data that would be used for the initial design before site data was available for final design and subsequent PV+TEG system development. The Juja site within the Jomo Kenyatta University was selected for security of equipment storage of equipment and materials and availability of appropriate site for carrying out measurements. During the one-year period, 24-hour

irradiance and temperature data was collected and specific setups were fabricated to collect data to enable study of effects of temperature on both PV and PV-TEG systems. Juja is located 1.16° south of the equator as compared to the actual Nyalenda Kisumu site that is located 0.16° south of the equator so it served as a good site for initial data collection. The data collection exercise in Juja was carried out for a period of 1 year.

When the site in Nyalenda was acquired and secured, site data collection started and was also done for one year at Nyalenda. This data was then used in the final design of the PV-TEG system that will supply power to the RAS as explained in section 3.2 of this chapter. Further in sections 3.3 and 3.4, specific studies are carried out to investigate the factors that affect the performance of the PV-TEG systems. Finally, in section 3.5, the economic analysis has been done to assess the viability of the PV-TEG system.

3.1.2 Weather Monitoring Station Setup

The irradiance and temperature measurement setup were fabricated on the roof where the Pyranometer was mounted on the tiled ridge of the roof and the temperature thermocouples were mounted under the PV module that was installed on the roof also. The ambient temperature was measured at an exposed external spot 600 mm above the roof surface, then the three sensors were connected to the COMBILOG 1022 data logger that was mounted on one of walls in the laboratory at the second floor of the IEET building of the University. The Pyranometer was calibrated by the manufacturers KIPP&ZONEN with a sensitivity of $11.94\mu\text{V/W/m}^2$ at normal incidence. The calibration was done following ISO 9846 paragraph 5 as hierarchy of traceability. The measurements were performed in Bohemia NY (latitude 40.780 , longitude -73.105 altitude 26m above sea level). The data logging schematic has been presented on Figure 3.2. The pyranometer was measuring irradiance while TC1 and TC2 were measuring PV cell temperature and ambient temperature respectively. The physical mounting on the roof has been shown in Figure 3.1.



Figure 3.1: The CMP-3 Pyranometer on the IEET building roof

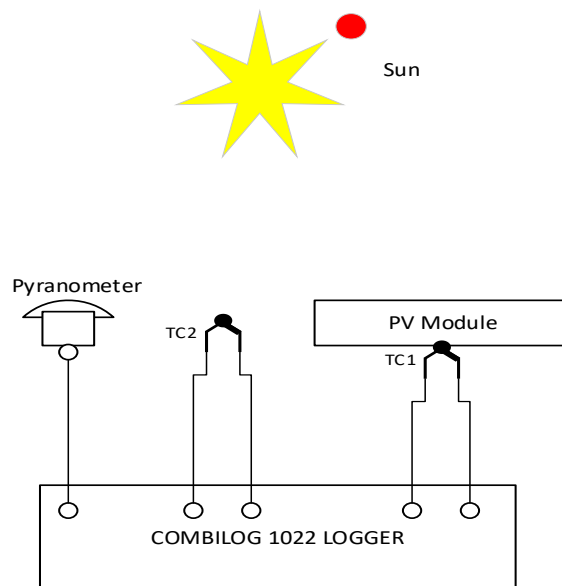


Figure 3.2: Schematic of the Weather Station data logging setup

3.1.3 Specific Setups for PV Temperature and Voltage Measurement

The specific setups (SS 1- SS 4) for PV module temperature and voltage measurements were fabricated to measure cell temperature and PV voltage output under varying irradiance where one module is in conventional mode and another under cooling mode. The specific setups were fabricated to investigate the different methods of cooling using air and water. Before the setups were fabricated, the characterization of the PV modules was done as shown in Figure 3.3.

3.1.3.1 PV Module Characterization

The PV modules used for the setup's measurements were subjected to characterization as shown in Figure 3.3. The modules were subjected to uniform irradiance and their open circuit voltages were measured to be compared. Their short circuit currents were also measured and compared. The PV modules were selected from a set of modules from the same manufacture and then characterized before use. For each setup, modules were selected and characterized before the specific measurements were done.

Ambient and PV cell temperature was measured but were not plotted because the conditions were exactly the same and the curves literally over traced each other. The aspect of temperature was however not considered under the characterization process.

The sampling criteria used was same power rating, same type of cells, same voltage and current ratings and same manufacture. The same method was used for the TEGs. The thermal interface materials and other consumable materials were imported and used following the manufactures specifications as procured and not subjected into any characterization process.



Figure 3.3: Characterization of the PV Modules

3.1.3.2 SS-1 PV Module Irradiance Temperature and Voltage Measurement under Air Cooling

Figure 3.4 shows the setup for the PV modules temperature and voltage measurement under air cooled environment. This set up was done where there is no possibility of shadow at all apart from cloud cover that would affect the whole set up the same way. Other following set ups were also done under conditions of no shadow at all and the setups were under close monitoring. The DNI data collected from the roof mounted pyranometer was checked out with the spot measurements DNI done on the ground level as the measurements were in progress and the irradiance data was the same all through.

The setup was fabricated using two modules mounted on a surface and tilted at an angle less than 15° facing north to the equator.



Figure 3.4: PV Module Temperature Measurement under Air Cooling

3.1.3.3 SS-2 PV Module Irradiance and Voltage Measurements under Air and Water Cooling

In this setup the PV modules temperature and open circuit voltage measurement was done under air cooling and water-cooling conditions as presented in Figure 3.5.



Figure 3.5: PV Module Temperature and Voltage Measurement

3.1.3.4 SS-3 PV Module Irradiance Temperature and Voltage Measurement

In this setup the PV module temperature and voltage measurement was performed under water cooling and air-cooling conditions while both modules cooling is enhanced using the ALUCORE cooling panel as shown on Figure 3.6. Here also, TEG modules were mounted on the Alucore cooling panel sandwiched between the PV- PVF back sheet and the cooling panel. The irradiance was measured using the weather station setup on the roof of the IEET building.



Figure 3.6: PV Module Temperature and Voltage Measurement

3.1.3.5 SS-4 Battery Charging Conventional and Water-cooled PV Systems

Specific setup SS-4 was fabricated for charging and discharging batteries. The setup was fabricated using a battery loading bank and a battery charging system. The battery charging power was obtained from the PV systems that was fabricated and setup outside the laboratory as shown in Figure 3.7. Figure 3.8 shows the battery loading bank or the

load system that was used for discharging of the batteries. The setup fabricated for the measurements is shown in Figure 3.9.

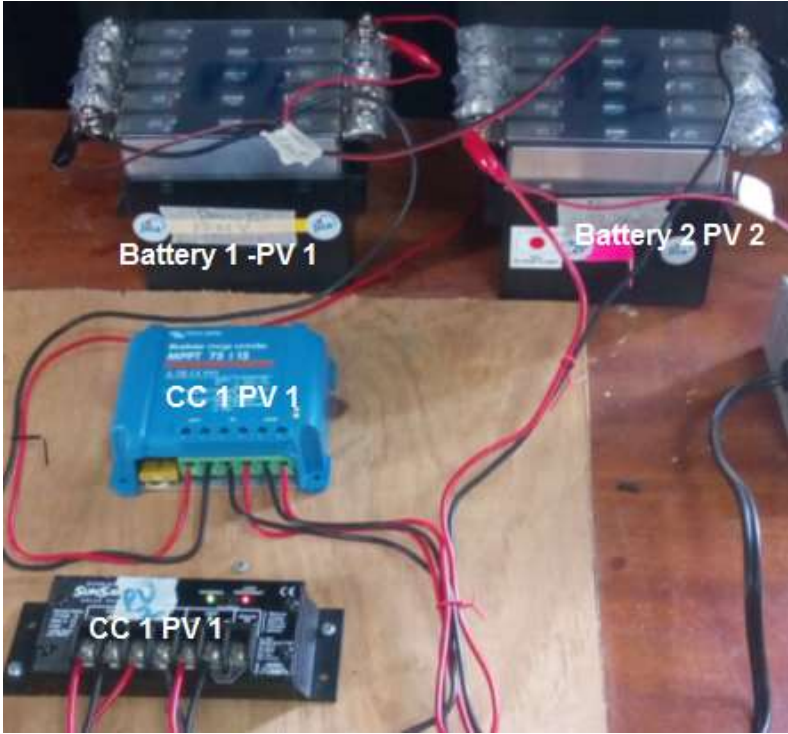


Figure 3.7: Battery Charging Voltage and Current Measurement

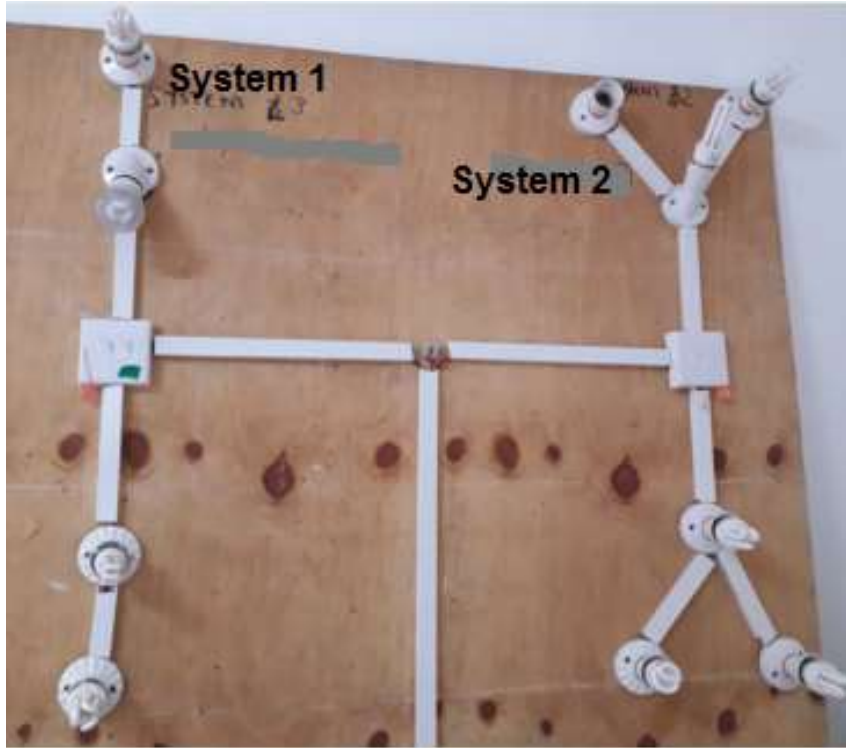


Figure 3.8: Battery Loading Lighting Bank



Figure 3.9: Battery Charging PV Temperature, Voltage and Current Measurement

3.2 Site Studies for Design of the PV-TEG Hybrid System to Run the Autonomous Aquaculture System

3.2.1 Introduction

After the acquisition and securing of the VicInAqua site at Nyalenda Kisumu, all the instruments were moved to site to continue with specific site data collection. The site in Nyalenda is located in Kisumu near the sewerage management and maturation ponds, about 1.2 kilometers off the Kisumu-Kericho highway. The Nyalenda site geographical coordinates are -0.2499N and 34.9166E.

The recirculation aquaculture system main function is to filter solid material from the used water from the fish ponds and then return the same water back to the ponds for use by the fish. This process is done a membrane bioreactor and water pumping network in the RAS. Next to the identified site there are large sewerage maturation ponds that are used by the Kisumu municipality for waste management, and would be an ideal place for disposing solid waste from the fishes and fingerlings. Therefore, the solid waste generated in the plant can be channeled to drain into the adjacent ponds.

Here, site specific data on irradiance, temperature and electrical power data were collected to be used for the final design of the system. The weather station was used to collect 24-hour irradiance and ambient temperature data like in the case of IEET-JKUAT. Other specific setups were fabricated to study specific system features. The site data collected were then fitted and harmonized with the expected RAS electrical load requirements to develop the PV-TEG design.

The design made, will provide for full load daily 8-hour operation and night time essential load operation plus an allowance of 3 Days of Autonomy (DOA) battery storage for consecutive cloudy days. The design shall use Lithium-ion type batteries so that 70% Maximum Depth of Discharge (MDOD) equivalent to 30% Minimum State of Charge (MSOC) is provided for the system energy capacity. The system is designed to

switch to essential load when the DOD attains 30% at all times. Nevertheless, the battery bank is capable of attaining 100% DOD on manual operation when the allowed days of autonomy are exceeded.

3.2.2 Instruments Sensors Components and Fixtures

Most of the instruments used at the IEET-JKUAT site were transferred and used at the RAS site in Nyalenda Kisumu. A list is presented in Table 3.1 showing the instruments used and whose specifications are tabulated in the fifth chapter. Additional instruments and components used for specific setups are also listed individually in chapter five.

Table 3.1: List of Instruments, Sensors and Devices

S/N	Name and Type of Device	Quantity Measured	No.	Range	Accuracy
1	COMBILOG 1022 Data logger	Irradiance, temperature and	1	Voltage $\pm 10V$ Resistance $20K\Omega$ Current $25mA$	0.05%
2	KEYENCE NR 500 logger	Voltage, temperature	1	$-55V$ to $50V$, $-100^{\circ}C$ to $1000^{\circ}C$	$\pm 0.05\%$ of FS
3	CMP 3 Pyranometer	Irradiance sensor	1	$0-250^{\circ}C$, $3000W/m^2$	11.94 $\mu V/W/m^2$
4	Thermocouples PT-100	Temperature sensor	3	$-80^{\circ}C$ to $200^{\circ}C$	$\pm 0.05^{\circ}C$
5	TENMARS TM-208 solar meter	Irradiance	1	$0-2000W/m^2$	$\pm 3\%$ at $1000W/m^2$
6	Infra-red thermometer AD-5615	Temperature	2	$0-1000^{\circ}C$	$\pm 1\%$, $\pm 0.012^{\circ}C$
7	Multi-meters HIOKI 3287	AC/DC voltage, current, resistance	2	$0-600V$ $0-1000A$, $0-420\Omega M$	$\pm 2.3\%$ $\pm 1.5\%$ $\pm 2\%$
8	Thermocouple wire	Temperature sensor	10	$-270^{\circ}C$ to $1372^{\circ}C$	$\pm 0.75\%$
9	Thermoelectric Generator	Electricity generation device	200	$4.8V$, $669mA$	
10	PV modules	Electricity generation device	4	$21.6V$, $0.8A$	

3.2.2.1 Plastic Tube Water Pool

The plastic water tube normally comes deflated when not in use but can be air inflated to form a pond shape where water is filled to form a water pool. This water pool was then used to float a large size PV module for specific setups on site. Figure 3.10 shows the air inflated plastic tube being filled with water.



Figure 3.10: Water Pool on site Kisumu

3.2.3 Weather Monitoring Station Setup in Kisumu

The same instruments used in weather monitoring in IEET-JKUAT are moved to Kisumu and installed on site at Nyalenda to collect 24-hour data needed for the final design of the PV-TEG hybrid system. The instruments comprise of a CMP-3 pyranometer that is moved and installed on the roof edge of the site laboratory building as shown in Figure 3.11 and the COMBILOG 1022 data logger is also mounted on the site laboratory wall as shown in Figure 3.12. One 13 Wp PV module is installed on the roof in conventional air-cooled mode to be used for the measurement of the module cell

temperature as shown in Figure 3.13. The site ambient temperature is measured using a PT100 thermocouple and data stored in the same data logger.



Figure 3.11: CMP-3 Pyranometer in Nyalenda Kisumu



Figure 3.12: COMBILOG 1022 Logger in Nyalenda Kisumu



Figure 3.13: PV Module Temperature Measurement

3.2.4 Specific Setups for PV Temperature and Voltage Measurement

Following successful movement and installation of the weather station in Kisumu, other specific setups are fabricated for measurement of module cell temperature and PV voltage mainly under conventional air cooling and water-cooling conditions. Kisumu is a lake shore city in Kenya that has sufficient water with many rivers and streams draining into the adjacent Lake Victoria from the highlands.

3.2.4.1 Specific Setup 1 for Site Roof Mount PV Temperature and Voltage Measurement

This specific setup is fabricated on the new roof where there is open space and no shading as shown in Figure 3.14. The conventional PV module is mounted on the roof leaving a clearance of 200 mm for free circulation of cooling air as in Figure 3.14 (a). The water-cooled PV module is clamped to an Alucore honey comb aluminum cooling panel sandwiching 10 TEG modules and made to float on water in a vessel as in Figure 3.14 (b).

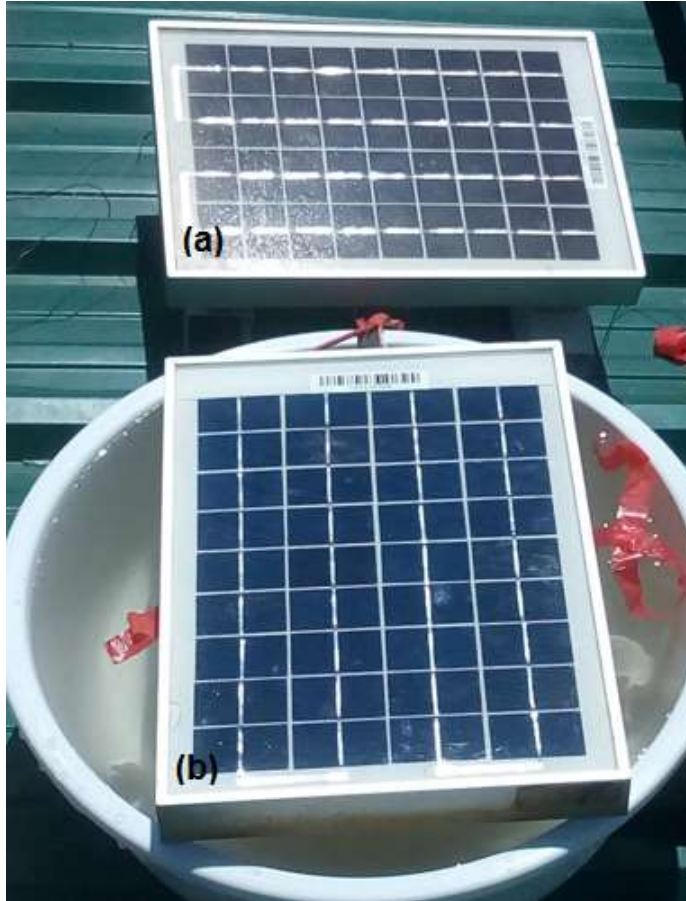


Figure 3.14: PV Parameter Measurements (a) Air (b) Water cooled

3.2.4.2 Specific Setups 2 for PV Ground Mount Temperature and Voltage Measurement

This specific setup is fabricated to carry out temperature and voltage measurements on the design size sample PV-TEG system where some TEG modules are stuck behind the PVF back sheet to measure the TEG output under the site irradiation conditions. The PV module is then made to float on a water pool created using a plastic tube, while the PV

cell temperature, output voltage and TEG output voltage measurements are being carried out. Figure 3.15 shows the PV module floating on the water while Figure 3.16 shows part of the data collection system used in the measurements.



Figure 3.15.: PV Module Temperature and Voltage Measurements



Figure 3.16. PV Module Temperature and Voltage Measurements

3.3 TEG Modeling and Test Bench Fabrications

3.3.1. Introduction

The objective of this section of chapter 3, is to study the internal operation of the TEG with an intension of identifying the TEG internal parameters that affect their performance in generating electricity from waste heat recovery. Herein, a TEG model is developed and simulated using MATLAB Simulink platform to study the internal features and their performance under externally induced heat flux. The model has been validated and can be used to optimize TEG operation especially in low heat flux systems like the solar PV systems. Test bench fabrications have also been developed to study the TEG interconnection alternatives with an intention of identifying and selecting the best connection methods at single and multiple TEG module connections and the different interconnection losses have been investigated in the process. In this section of the chapter the design of the PV-TEG hybrid system for the autonomous RAS has been done; matching the anticipated RAS load to the power generation capacity and energy storage.

3.3.2 TEG Numerical Model Development

In PV-TEG systems, the PV cell waste heat recovery is accomplished using TEG modules. The TEG modules absorb the waste heat developed by the solar cells and sink it to a medium or the environment hence lowering the operating cell temperature. These modules are composed of electrically series-connected and thermally parallel-connected P-N junction pairs. Normally in one TEG module, there are practically about 127 P-N junction pairs or pellets (Kolambekar & Bhole, 2015). When the electrically series-connected P-N junction pairs are subjected to a temperature gradient (ΔT) between the two faces of the modules ($T_h - T_c$), they generate electromotive force (EMF) and current flows according to the Seebeck phenomenon (David M Rowe, 2006). When the TEG modules are interconnected in series, their voltages add up and when they are connected

in parallel formation their currents add up. Hence the current and voltage levels matter when interconnecting the modules or module strings.

3.3.2.1 Numerical Model Development /Setup

For purposes of modelling the TEG module, the collected PV module temperature data at the study site are used. The data is obtained from the field weather station setup at Nyalenda Kisumu where the observed maximum PV cell temperature was 69.2 °C. Using this maximum cell temperature, a TEG with medium ΔT of 10 °C - 100 °C and maximum hot side temperature T_h of 150 °C is selected and its parameters evaluated for simulation purposes. A mathematical model is developed and simulated on a MATLAB Simulink platform.

In a PV-TEG hybrid power generation system, the thermoelectric generator pellet is both a thermal absorber and an electric generator combining the two functions to achieve electricity generation and essentially functioning as a heat pump (Jradi et al., 2012). Therefore, to accurately model the TEG pellet, all the possible thermal and electrical parameters are considered. The model can be thought of as an electric generator encased in a thermal vessel consisting of the P and N pellets combination conducting heat in one direction of flow from the hot side as, Q_h at temperature, T_h to the cold side as, Q_c at temperature, T_c as shown in Figure. 3.17. The model in Figure 3.17 defines the contact thermal resistance R_{ct} of the Thermoelectric Material (TEM), the thermal resistance R_{et} of the P and N elements of the TEG, T_h and Q_h as the temperature and heat respectively, at the hot side of the pellet and T_c and Q_c as the temperature and heat, respectively, at the cold side of the TEG.

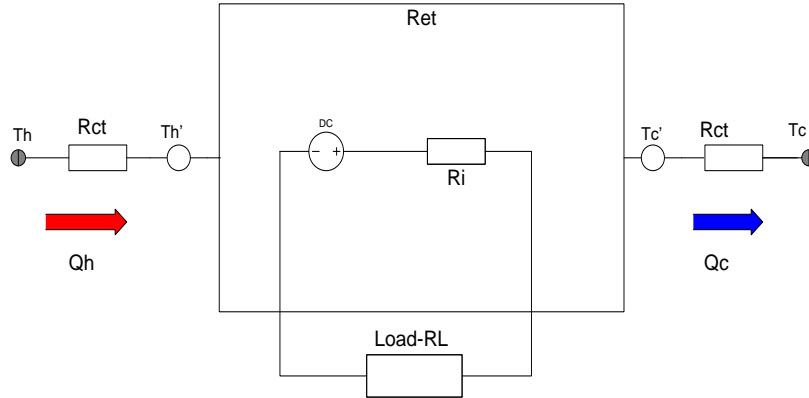


Figure 3.17: Thermoelectric Generator model block diagram

3.3.2.2 The Electric Model of a TEG

In the electric model, R_i and R_L are the TEG internal electrical resistance and the load resistance, respectively, where the internal electrical resistance of the TEG includes the electrical resistance of the TEM and the contact resistance of the associated connecting conductors (Saima Siouane, et al., 2016). During the implementation of simulations on the developed model, heat, Q_h is applied on one side of the module that consequently raises the temperature to Q_h with conductive heat transfer taking place across to the module to the cold side to appear as Q_c and the temperature as T_c as shown in Figure 3.18.

Temperatures T_h and T_c creates a temperature gradient, ΔT that enables the TEG to generate electricity based on the Seebeck phenomenon where the N element assumes the positive polarity and the P element, the negative polarity as shown in Figure 3.18. The fundamental internal and external parameters of the TEG pellet used in the model are listed in Table 3.2 and Table 3.3, respectively. The parameters were obtained from the manufacture of the thermoelectric generator as part of the technical specifications. The input parameter was the source heat as modeled and the output parameter was the D.C voltage generated by the TEG.

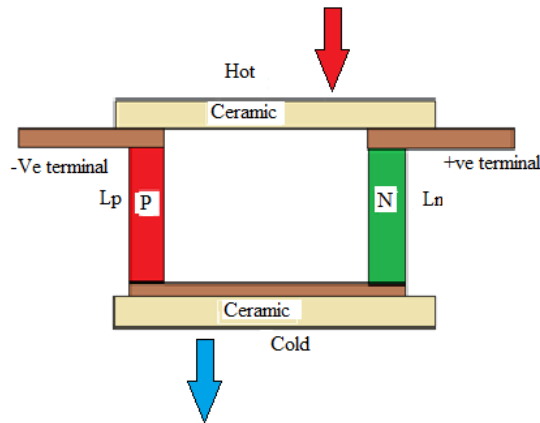


Figure 3.18: Thermoelectric Generator Physical Structure

Table 3.2: Internal Parameters of a TEG Module

Serial	Parameter description	Symbol
1	Seebeck coefficient for the P element	α_p
2	Seebeck coefficient for the N element	$-\alpha_n$
3	Electrical resistivity for the P element	ρ_{pe}
4	Electrical resistivity for the N element	ρ_{ne}
5	Electrical internal resistance	R_i
6	Length of the P element	L_p
7	Length of the N element	L_n
8	Area of the P element	A_p
9	Area of the N element	A_n
10	Thermal resistance of the pellet	R_{th}
11	Terminal resistance of connectors	R_c
12	Number of pellets	N

Table 3.3: External parameters of a TEG module

Serial	Parameter description	Symbol
1	Temperature gradient	ΔT
2	Hot side temperature	T_h
3	Cold side temperature	T_c
4	Thermal conductivity layer	C_{tl}
5	Load resistance	R_L

The governing equations used in the setting up of the electrical performance model of the TEG are hence developed as follows;

The open circuit voltage or Seebeck voltage for a single pellet of the TEG is given as (David M Rowe, 2006; Kanimba & Tian, 2016);

$$V_{oc} = \Delta T \alpha \quad (3.1)$$

Where, α is the Seebeck coefficient of the thermoelectric materials (P and N) and ΔT is the temperature gradient between the hot and cold sides of the TEG. For a whole TEG module, the Seebeck coefficient is multiplied by the number of pellets in the module which is typically 127.

The power generated by the TEG or the output power P_o can be expressed as; $I^2 R$. So, the power output from the TEG for one TEG pellet is given as in (Kanimba & Tian, 2016; K. Li et al., 2014);

$$P_o = \Delta T \alpha I - r I^2 \quad (3.2)$$

where $r = nRi$ represents the total internal resistance of the TEG module.

Taking the derivative of P_o with respect to current I yield

$$\frac{dP_o}{dI} = \alpha \Delta T - 2rI \quad (3.3)$$

For peak current condition, the derivative obtained above is equated to zero

$$(\alpha\Delta T - 2rI = 0),$$

Hence peak current, I_p becomes;

$$I_p = \frac{\alpha\Delta T}{2r} \quad (3.4)$$

Further, I and P_o can, respectively, be expressed as;

$$I = \frac{V}{R} = \frac{\alpha\Delta T}{r + R_L} \quad (3.5)$$

Then the power output becomes;

$$P_o = I^2 R_L = \left(\frac{\alpha\Delta T}{r + R_L} \right)^2 R_L \quad (3.6)$$

Therefore, the electrical current flowing in the circuit and across the load R_L as the load current is equal to;

$$I_L = \frac{\alpha\Delta T}{r_i + R_L} \quad (3.7)$$

And can also be expressed as;

$$I_L = (V_{oc} - r_i I_L) / R_L \quad (3.8)$$

Therefore, load voltage, V_L can also be expressed as;

$$V_L = V_{oc} - I_L r_i \quad (3.9)$$

3.3.2.3 The Thermal Model of a TEG

The thermal model of the TEG pellet is developed based on Figure 3.19 and with the understanding that the heat from the heat generator encounters some thermal resistance and the current generated by the TEG also encounters some electrical resistance as it flows through the Thermoelectric Material (TEM), thus creating the Joule heat $I^2 r$ in the

elements (Kanimba & Tian, 2016; K. Li et al., 2014). During its operation, the efficiency of a TEG device mainly depends upon the ΔT or heat applied and the figure of merit Zt (Lv et al., 2020). In Figure 3.19, the temperature gradient, ΔT is equal to $T_h - T_c$ and the Seebeck coefficient α , shall be equal to $\alpha_p - \alpha_n$ which is the sum of

the Seebeck coefficients of the P and N because they are thermally parallel. The heat applied at the hot side of the TEG is Q_h and the heat dissipated on the cold side is Q_c . Therefore, the heat absorbed by the TEG is given as (Dousti et al., 2015; Karami & Moubayed, 2014);

$$Q_h - Q_c = Q_d \quad (3.10)$$

Considering a module of n pellets, the thermal power at the hot side can be expressed as (Dousti et al., 2015; Karami & Moubayed, 2014);

$$Q_h = \left(\frac{T_h - T_c}{R_{et}} \right) + T_h n \alpha I - \frac{1}{2} I^2 R_i \quad (3.11)$$

Where R_{et} is the thermal resistance of the P and N elements, I the electric current flowing in the $n\alpha$ TEG and, are the combined Seebeck coefficients of the P and N elements of the TEG.

Similarly, the thermal power reaching the cold side of the TEG is expressed as (Dousti et al., 2015; Karami & Moubayed, 2014);

$$Q_c = \left(\frac{T_h - T_c}{R_{et}} \right) + n \alpha I T_c + \frac{1}{2} I^2 R_i \quad (3.12)$$

From Equations (3.11) and (3.12), the difference in the value Q_d between the hot and the cold side of the TEG is converted to electricity according to the Seebeck phenomenon.

Electrical power, P_o of the TEG is hence equal to the thermal power, Q_d and the efficiency of the TEG can be expressed in both electrical and thermal terms as;

$$\eta_c = \frac{\text{output power}}{\text{input power}} = \frac{P_o}{Q_h} \quad (3.13)$$

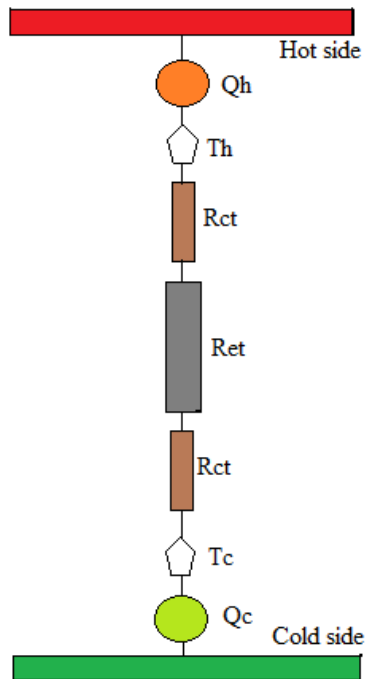


Figure 3.19: Thermoelectric Generator PN Pellet Structure

3.3.2.4 Model Development and Simulation

The TEG numerical model is developed using the internal parameters of the TEG pellet obtained from the TEG manufacturers. The parameters values are used in the MATLAB Simulink block-sets and built to make the TEG pellet by interconnecting the block-sets using numerical function operators.

Display points are used to closely monitor the individual operation outputs and finally the results are obtained from a five-channel virtual oscilloscope that outputs the values in graphical format. For clear visibility of the graticule traces, gains have been used where necessary. The scope output traces consist of the voltage, current, power, efficiency and the TEG hot side temperature, T_h . The control parameters used are the hot side and cold side temperatures of the TEG, T_h and T_c , respectively. Figure 3.20 shows the TEG model simulation flowchart while Figure 3.21 shows the actual numerical

operators and a schematic block set of the TEG model used in the MATLAB Simulink simulation platform.

The TEG boundary conditions are obtained from the length-wise dimensions of the TEG pellet

L being the length of pellet P-N

The temperature boundary conditions for heat conduction in the pellet are;

$$(1) \quad T_{P,N}(0) = T_{hot} \quad (3.14)$$

$$(2) \quad T_{P,N}(L) = T_{cold} \quad (3.15)$$

These temperature boundaries were imposed by making sure that the simulation lower side temperature setting was 30.82°C that was ramped linearly to higher side temperature of 69.2°C

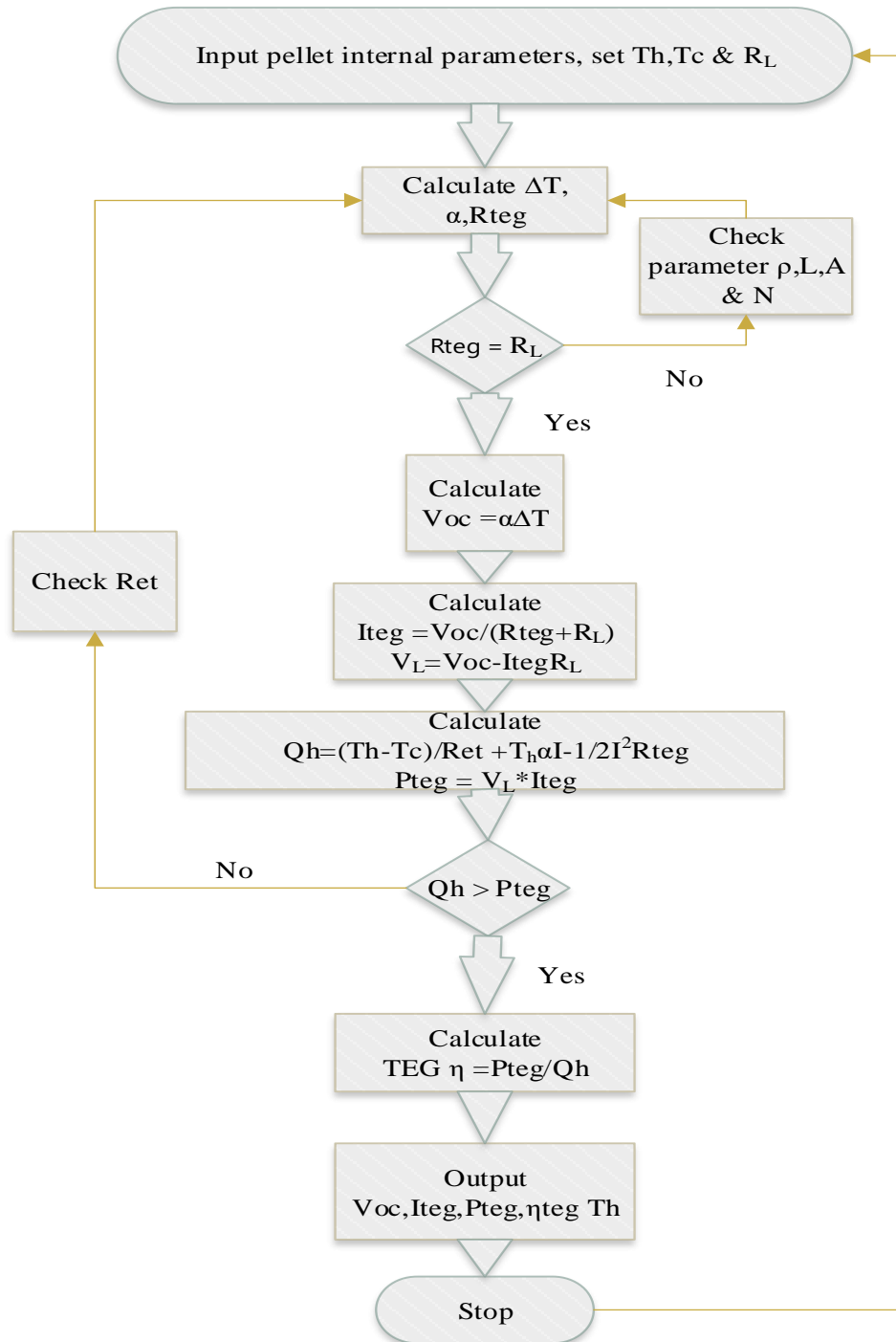


Figure 3.20: TEG Simulation State Flowchart

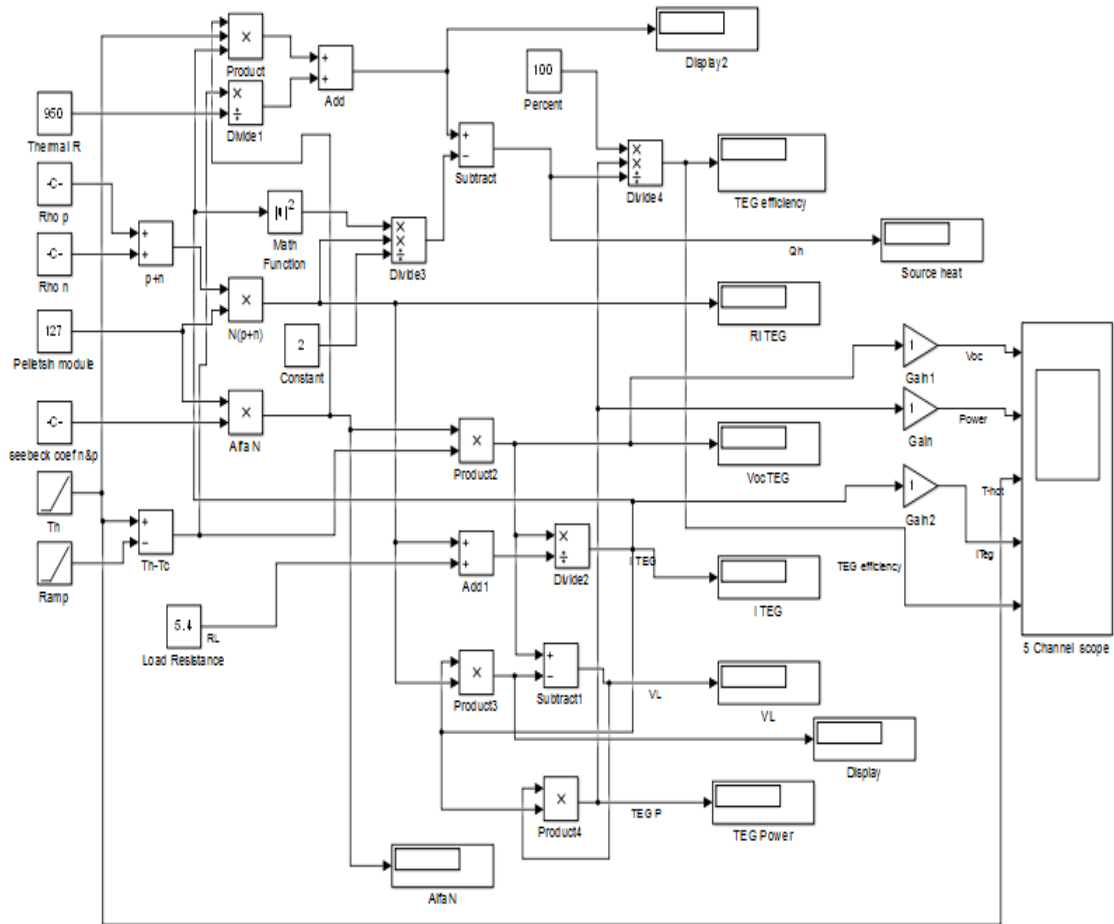


Figure 3.21: Schematic TEG Block-Set Model in MATLAB Simulink

3.3.2.5 Model Development Assumptions

During the development of the TEG model, some assumptions were made as explained. The temperature at the back plate of the PV module is taken to be the same as the temperature of the hot side of the TEG implying a near perfect thermal conducting layer between the two surfaces and no temperature mismatch on the TEG surfaces. The internal resistance of the TEG remains constant during the power generation and that the T_h temperature of all the pellets is uniform. It is also assumed that the PV cell temperature at the PVF back-sheet is uniform and starts from a low value of the site ambient and rises steadily to the maximum field value of 69.2 °C. The thermal

resistances, R_{ct} of the pellets are assumed to be insignificant compared to Q_{ct} in the electric model of the TEG.

The model has been validated using previous work done by Nabil K. et al. The two TEG pellets used differed in their internal parameters; Seebeck coefficients, electrical resistivity, length and thermal resistance that mostly affect the magnitude of their electrical outputs. The peak temperature used in the model was equivalent to the highest temperature achieved on site during field data collection so it was very different from the one used by Karami and his counterparts. Also, the accurate matching of the internal resistance and the load are factors that must have contributed to make the magnitudes vary because they affect the efficiency of the TEG.

3.3.3 TEG Bench Setup Fabrication

This setup was fabricated to study the TEG Voltage, Current and Power outputs under series and parallel connections and how their interconnection would affect their total output. The setup was not validating the simulated single TEG. The TEG experimental bench test apparatus was fabricated and set up to carry out measurements of voltage, current and power output from the physical TEG modules under laboratory thermal generated conditions. The workbench laboratory setups are fabricated for a single, two and four TEG modules. The heat dissipated by the PV is modelled using an electric heater plate and water cooling achieved using an Alucore honey comb cooling panel initially filled with cold water at 20 °C. Temperatures are measured using K-type thermocouples.

Figure 3.22 shows a schematic representation of the electrical connection of a single TEG and position of the thermocouples, while Figures 3.23(a), 3.23(b) and 3.23(c) show the single, two and four TEG setups, respectively. Their respective electrical connections are schematically presented in Figure 3.24. For each of the setups, the load resistance was matched to the TEG internal resistance as shown. The load current drawn from the TEG modules was measured as a voltage across a 1-ohm resistor. The data

from these setups are logged using a KEYENCE NR-500 logger at time intervals of 5/10 seconds or a frequency of 2 Hz and then and then collected in CSV format using a laptop computer for onward analysis.

The computer used for capturing the data was had a processor of Intel® Core i5 -4210U CPU @ 1.70GHz -2.4GHz, Installed RAM of 8GB and System type -64-bit OS, x64-based processor.

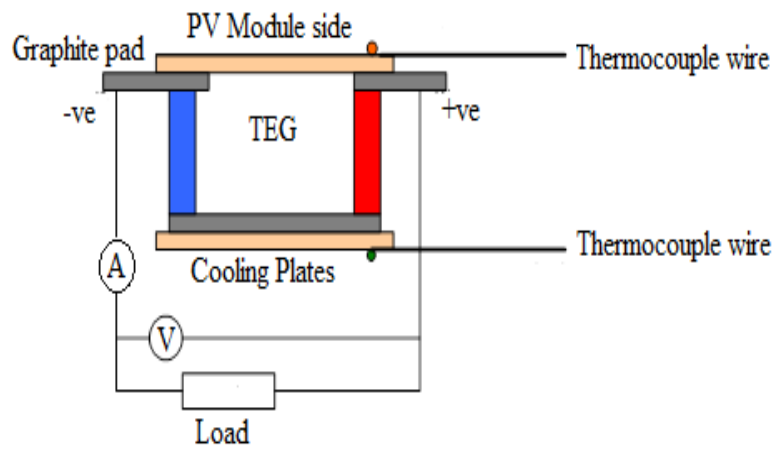


Figure 3.22: TEG Electrical Connection Schematic

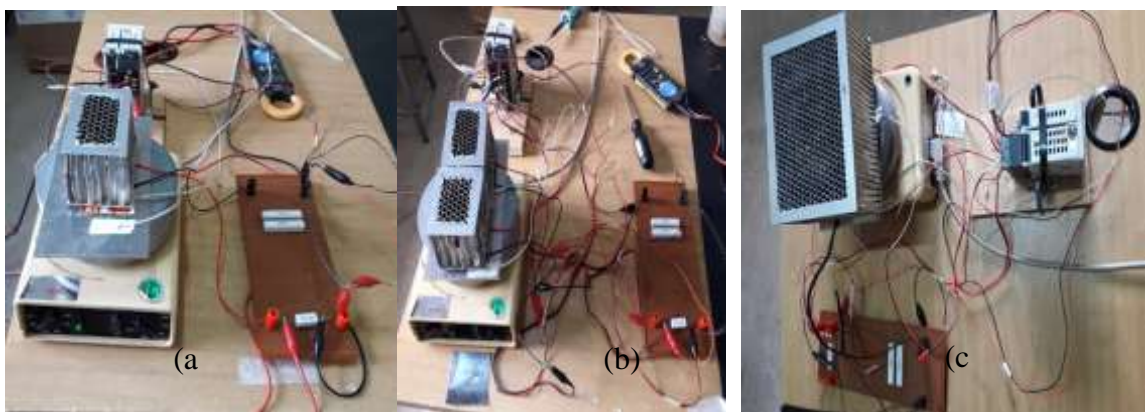


Figure 3.23: Laboratory TEG setups; (a) single, (b) two and (c) four TEGs

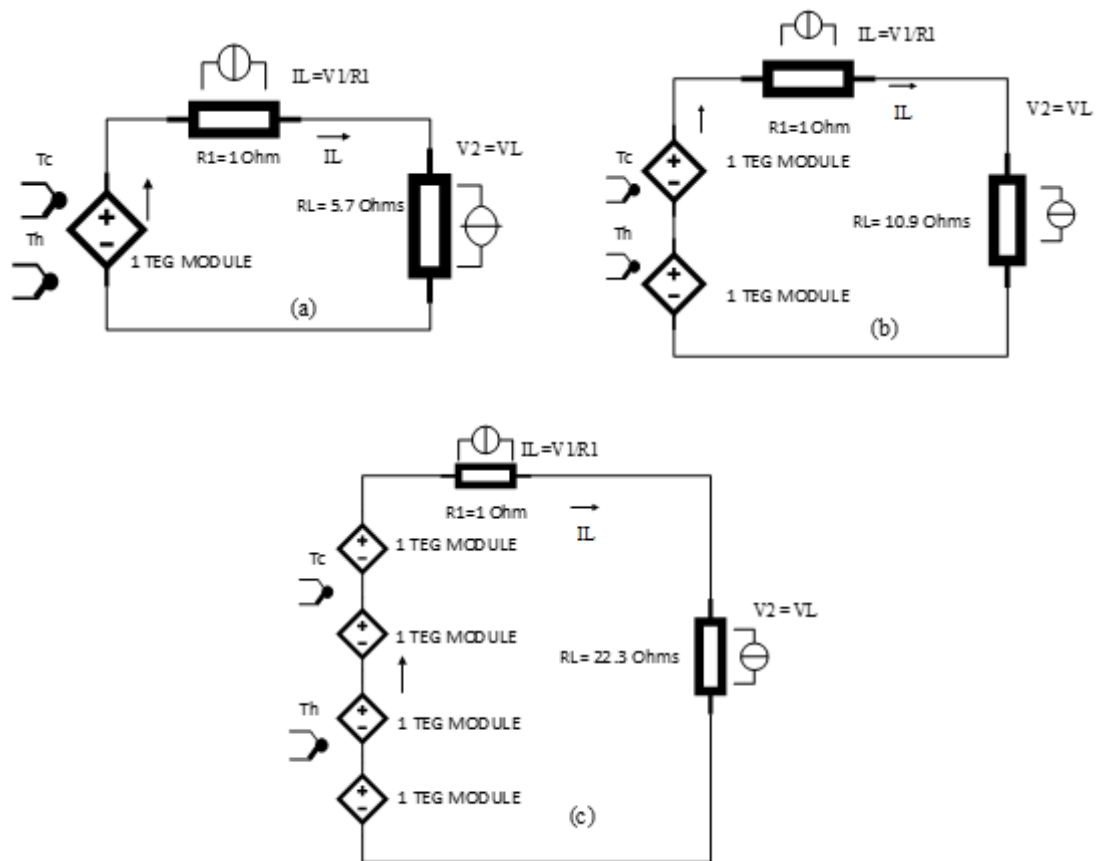


Figure 3.24: Schematic representation of the electrical connection of the TEG Modules: a) One, b) Two, and c) Four TEG Modules

In all the setups, the TEG internal resistance is matched to a pure resistive load and the only variable parameter was T_h whose values are extracted from the RAS site data at

Nyalenda, Kisumu and varied from 22 °C to 69.2 °C. A thermal pad graphite sheet with a thermal conductivity of 35.0 W/m.K is used to improve the temperature distribution between the modules (K. Li et al., 2014).

3.3.4 Field PV-TEG Power System Design

The PV-TEG system is intended to supply power to an autonomous Recirculating Aquaculture System in Nyalenda Kisumu. Using the weather data collected at the site

over a one-year period, and backed by similar data from the Kenya solar potential database (H. Gichungi, 2012), the design is prepared to suit the daily load demand allowing three Days of Autonomy (DOA) considering the site location and annual weather pattern. The main power to the RAS load demand is supplied by the PV system with storage while the TEG complements the PV power. The load for the RAS consists of a Membrane Bio Reactor (MBR), the ponds and water pumping system as presented in Table 3.4.

Table 3.4: The RAS electrical load

S/N	Load Description	Qty	Power (W)	Duty (Hr)	Energy (Wh)
1	MBR Pump	1	900	1	900
2	Filtrate pump	1	130	4.8	624
3	Blowers tank 1	1	215	2.5	537.5
4	Blowers tank 2	1	215	2.5	537.5
5	Sludge pump	1	40	1.5	60
6	Circulation pump	1	40	2	80
7	Sterilization	1	47	1	47
8	Ox guard control	8	20	24	3840
9	Bio filter pump	1	900	4	3600
10	Circulation pump	1	670	2	1340
11	UV-C generator	1	40	24	960
12	Filter pumps	1	1900	2.5	4750
13	H. tank pump	1	670	4	2680
14	RAS 1 blower	4	215	2	1720
15	RAS 2 blower	3	215	2	1290
16	Oxygen probes	1	20	24	480
17	Bio gas pump	1	450	3	1350
18	Computers	1	200	10	2000
19	Ox guard units	11	100	24	26400
20	Battery chargers	7	40	24	6720
21	24 V power unit	1	100	24	2400
	Total Load (Wh)				63216
	kWh				63.22

3.3.4.1 PV-TEG System Sizing Methodology

To get a complete and clear picture of the significance of the PV-TEG power generation system, the actual hybrid system is designed and sized factoring the demand and local

conditions of the study site. The PV system is sized based on the average annual Direct Nominal Irradiation (DNI) data obtained from the Nyalenda Kisumu site whose daily average is 6.02 kWh/m²/day and backed by the calculated 21-year daily average as 4.8 kWh/m²/day (H. Gichungi, 2012). The design parameters for the preferred items include; PV module type (polycrystalline) and size (275 W), battery storage type (L-ion) and size (48 V/50 Ah), system voltage (48 VDC), inverter type (pure sine-wave), charge controllers (MPPT), the load profile and prioritization as presented in Table 3.4. The efficiencies of all the devices used are also taken into consideration and used in the design.

The PV system output power is calculated as;

$$PV = \frac{\text{daily load}}{\eta_I \times \eta_C \times \eta_B \times \eta_{PV} \times PSH} \quad (3.16)$$

where, η_I , η_C , η_B and η_{PV} are efficiencies of the inverter, charge controller, batteries and the PV modules, respectively, and PSH is Peak-sun hours for the site. The physical dimensions of the selected TEG and the surface area of the back plate of each PV module are used in the scheme design and sizing. The interfacing device between the TEG system and the battery bank, or the charge controller's resistance (impedance) is harmonized to the internal resistance of the TEG system.

The TEG power system is designed and sized considering mainly the field TEG hot side temperature, Th and the internal resistance of the entire TEG system. Table A8 presents the basic technical specifications for the selected TEG module in the design and sizing process.

Using the manufacturer's dimensions for the PV and TEG, the area of each PV back plate being 1.395 m² and that of each TEG module being 1.6×10^{-3} m² and taking into

account a dead and edge space allowance of 30%, the back plate of each 275 Wp module would comfortably accommodate 600 TEGs.

3.4 Evaluation of Thermal Interface Materials in Mediating PV Cell Temperature Mismatch in PV-TEG Power Generation Systems

3.4.1 Introduction

This section of chapter 3 has been dedicated to studying the PV cell temperature distribution at the module PVF back sheet in a view to minimize any non-uniformity that may arise and affect the performance of the TEG in PV-TEG systems. The PV cell temperature has been analytically evaluated and also measured in an open setup environment to determine temperature distribution on the PV-PVF back sheet. Further, the effects of cell temperatures distribution have been investigated using three thermal interface materials (TIM) under air and water-cooling environments with aluminum honeycomb cooling panels as the cooling contact medium.

3.4.2 PV-TEG System Model and Governing equations

A PV module can be integrated with TEG modules using a TIM that takes care of the roughness of the surfaces and the Thermal Coupling Resistance (SCR) so that the two technologies can concurrently be used to generate electricity (J. Zhang et al., 2020b; Zhou et al., 2017)[88]. The combined technologies can be expressed schematically as in Figure 3.25 where the PV and TEG are interconnected using a common thermal connector. In Figure 3.25, the heat on the PV cell is then absorbed by the TEG array mounted under the cells to generate electricity following the Seebeck phenomenon (Fisac et al., 2014; Lashin et al., 2019). Hence the TIM or thermal connector between the PV cell and the TEG modules plays a significant role in the performance of the TEG module electricity generation process as it takes care of uniform heat transfer between the microscopic rough surfaces of the PV and the TEG (Y. Chen & Xuan, 2015).

where, α_{PN} are the Seebeck coefficients of the P and N semiconductor materials of the thermoelectric modules that are thermally in parallel.

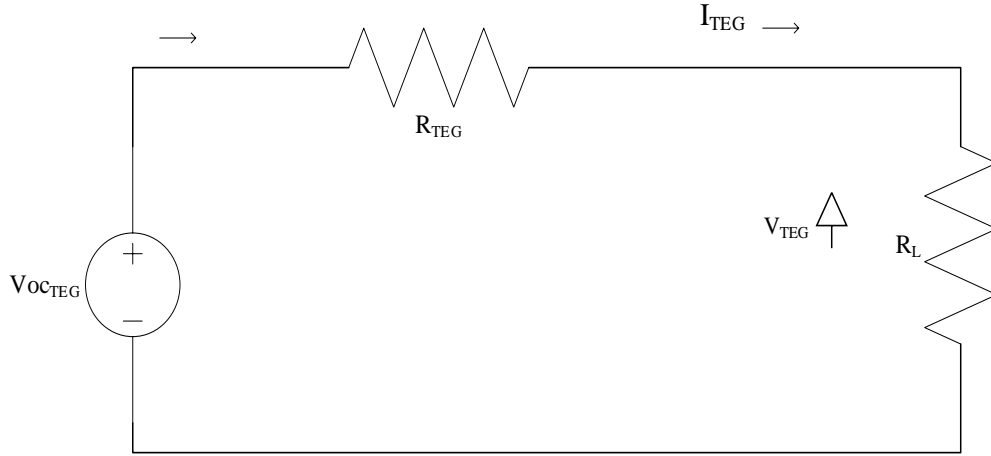


Figure 3.26: A schematic of equivalent TEG Cell

The power generated by the TEG, P_{TEG} is given as in Equation (3.18), (Paraskevas & Koutroulis, 2016);

$$P_{TEG} = \frac{(\alpha_{PN}\Delta T)^2}{(R_{TEG} + R_L)^2} R_L \quad (3.18)$$

Maximum power is obtained from the TEG when the internal resistance, R_{TEG} and the load impedance, R_L are matched and occurs at a point where V_{TEG} is equal to $\frac{V_{OC}}{2}$ and I_{TEG}

is equal to $\frac{I_{SC}}{2}$. When the resistances R_L and R_{TEG} are matched, maximum TEG power is

achieved and is expressed as in Equation (3.19), (Paraskevas & Koutroulis, 2016);

$$P_{TEGMax} = \frac{\alpha_{PN}^2 \Delta T^2}{4R_{TEG}} \quad (3.19)$$

Equation (3.19), shows that the temperature gradient and hence the hot side temperature of the TEG, T_h , is key for good performance of the TEG. When the T_h of the TEG modules is not uniform or near uniform, the TEGs under the PV module operate at different Maximum Power Points (MPPs) and so their generated maximum power is different even when the R_{TEG} and R_L are matched. To counter the effect of temperature mismatch, studies have been carried out by several researchers where methods of matching the Maximum Power Points (MPP) of TEGs using electronic approaches have been developed and proposed (Dalala, 2016; H. Nagayoshi & T. Kajikawa, 2006; Montecucco et al., 2014; Paraskevas & Koutroulis, 2016).

The main factors that influence PV cell temperature are the incident solar irradiance, ambient temperature, wind speed and the cell manufacturer's specifications on the nominal cell operating temperature (NOCT). So the simplest linear expression that gives explicit correlation for the evaluation of PV temperature is where the module cell temperature T_{mod} is expressed as in Equation (3.20), by (Maturi et al., 2014).

$$T_{mod} = T_a + KG \quad (3.20)$$

The expression links T_{mod} with the ambient temperature and the incident solar irradiance G , where K is the Ross coefficient of the module. Further, the cell temperature can be expressed as in Equation (3.21), by (Jakhrani A.Q et al., 2011);

$$T_c = T_a + KG_T \quad (3.21)$$

where;

$$K = \Delta \frac{(T_c - T_a)}{\Delta G_T} \quad (3.22)$$

This was further improved by Rauschenbush (1980) to take into account the effects of wind speed, heat loss coefficient and the cell nominal operating temperature, as expressed by in Equation (3.23), by (Jakhrani A.Q et al., 2011).

$$T_c = T_a + \frac{G_T}{G_{TNOCT}} (T_{cNOCT} - T_{aNOCT}) \left(1 - \frac{\eta_m}{\tau_\alpha}\right) \quad (3.23)$$

And later, Duffie and Beckman expressed the cell temperature as in Equation (3.24), by (Duffie & Beckman, 2013);

$$T_c = T_a + \frac{G_T}{G_{NOCT}} \left(\frac{9}{5.7 + 3.8V_m}\right) (T_{cNOCT} - T_{aNOCT}) (1 - \eta_m) \quad (3.24)$$

They later optimized it to Equation (3.25), (Duffie & Beckman, 2013);

$$T_c = T_a + \left[\left(\frac{G}{G_{NOCT}}\right) \left(\frac{9.5}{5.7 + 3.8V_w}\right) (T_{cNOCT} - T_{aNOCT}) \left(1 - \frac{\eta_c}{(\tau_\alpha)}\right) \right] \quad (3.25)$$

3.4.3 Simulation and Experimental Procedures

This sub-section comprises of analytical model development, simulations and fabrication of cell mapping techniques and temperature measurements setups. In the analytical model formulation, a model is used to analytically evaluate the PV cell temperature while in the experimental part, different setups are fabricated using various Thermal Interface Materials (TIMs) for temperature distribution and PV-TEG performance measurements.

3.4.3.1 Analytic PV Cell Model Description

An individual PV cell on a module is taken as a representative of the many cells on the module. A module could have 18 cells, 36 cells, 60 cells and even more and so, one of them can represent the rest on the module. The representative cell on a module is always expected to give the features and temperature of the rest of the cells because they are identical and mounted on the same module. In this description, the cell analytical analysis provides the representative cell temperature and attempts to disclose how well the single cell temperature may represent the other cells when the actual cell temperatures are measured in the setups that follow.

Previous researchers developed PV system models that have been used to predict cell temperature in different analytic and simulation platforms. The models have been mathematically explicit or implicit to suit the researcher's preferences and have also been classified in steady-state or transient approaches, where the parameters in the models are assumed to be either independent or dependent of time, respectively (Jakhrani A.Q et al., 2011). These models have been applied in many varying environments and PV mounting conditions and results of different accuracies obtained depending on the model used. Some selected models are listed in Table 3.5 for assessment (Jakhrani A.Q et al., 2011).

Among them, the optimised Duffie and Beckman model has been applied for this study because it takes into account the cell temperature at varying wind speeds (Duffie & Beckman, 2013). The model also offers better accuracy in predicting the cell temperature and has also been preferred before by other researchers for size optimisation, analysis, simulation and design of PV systems (Jakhrani A.Q et al., 2011). The Duffie and Beckman model has been used widely in designs and when compared to other models by Renata et al (2019), the model presented the lowest average error at 5.20% (Yang et al., 2019). In this study, the analytical model analysis is performed in Microsoft excel, where input parameters such as; ambient temperature, wind speed and

the irradiance were obtained from measured matrix temperatures taken during the preliminary setups. This was done to help in the validation of the results.

Table 3.5: Illustration of Models for Determination of PV Cell Temperature (Jakhrani A.Q et al., 2011)

S/n	Author(s)	Empirical models	Comments
1	Didier (2001)	$T_c = T_a + \frac{(T_{cNOCT}-20)}{800} (219 + 832 \frac{S}{Kt})$ $Cf = 1-1.17 \times 10^{-4} (S_m - S)^2$	<p>For non-optimal values, use a multiplier with</p> <p>S_m denotes optimal tilt angle and S is the actual tilt angle (degrees)</p>
2	Krauter (2004)	$T_c = T_a + KG_T$, and $K = 0.0058, 0.012$ and 0.03	The value of k for lower, upper and usual modules
3	Mondol <i>et al.</i> , (2005 and 2007)	$T_c = T_a + 0.031G_T$, and $T_c + 0.031G_T - 0.058$	T_c is taken as mean of front and back temp. of module °C, $V_w > 1m/s$ with constant U_L
4	Duffie and Beckman (2006)	$T_c = T_a + \left[\left(\frac{G}{G_{NOCT}} \right) \left(\frac{U_{LNOCT}}{U_L} \right) (T_{cNOCT} - T_{aNOCT}) \right] \left(1 - \frac{n_c}{\tau \alpha} \right)$	<p>The n_c value of transmittance and absorbance product ($\tau\alpha$) was taken as 0.9</p> <p>Coefficient of heat losses (U_L) was associated</p>
5	Chenni <i>et al.</i> , (2007)	$T_c = 0.943T_a + 0.028G_T - 1.528V_w + 4.3$	Coefficient of heat losses (U_L) was not taken into account

3.4.4 PV Module Preliminary Cell Mapping and Temperature Measurement Setup

A 13 Watts peak (Wp) polycrystalline PV module of 36 cells and nominal voltage of 12 V was used to carry out the cell mapping and subsequent cell temperature measurements process. The objective of the cell mapping procedure was to categorise and investigate possible individual cell temperature differences within the PV module when subjected to uniform solar radiation levels. The cell mapping and marking was realized by first identifying the central cells on the module, marked as matrix 1 and then from there radiating outwards to each cell position with respect to the centre as shown in Figure 3.27. The next nearest matrices outwards are denoted as matrix 2 followed by other sets of matrices 3, 4 and 5 up to the outermost cells on the module designated as matrix 6.

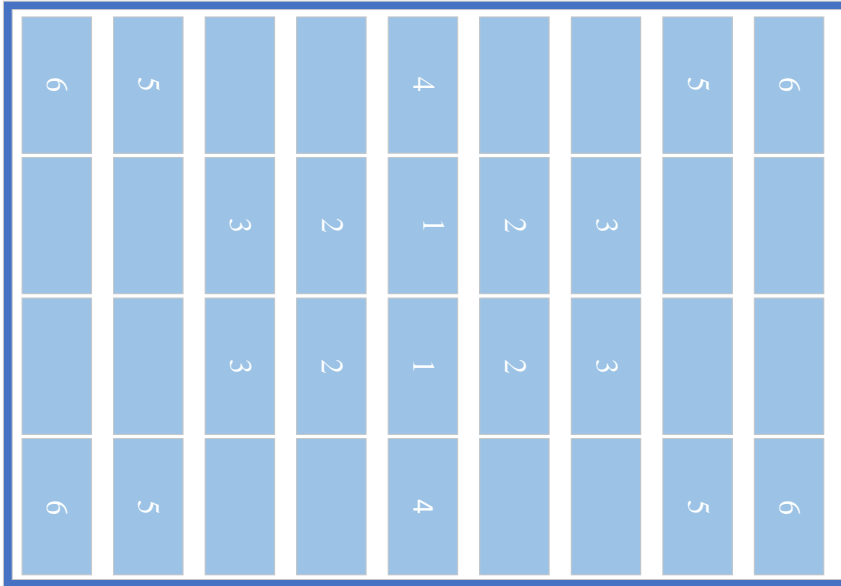


Figure 3.27: Cell mapping on the 36 Cell 13 Wp PV Module

In the cell mapping procedure, the cells in the same matrix are almost at the same distance from the centre-most cells and are assumed to be at the same temperature. One cell from each matrix designation cluster is randomly selected for actual measurements. Figure 3.28 (a) shows the front side of the cell matrix mapping. The temperature thermocouples (K-type) used to measure the individual cell temperatures are stuck on the Polyvinyl Fluoride (PVF) layer at the back side of the PV cells using industrial heat resistant tape as in Figure 3.28 (b). The thermocouples are then covered with another industrial adhesive to firmly bind them to the PVF back plate whose thermal conductivity (k) is 0.25 W/mK as per the manufacturer’s specifications. This preliminary setup is fabricated to enable measurement of the individual bare cell temperatures before subsequent fabrication of systematic measurement setups. The module was then mounted horizontally on a wooden structure, 1 meter above the ground where there was free circulation of air around and during the measurements, the wind speed was fairly low ranging between 0 and 0.3 meters per second. The setup was then subjected to solar radiation and the data logging done using a KEYENCE NR500 data logger. Temperature measurements from the 6 representative cells selected from the designated matrices are taken over a period of 125 minutes at intervals of 30 seconds and the logged data

thereafter transferred to a computer in Comma Separated Version (CSV) file format for analysis.

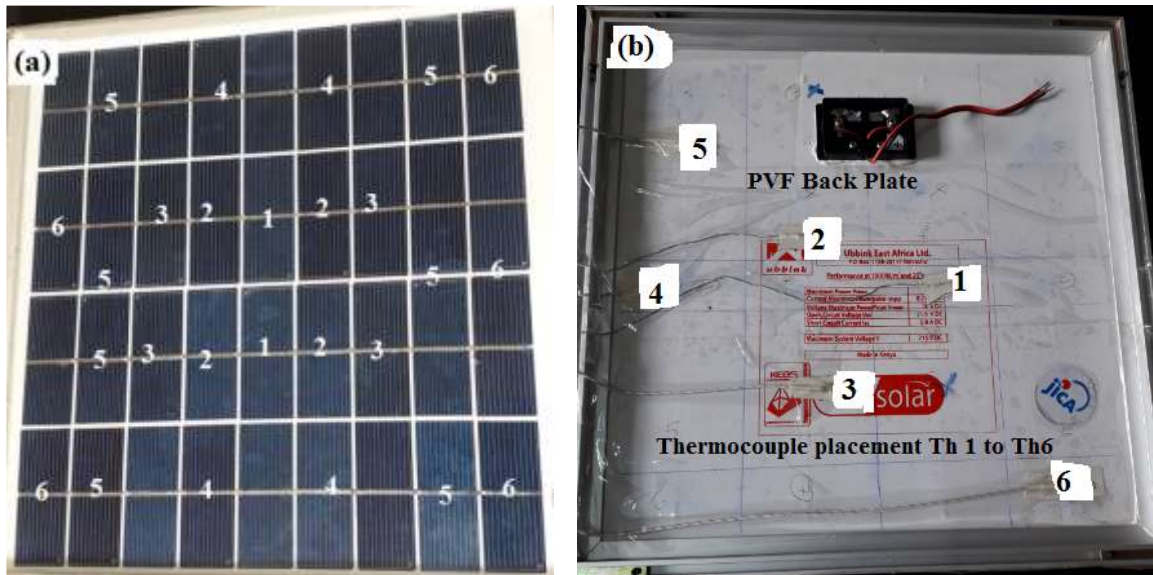


Figure 3.28: Cell mapping and temperature distribution measurements; (a) PV cell mapping, (b) Thermocouple placement

3.4.5 Systematic Solar PV Cell Temperature Measurements Setups under TIMs

After the preliminary cell mapping and bare cell temperature measurements setup, the eight center most cells of the 36 cells PV module are designated for systematic cell temperature measurements for further investigation. The eight cells are all drawn from the three central matrices mapped earlier and designated as Matrix 1, Matrix 2 and Matrix 3. Once again, a representative cell is randomly chosen for placement of the temperature measurement thermocouples. Three K-type thermocouples were stuck on the TIMs under the PVF back plate as shown in Figures 3.29 (a), (b) and (c). The three thermocouples are designated as T_h 1, T_h 2 and T_h 3 and used to collect the cell temperature data when the module is exposed to solar radiation as in Figure 3.29 (d). Three module setups were fabricated using graphite sheet TFO-S250-CB of 0.27 mm gauge thickness and a thermal conductivity (k) of 35 W/mK, PH-3 heat spreader (HS)

sheet with thermal conductivity (k) of 400 W/mK and gauge thickness of 0.30 mm and clean aluminum foil sheet of 0.32 mm gauge thickness and thermal conductivity (k) of 235 W/mK as in Figure 3.29 (a), (b) and (c) respectively. This setup is fabricated to observe the effects of TIMs on cell temperature distribution on the three matrices, measured as T_h 1, T_h 2 and T_h 3 and also to form a basis for the subsequent measurements.

During the data analysis, the variance in temperature is evaluated as a percentage difference between the mean of the measured cell matrix temperatures and the individual cell matrix temperatures in each case.



Figure 3.29: Systematic temperature distribution measurements using various TIMs; (a) Graphite (b) Heat spreader (c) Aluminum foil (d) Complete setup of the three sets.

3.4.6 PV-TEG Temperature and Voltage Measurements under TIMs

In this subsection, four setups were fabricated where the four central cells of the PV module are designated for the measurement procedures. The three PV-TIM-TEG setups and a control (PV-TEG) were investigated under air- and water-cooled environments. Having looked at the effects of TIMs on the temperature distribution, this particular

investigation was meant to bring out their actual significance on the PV-TEG power generation assembly. In studying the effects of temperature mismatch on TEG voltage output, two thermocouples and two TEGs were used to measure cell temperature and voltage output, respectively in each setup. These measurements were referenced to the center-most Matrices 1 and 2 of the initial cell mapping and shown in Figure 3.27. The temperature and voltage measurements were first conducted under passive air and later under passive water cooling where a honey comb aluminium cooling panel is used as the heat sink. The cells on Matrix 1 and 2, are selected after confirmatory results from the previous measurements revealed uneven temperature distribution on the entire module. The three setups are fabricated using three different TIMs sandwiched between the PV modules' PVF back plate and the TEG hot side and then thermocouples stuck on the TIMs at the edge of each TEG module space to measure the PV cells temperature as shown in Figure 3.30 (a), (b) and (c) for the three TIMs, respectively. The fourth module used as the reference had its thermocouples stuck on the PVF cell matrix leaving space where the TEGs were to rest as in Figure 3.30 (d). Before the thermal interface materials were applied on the PV back sheet, the PVF was well cleaned using a solvent cleaner fluid to remove all particles and any oily dust on the surface. The TIMs were then each laid flat on the PVF avoiding any air being trapped in between. An industrial adhesive was then used to firmly hold the TIM on the PVF. The TEG modules were stuck on the honeycomb cooling panel from their cold side Figure 3.30 (e), so that they rest square on the TIMs and PVF where the complete assemblies were mechanically clamped together at same safe mechanical loading of 4.8 kPa that is within the safe standard loading of 5.4 kPa for PV cells as shown in Figure 3.30 (f). The four setup assemblies were then mounted outdoors horizontal to the earth surface facing north at the same inclination as in Figure 3.30 (f) and exposed to solar irradiation. During this setup, the primary aspects under study were the temperature distribution across each module, notably mismatch under the PV cells and how the mismatch affected the voltage generated by the TEG modules below the PV cells.

Measurements on the four PV-TEG-TIM setups were conducted under cold water cooling as shown in Figure 3.31. Water cooling was used to study its significance on temperature distribution and TEG voltage patterns because water has a higher heat capacity, density, thermal conductivity and would be preferred when available especially where water is easily accessible (Yin et al., 2017). The water cooling setup was fabricated in open vessels where water was refilled to spilling level at regular intervals of 10 minutes and 2minutes refill to maintain the water temperature at a near constant cooling temperature as data was captured. These water-cooled setups would also inform the proposed actual design of the PV-TEG system for a Recirculation Aquaculture System (RAS) at a lakeside site in Nyalenda Kisumu, Kenya as reported previously in our study (Kidegho G.Guyo et al., 2020). The TEG voltage output and the PV cell temperatures were once again simultaneously logged using a KEYENCE NR500 data logger.

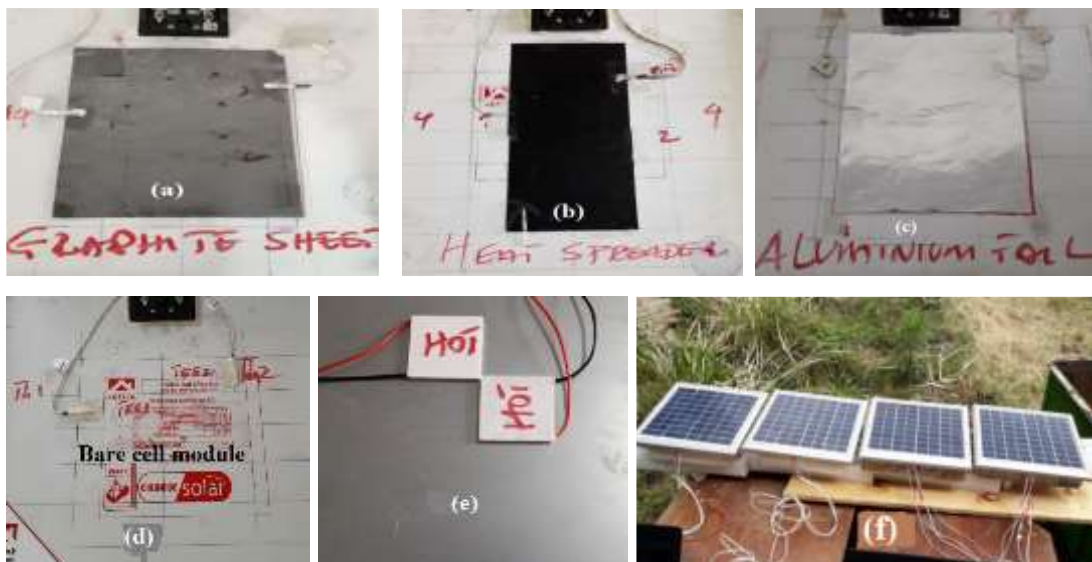


Figure 3.30: Air cooled PV-TEG setups (a) graphite (b) heat spreader (c) aluminum foil (d) bare cells (e) TEGs mounted (f) Complete setup



Figure 3.31: Water cooled PV-TEGs setups for the three TIMs and the reference case

3.5 Economic Analysis and Viability of the PV-TEG Hybrid System

3.5.1 Introduction

In this section of chapter 3, an economic analysis has been carried out on the project to determine its economic viability and also inform future prospect. Economic analysis offers the necessary information required to support decision making for future investment of government or private resources. The economic analysis was carried out from both the national and private economic point of view. This is because for a project to be economically viable, it must satisfy the economic efficiency requirements.

A four decision criteria has been used in evaluating the project economic viability and the parameters used are: - the project Net Present Value (NPV) the Payback Period (PP), Internal Rate of Return (IRR) and Profitability Index (IP) which all take into account the

time value of money and opportunity cost (Zeraatpisheh et al., 2018). The project life cycle is 25 years when most of the components shall have depreciated to a level requiring replacement for economic viability and sustenance and when the salvage value of the project is also evaluated.

3.5.2 PV-TEG System Materials and Cost Analysis

The main components used in the assembly/fabrication of the PV-TEG system are the PV modules, thermoelectric generators, charge controllers, batteries and inverter whose details and sizes are available in the system design and sizing in section 3.3.4. Other auxiliary components that facilitate the PV-TEG power generation and storage are also designed and sized. The complete system components tally and their specifications are presented in Table 3.6. Most of the components are locally available but due to quality and strict specifications adherence, all major components were obtained from abroad.

Table 3.6: Component Technical Specifications and Cost

S/N	Description	Unit	Quantity	Cost
1	275Wp solar panels AXITEC	Pcs	72	784080
2	SMA Sunny Tri-power 25000TL-30 Inverter	Pcs	1	280390
3	Charge controllers MPPT 250/100 Victron	Pcs	6	509850
4	TEG Charge Controller MPPT 100/100	Pcs	1	56100
5	Lithium-Ion Batteries BYD 48/50AH 2.5kWh	Pcs	12	2225520
6	Thermoelectric Generator (TEG) modules	Pcs	43200	2613600
7	Distribution boards and panels	Pcs	5	66000
8	Looping and splitter boxes	Pcs	20	33000
9	Mounting GI framework	Lot	1	132000
10	Alucore cooling panels 1.2m ×1.2m×6mm	Pcs	200	422400
11	GI Fasteners and adhesives	Lot	1	226017
12	Cabling and connectors	Lot	288	22000
13	Thermal sheet material (graphite/ heat spreader)	Pcs	72	1584000
14	Clamping brackets and bolts	Lot	1	187900
15	Battery cabinets as BYD	Pcs	2	55000
			Ksh.	9197857

3.5.3 System Economic Analysis

The economic analysis of the project is carried out to appraise the economic viability of the project using the assessment criteria tools like NPV, IRR, PP and PI. The NPV is calculated using Central Bank of Kenya (CBK) discounting rates for the period of May and September 2018 when the project would be procured to observe the financial behaviour of the project. The NPV is the projects total benefits minus the total costs calculated at the present value using a discount rate. The inflation rate during the year has also been incorporated to determine the NPV of the project. A nominal cash flow and nominal discount rate approach has been used as well. In this project, there are no cash flows so the NPV is evaluated using the annual avoided cost of energy resulting from the project. The cost of energy is calculated using the Small Commercial (SC) tariff of the utility (KPLC) in Appendix E that includes all the levies, adjustments and taxes incurred for supply of grid power. NPV is calculated as in Equation (3.26),

$$NPV = \sum_{t=0}^T \frac{C_t}{(1+r)^t} \quad (3.26)$$

where C is the cash flow at interest, r is the discount rate expressed as a decimal and t is the time period.

The IRR is used in the analysis mainly to compare a number of projects for investment consideration. IRR is the discounting rate that makes the NPV equal to zero. When comparing projects, the project with higher IRR is normally preferred over the one with lower IRR. IRR is evaluated as in Equation (3.27),

$$IRR = 0 = NPV = \sum_{t=0}^T \frac{C_t}{(1+IRR)^t} \quad (3.27)$$

where C is the cash flow at time t , IRR is the discounting rate/internal rate of return expressed as a decimal, t is the time period.

On the other hand, the PI is the project investment ratio used to compare the projects costs and profits. It is the ratio of the NPV and the initial investments evaluated using Equation (3.28), as;

$$\text{Profitability Index (IP)} = \frac{NPV}{\text{Initial Investment}} \quad (3.28)$$

PI of one (1) or more than one (1) shows that the project is profitable while PI of less than one (1) shows that the project is not profitable.

The project Payback Period (PP) is evaluated by dividing the total cost of investment of the project with the annual benefits over the period of the project and the result obtained is expressed as a ratio of the project life period in years and can be expressed as in Equation (3.29),

$$PP = \frac{\text{Initial Investment}}{\text{Net cash flow per period}} \quad (3.29)$$

Also

$$PP = A + \frac{B}{C} \quad (3.30)$$

where A is the last period number with a negative cumulative cash flow, B is the absolute value of cumulative net cash flow at the end of period A and C is the total cash inflow during the period following A .

CHAPTER FOUR

RESULTS AND DISCUSSIONS

4.1 Preliminary Data Collection at JKUAT –IEET for PV-TEG Hybrid System

In preparation to use the identical PV modules for measurement of the required features, the modules were first characterised by subjecting them to the same irradiance and temperature conditions to confirm the parameters against their technical specifications. Their open circuit voltages (V_{oc}) were measured under same conditions environmental conditions so as to characterise and compare them.

Figure 4.1 shows the open circuit voltage plots for the two modules plotted together with the irradiance during the measurements. V_{oc} 1 and V_{oc} 2 plots were almost identical and the differences were experimentally negligible implying that the modules could be used for comparison measurements because there were no abnormal differences observed. This exercise was carried out for all remaining PV modules used for measurement. Both the PV modules open circuit voltage responses closely followed the irradiance pattern rising and falling when the irradiance increased and dropped respectively.

The error margin for the experimental negligible measurement differences was 1% for irradiance, 0.5% for Voltage and temperature and 0.1% for current measurements. During the characterization measurements, the temperature started at 58.8 °C rising to 62.8 °C then reduced to 35.1 °C and later rose slightly to 47.5 °C at the end of the measurements. There was a negligible average open circuit voltage percentage difference of 0.012% where none of the modules was noticeably lower or higher than the other. The day was very bright with some brief light cloud casting and the average irradiance was 812.73 W/m² with a peak value of 1277 W/m² and a low value of 193.5 W/m².

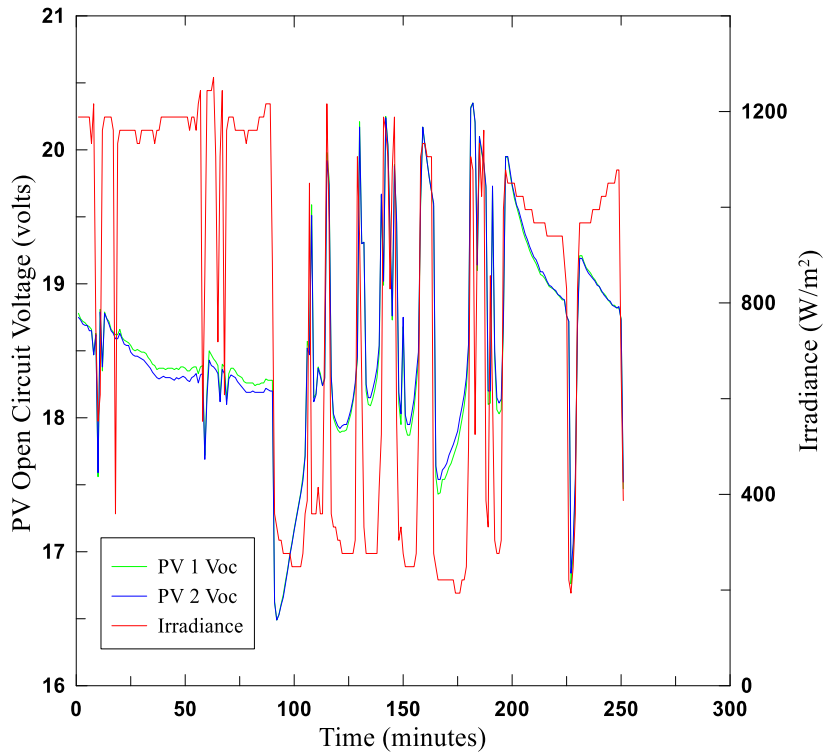


Figure 4.1: Open circuit voltage characterization

After successful characterization of the PV Modules, SS-1 for the measurement of PV cell temperature and open circuit voltages was fabricated and measurements conducted on site under natural solar irradiation. Conventional PV 1 back plate was left bare while an aluminum Alucore honey comb cooling panel was mounted behind the back plate of PV 2 to study the cell cooling process. The modules were passive air cooled and subjected to the same solar irradiation over the entire measurement period.

Figure 4.2 shows the graphical results obtained from the measurements. PV 1 achieved a peak cell temperature of 40.6 °C, average of 35.22 °C and a low value of 33.2 °C while PV 2 achieved a peak cell temperature of 35.25 °C, average of 31.24 °C and a low value of 29.95 °C. The average percentage temperature difference between the PV 1 and PV 2 module temperatures was 12.61% while the average open circuit percentage difference was 3%. The average irradiance over the measurement period was 480.24 W/m² with a

peak of 939.8 W/m^2 and a low irradiance of 276.4 W/m^2 . The temperature difference and voltage difference are quite significant especially when a large system is considered.

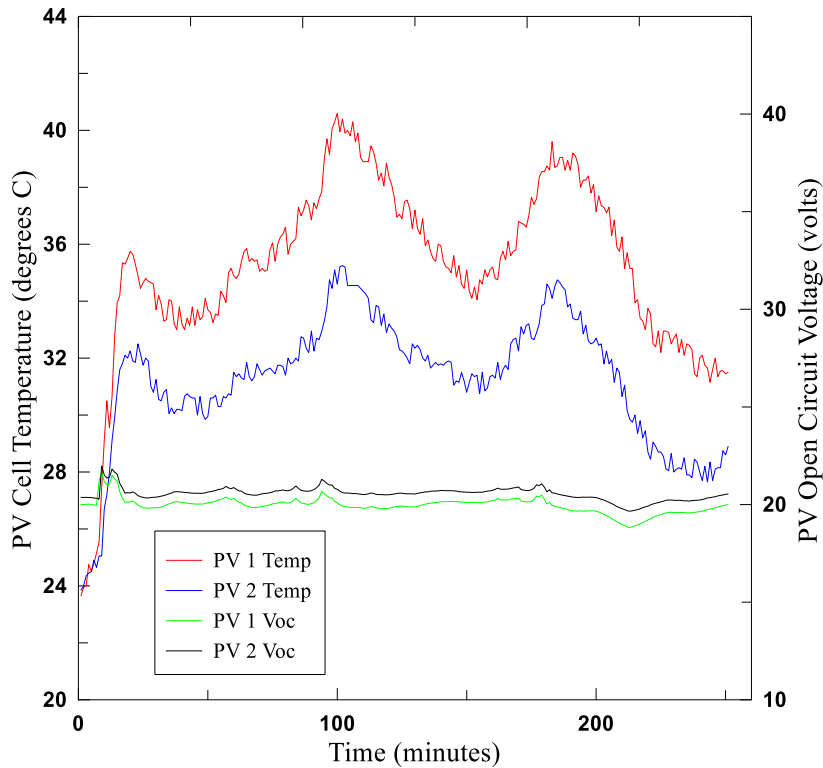


Figure 4.2: PV cell temperature and open circuit voltage both air cooled

The second specific fabrication 2, SS-2 was fabricated with one module PV 2 water cooled and the second module PV 1 is air cooled without a cooling panel mounted underneath the PV module. Both modules were subjected to the same irradiance horizontally mounted where the cooled PV 2 was floating in water on the Alucore cooling panel as in Figure 3.5. 10 TEG modules were stuck on the cooling panel on PV 2 to study their performance under water cooling.

Results presented in Figure 4.3 show that PV 1 achieved a peak cell temperature of $64.85 \text{ }^\circ\text{C}$, average of $43.06 \text{ }^\circ\text{C}$ and a low value of $36.75 \text{ }^\circ\text{C}$ while PV 2 had a peak cell

temperature of 55.55 °C, average of 38.10 °C and a low value of 31 °C. The average percentage temperature difference between PV 1 and PV 2 was 12.55% with the PV 1 temperature predominantly higher, while the average percentage output voltage difference was 3.95% with the PV 2 voltage predominantly higher. The average TEG open circuit voltage was 1.11 volts and has been plotted on the same axes with the PV open circuit voltage for comparison. During the measurements, the average irradiance was 625.71 W/m² with a peak value of 1160.9 W/m² and a low value of 221.2 W/m². The voltage output for both PV modules strictly followed the irradiance level pattern.

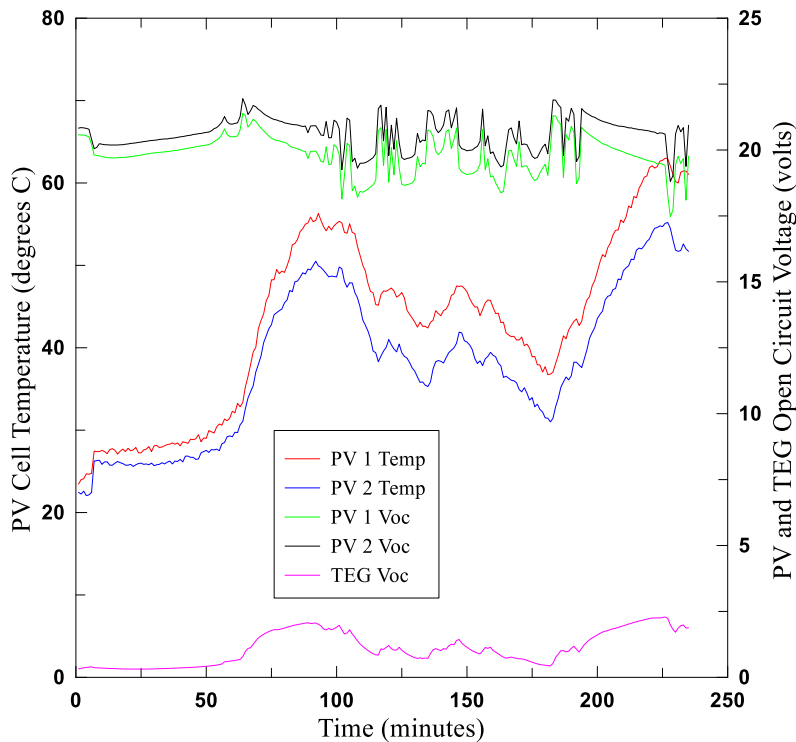


Figure 4.3: PV cell temperature and open circuit voltage air cooled and water cooled

Specific setup 3, SS 3 was fabricated with one module PV 2 water cooled and the second module PV 1 is air cooled and both PV modules had Alucore cooling panels mounted underneath them. The modules were then subjected to the same irradiance horizontally mounted where the cooled PV 2 was floating in water on the Alucore cooling panel

while PV 1 was mounted air cooled as in Figure 3.1.6. 10 TEG modules were once again stuck on the cooling panel on PV 2 to study their performance under water cooling because this would inform the PV-TEG hybrid system design.

Results graphically shown in Figure 4.4 reveal that PV 1 achieved a peak cell temperature of 64.45 °C, average of 62.25 °C and a low value of 61.05 °C while PV 2 had a peak cell temperature of 56.9 °C, average of 55.63 °C and a low value of 54.45 °C. Once again, the PV 1 cell temperature was noticeably higher than that of PV 2. The average percentage temperature difference between PV 1 and PV 2 was 11.90% with the PV 1 temperature mainly higher, while the average percentage output voltage difference was 3.76% with the PV 2 voltage once again predominantly higher. The average TEG open circuit voltage was 2.11 volts.

During the measurement period, the sky was very clear attaining average irradiance was 987.39 W/m², a peak value of 1055.4 W/m² and a low value of 884.5 W/m². The consistently high irradiance has resulted to a higher TEG output voltage as compared to the SS 2 setup. Here also, the voltage output for both PV modules strictly followed the irradiance level pattern.

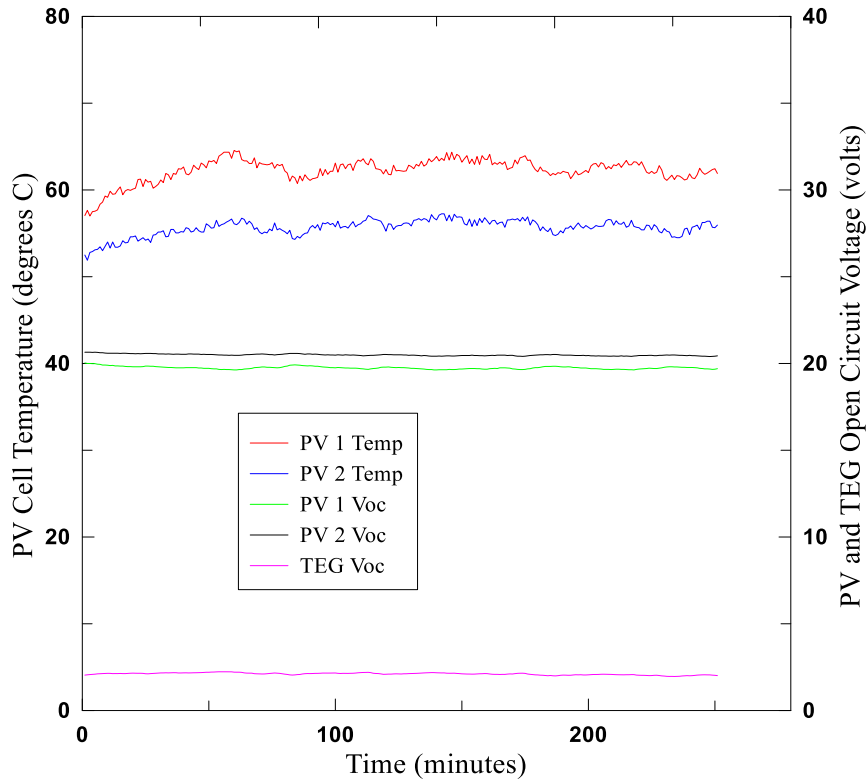


Figure 4.4: PV cell temperature and open circuit voltage air cooled and water cooled

Specific setup SS 4 was fabricated using a battery loading bank consisting of 10 compact fluorescent lamp loads and a battery charging system consisting of two charge controllers and two 10 AH, 12 VDC Lithium-ion batteries. The loading bank was used for discharging the batteries to achieve the same state of charge (SOC) for the two batteries while the charging system was for charging the battery system to study the power charging capacities of two PV systems. This setup was fabricated to study the performance of conventional PV and water-cooled PV system when charging batteries.

This pilot study would inform the design of the proposed PV-TEG power generation system for supplying power to the autonomous (RAS) at Nyalenda Kisumu. The PV cell temperature was measured using K-type thermocouples and the temperature, voltage and current data was collected using the KEYENCE NR 500 system. Figure 4.5 shows the

graphical results from the setup measurements. It was observed that PV-1 air cooled with Alucore cooling panel had a higher cell temperature than PV-2 that was Alucore water cooled. The percentage difference is 10.84% where PV-1 was predominantly higher. On the other hand, the DC power was correspondingly higher for PV-2 compared to PV-1 with a percentage difference of 14.09%.

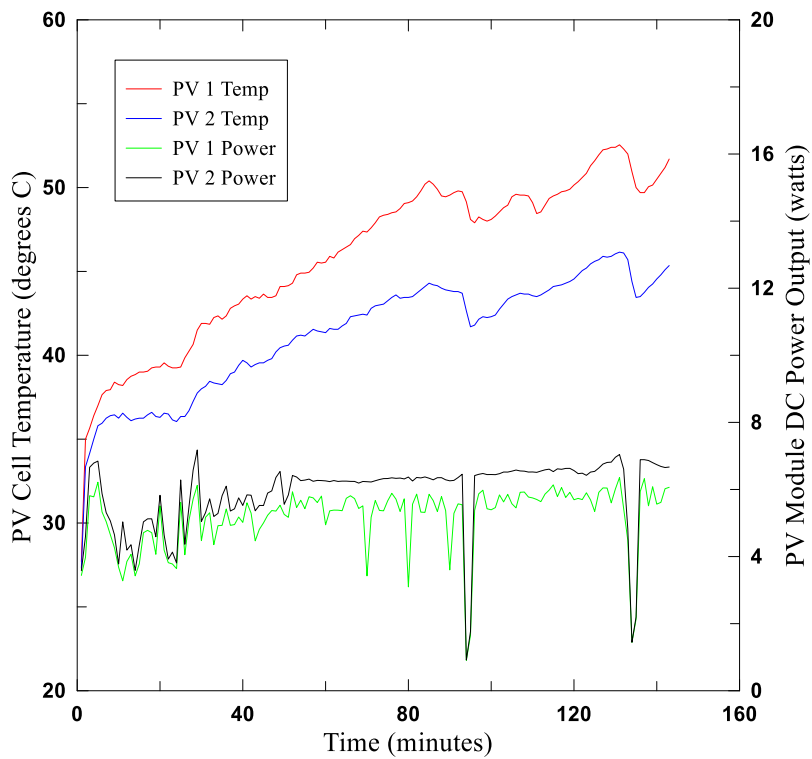


Figure 4.5: PV cell temperature and Battery Charging DC Power output

The summary of the results obtained from the setups fabricated to study the main aspects in the PV-TEG hybrid systems in this section of the chapter have been presented in Table 4.1.

Table 4.1: Summary of Results

SETUP Mode		PV Temp (°C)			DC PV Voltage (V)		Irradiation (W/m²)
SS – 1 Air cooling Alucore and conventional	High	PV1- 40.6	PV2- 35.3	PV1- 21.76	PV2- 21.98	939.8	
	Average	PV1- 35.2	PV2- 31.2	PV1- 19.96	PV2- 20.56	480.24	
	Low	PV1- 33.2	PV2- 29.9	PV1- 18.43	PV2- 19.66	276.4	
	Difference %		12.6		3.0	-	
	High	PV1- 64.9	PV2- 55.6	PV1- 21.39	PV2- 21.95	1160.9	
SS – 2 Air and water and conventional	Average	PV1- 43.1	PV2- 38.1	PV1- 19.83	PV2- 20.6	625.71	
	Low	PV1- 36.8	PV2- 31 29.9	PV1- 17.47	PV2- 18.81	221.2	
	Difference		12.55		3.95	-	
	High	PV1- 64.5	PV 2- 56.9	PV1- 20 19.75	PV2- 20.59	1055.4	
	Average	PV1- 62.3	PV 2- 55.0	PV1- 19.75	PV2- 20.49	987.39	
SS – 3 Alucore conventional and water	Low	PV1- 61.1	PV 2- 54.5	PV1- 19.63	PV2- 20.41	884.5	
	Difference %		11.90		3.76	-	
	High	PV1- 52.6	PV 2- 46.1	PV1- 6.36	PV2- 7.04	884.5	
	Average	PV1- 45.8	PV 2- 41.1	PV1- 5.05	PV2- 5.68	655.74	
	Low	PV1- 35 33.5	PV 2- 33.5	PV1- 3.42	PV2- 3.59	440.48	
SS-4 Battery charging	Difference %		10.84		14.09	-	

Site data was collected and specific setups fabricated to study specific aspects on the PV-TEG system under site weather conditions. The results from the weather data collected from the Kisumu weather station revealed that the site has adequate irradiation with a daily average Direct Nominal Irradiation (DNI) of 6.02 kW/m²/day as shown on Figure 4.6 as compared to the national average DNI of 6.02 kW/m²/day. The annual average ambient temperature for the Kisumu site is slightly higher at 27.26 °C compared to that observed at the IJET-JKUAT of 23.3°C. This temperature difference is mainly

attributed to the fact that IEET-JKUAT is at a higher altitude of 1460 meters above sea level and has humidity of 50% (Kituu G.M et al., 2010) compared to the Nyalenda Kisumu site low altitude of 1131 meters above sea level and higher site humidity of 59%. This site ambient temperature would result in higher PV cell temperature that would adversely affect the electricity generation. The measured conventional air-cooled PV cell temperature is also higher in Nyalenda Kisumu for the same reason.

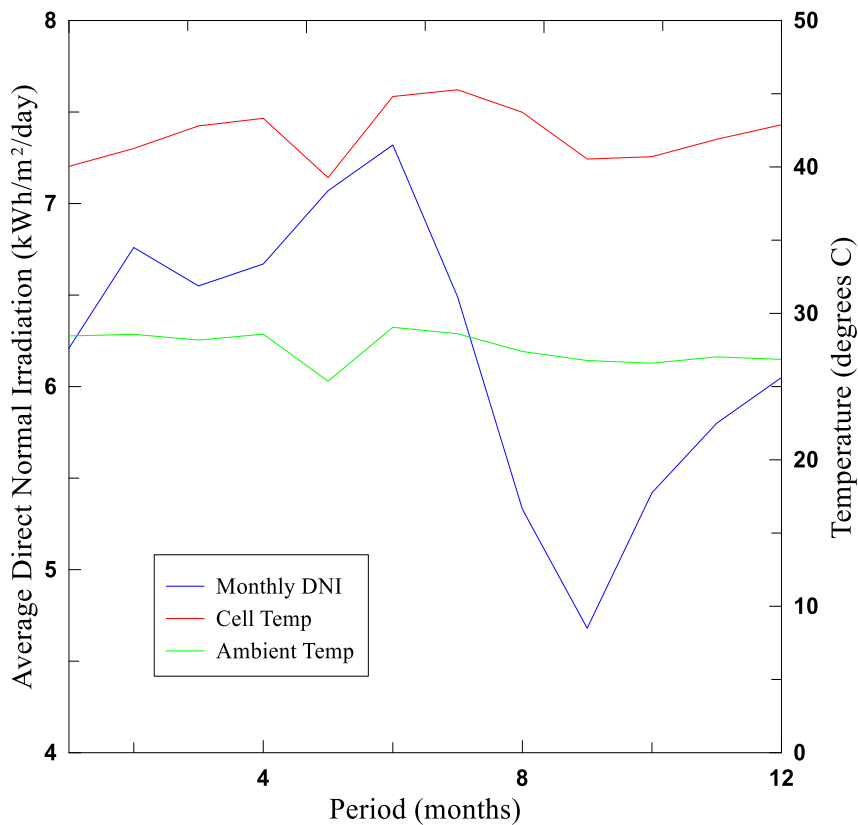


Figure 4.6: Nyalenda Kisumu Annual Weather Pattern and Irradiation

Specific Setup 1 is fabricated using two 13 Wp PV modules mounted on the roof to measure conventional PV and PV-TEG temperature and voltage. The conventional PV is air cooled while the PV-TEG is cooled when floating on a water pool in a vessel. Results obtained presented good irradiance recorded during the experiment with a low and high irradiance of 525 W/m² and 967.4 W/m² respectively. The air-cooled PV recorded

higher cell temperature at 59.6 °C compared to the water-cooled PV-TEG PV that recorded a high cell temperature of 57.25 °C with an average percentage difference of 2.4% between the air cooled and water-cooled PV modules. Figure 4.7 shows the graphical presentation of the PV and PV-TEG cell temperatures, ambient temperature and irradiance. During this setup measurements, the ambient temperature was ranging from a low value of 27.3 °C to a high value of 31.2 °C.

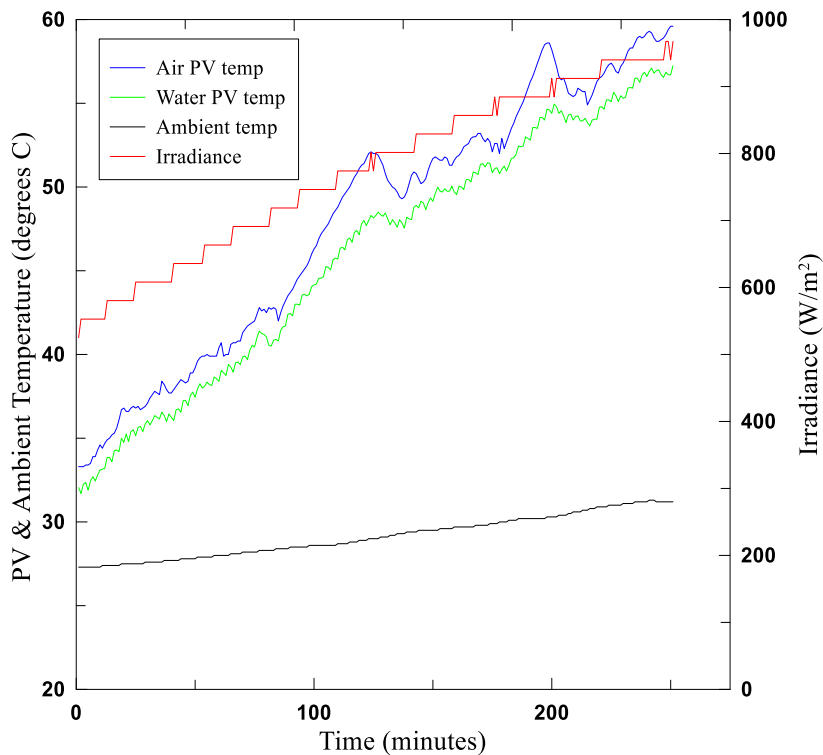


Figure 4.7: Roof Mount PV Temperature Measurements

The results obtained from the voltage measurements shows the water-cooled PV-TEG module maintaining a higher voltage output compared to the air-cooled module during the entire measurement period as in Figure 4.8. The water-cooled PV-2 obtained a minimum voltage of 20.3 volts at an irradiance of 810.8 W/m² and a maximum voltage of 21.11 volts at an irradiance of 865.2 W/m², while the air-cooled PV-1 obtained a minimum voltage of 17.96 volts at an irradiance of 725.2 W/m² and a maximum value of 20.71 volts at an irradiance of 830.5 W/m². The average percentage voltage difference

between the air-cooled PV-1 and water-cooled PV-2 was ranging between 1.88% and 13.36%. The TEG system generated an average voltage of 1.24 volts with a peak of 1.63 volts obtained at a PV cell temperature of 56.85 °C. These results confirm that the PV-TEG system is capable of saving 3.83% of the PV voltage and an additional voltage generated using the TEG modules when the system is operated under a passive water-cooling environment as the voltage difference shown graphically in Figure 4.8.

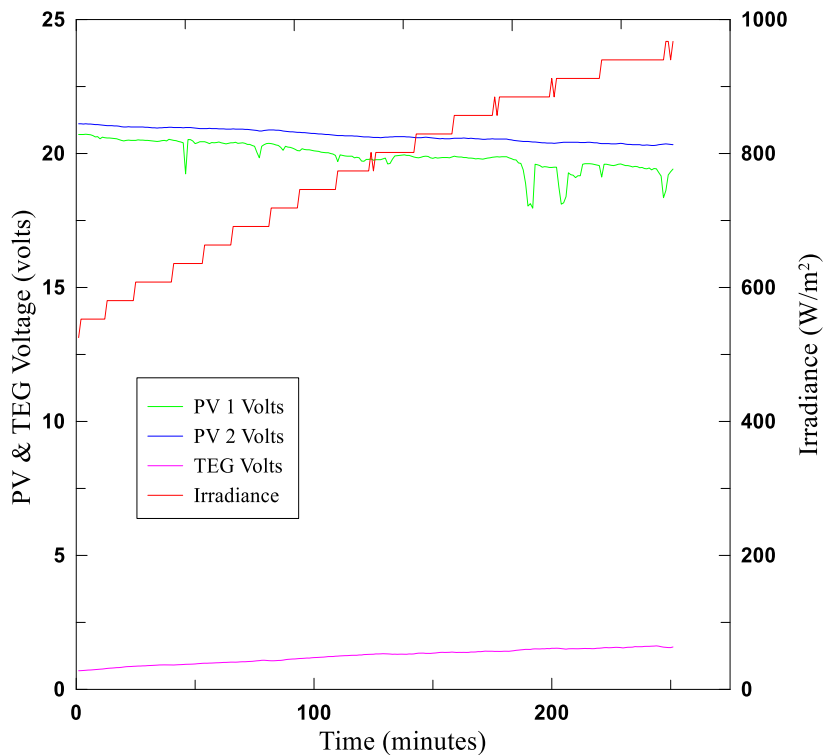


Figure 4.8: Roof Mount PV Voltage Measurements

Specific Setup 2 is fabricated using a design sample size PV module of 275 Wp that is floated in a plastic water pool mounted at near ground level as shown in Figure 3.10. Results obtained from this setup achieved a peak irradiance of 1022 W/m² that suddenly reduced to 304.1 W/m² then reduced gradually to 110.5 W/m² by the end of the measurement, maintaining an average irradiance of 501.14 W/m². The PV cell temperature recorded a high value of 54.9 °C with an average cell temperature of 40.6 °C and a low value of 24.2 °C at the end of the measurements. The peak PV output

voltage obtained was 36.45 volts D.C while the average voltage was 33.76 volts D.C and the lowest PV voltage output was 33.22 volts D.C. The TEG system sandwiched at the back plate, was able to generate a peak voltage of 17.8 volts D.C and an average voltage of 13.34 volts D.C with the lowest voltage obtained being 5.6 volts D.C when the PV cell temperature was only 26.5 °C at the end of the setup measurements. The results are presented graphically in Figure 4.9.

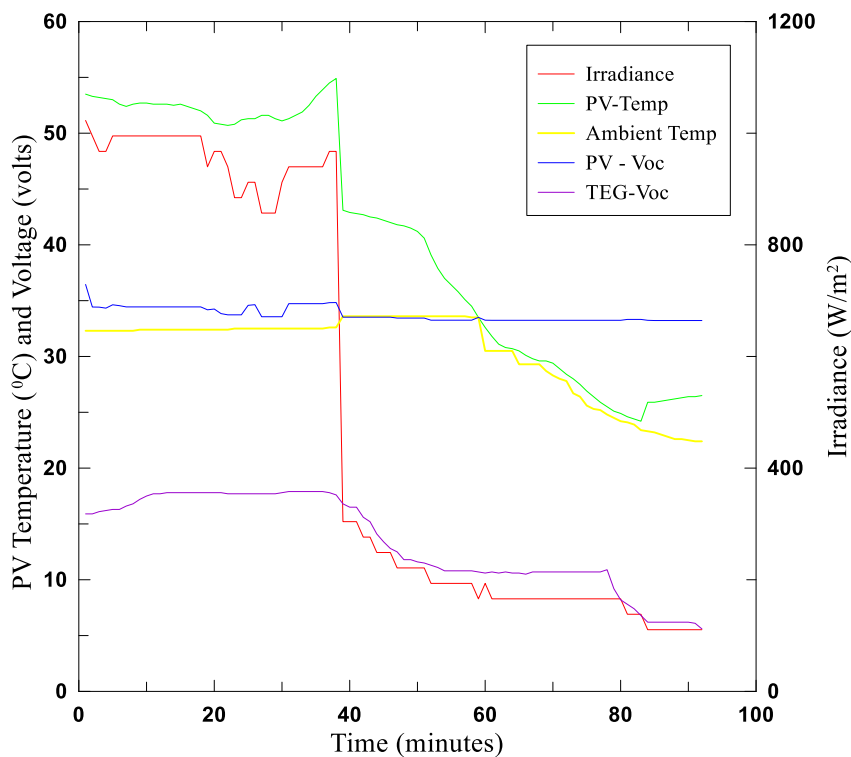


Figure 4.9: 275 Wp PV Ground Mount Temperature and Voltage Measurements

4.3 TEG Modeling and Test Bench Fabrications

4.3.1 Model Validation and Simulation Outcomes

Simulation results from the developed model agree with the TEG theory and are validated with previous work done by (Karami & Moubayed, 2014). Figure 4.10 presents a comparative analysis of the two studies. For the four parameters analysed, the trend is quite similar in both studies. The study by Karami N. et al however shows much

lower values compared to the present study results because of the type of TEG used as they were not identical and also because gains were used in the current study for precision's sake and trace visibility.

The sharp picks observed in the power and efficiency graphs, Figures 4.10 (c) and Figure 4.10 (d), respectively, are due to the time period for the simulations. The behaviour of the TEGs however follows the same trend though the magnitude of the electrical outputs were different confirming the difference in samples used. From Figures 4.10 (a) and Figure 4.10 (b), the voltage and current display higher values that rise gradually with time and temperature gradient to a high value of 0.75 V and the current peak of 0.14 mA. On the other hand, the TEG power rises to a peak of 20 mW and the efficiency rises to 11%.

The observed values mostly depended on accurate matching of the simulation load resistance to the TEG internal resistance and the temperature gradient which are closely matched.

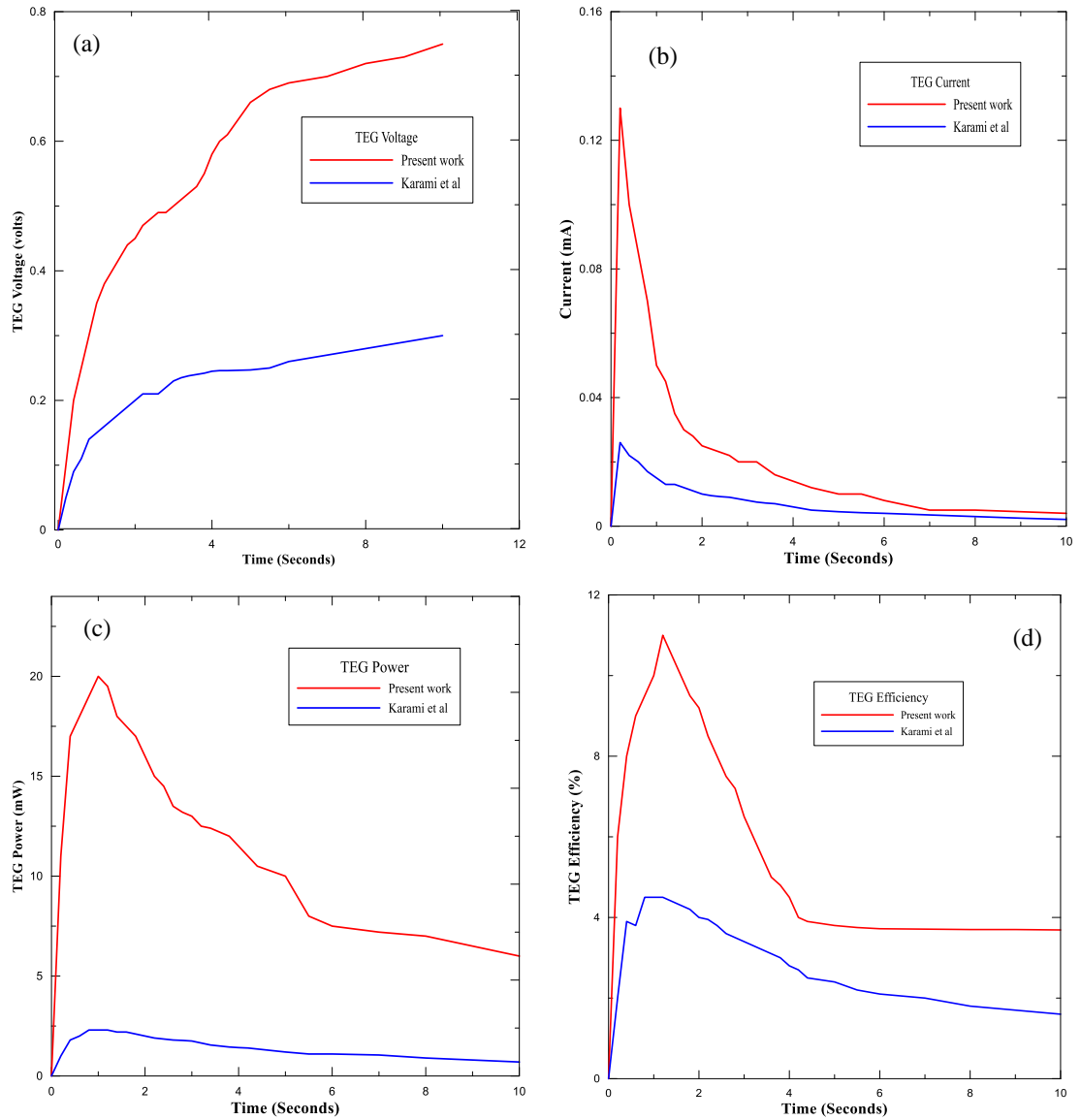


Figure 4.10: Validation of present work; (a) Voltage, (b) Current, (c) Power and (d) Efficiency

4.3.2 Bench Setups Outcomes

The bench setups in the laboratory succeeded the numerical simulations and results show that as T_h increases to the pre-set value of $69.2\text{ }^\circ\text{C}$ and ΔT also increases, the TEG voltage increased to 0.6 V, 1.29 V and 2.41 V D.C for one, two and four TEGs setups, respectively, as presented in Figure 4.11 (a) and Figure 4.11 (b). This was observed by

Montecucco A. et al (2014). The current had a negligible variance as expected due to series connection where the TEG maximum currents were 113.3 mA, 114.6 mA and 119 mA for the one, two and four TEGs, respectively, as presented in Figure 4.11 (c) and Figure 4.11 (d). For one, two and four TEGs, the power increased to 73.98 mW, 134 mW and 287.39 mW as presented in Figure 4.11 (e) and Figure 4.11 (f), respectively. These results show that by matching the TEG internal resistance to the load or interface device resistance and connecting individual TEG modules in series the output voltage can be scaled-up increasing the power obtainable from the TEG modules. This is analogous to PV cells operation. Consequently, connecting such strings in parallel increases the current output and this was used as the basis for continued field trials on the RAS site at Nyalenda Kisumu.

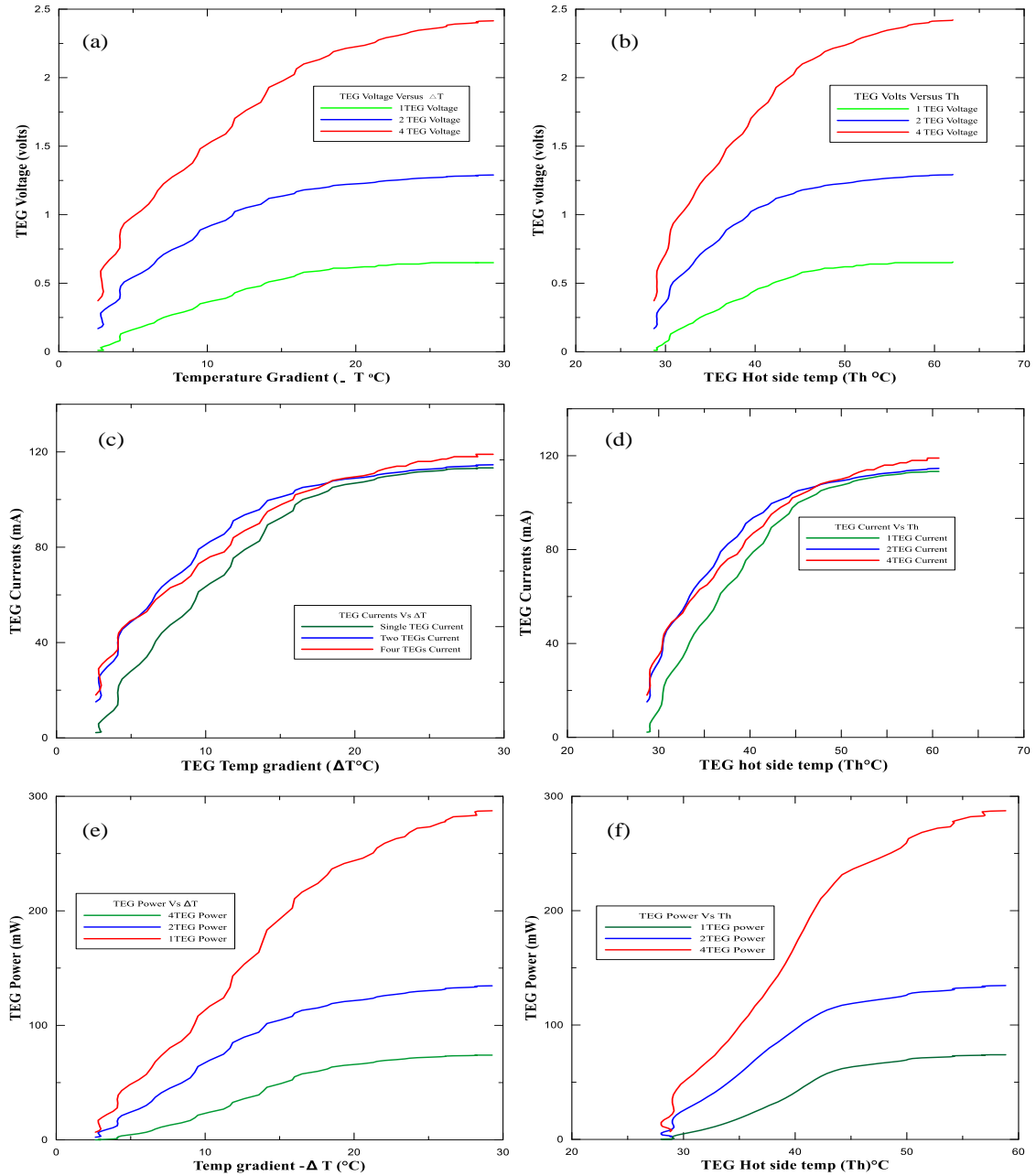


Figure 4.11: TEG Bench Setup output measurements; (a) Voltages / ΔT , (b) Voltages / T_h (c) Currents/ ΔT , (d) Currents / T_h (e) Power / ΔT and (f) Power / T_h

4.3.3 Final System Design Implications

From the study investigations and using the daily energy requirements for the RAS as calculated in Table 3.3.3 to be 63.22 kWh and the site annual average DNI of 6.02 kWh/m²/day, the PV-TEG system is designed using the national annual DNI of 6.02 kWh/m²/day and a 19.13 kWp PV system is obtained which is equivalent to 20 kWp. The system is designed using the national annual average DNI of 6.02 kWh/m²/day so that the extra site irradiation takes care of any energy shortfall that may arise. The PV system consists of 72 modules of 275 Wp each. One PV module accommodates 600 TEG modules that will be capable of generating a peak power output of 43.7 W, so the total peak power from the TEG system is expected to be 3,146 W. The entire TEG system will be connected in a series-parallel formation to achieve a nominal voltage of the 48 VDC able to charge the same battery bank as the PV system. The TEG system directly contributes an additional 15.7% to the 20 kWp of the PV system power output. In addition, the PV system would generate 1.05% more power as compared to the original setup without cooling.

4.4 Evaluation of Thermal Interface Materials in Mediating PV Cell Temperature Mismatch in PV-TEG Power Generation

The discussion of our findings is split into three main parts. First, we determine the variation characteristics of temperature mismatch between the PV cells of the same module and compare the measured cell temperature variances, the second part examines the results obtained when the thermal interface materials are used under the cell to improve the temperature distribution. Lastly, we determine the effects of using the three types of thermal interface materials, on the temperature and TEG voltage generation mismatch.

4.4.1 Numerical Analytical Solution and Preliminary PV Module Cell Temperature Measurement

The PV cell temperature numerical analytic solution sought to provide an assessment of the cell temperature under the conditions and environment of measurement. These results provided the representative module cell temperature for the 36 cells on the PV module. This cell temperature was then used as the normalized reference cell temperature for comparison with the measured cell temperatures under those conditions and environment. The analysis results are presented in Figure 4.4.1 (a) showing how the cell temperature varied with irradiation, ambient temperature and the mean of the measured cell matrix temperatures. The graph of the mean of the measured cell matrix temperatures closely traces the numerical temperature curve validating the entire process. The slight difference observed between -9.3% and 8.66% with an average of 1.97% between the measured mean and simulated temperature accounts for the temperature variance between the individual cell matrices. Both the temperatures were responsive to the amount of irradiance available and responded sluggishly to the ambient temperature as in Figure 4.4.1 (a). During this experiment, the irradiance varied between 160 W/m^2 and 960 W/m^2 and the ambient temperature varied between $19.9 \text{ }^\circ\text{C}$ and $26.7 \text{ }^\circ\text{C}$ and resulted in the numerically analyzed PV cell temperatures that varied between $30.82 \text{ }^\circ\text{C}$ and $69.84 \text{ }^\circ\text{C}$.

From the temperature measurement results, it is observed that the measured cell temperatures are indeed different as shown in Figure 4.12 (b) as opposed to the general expectation that they would be the same since the cells are exposed to uniform irradiance (Y.-R. Li et al., 2019; Soliman et al., 2020). These measured cell temperature results also confirm and agree with the findings by Tina G. et al. (2008) (Tina & Abate, 2008) who observed higher cell temperature at the most central cell compared to the outer cells. In Figure 4.12 (b), the numerical cell temperature is also plotted to compare it with the measured temperatures and the graph fits closely among the measured matrix cell temperature response plots. Figure 4.12 (c) then shows the variance of the measured individual cell matrix temperatures as compared to the simulated temperature and Table

4.2 presents the summary of variance for each cell matrix. The aspect of temperature mismatch and its effects agree with findings by Montecucco A et al (2014)

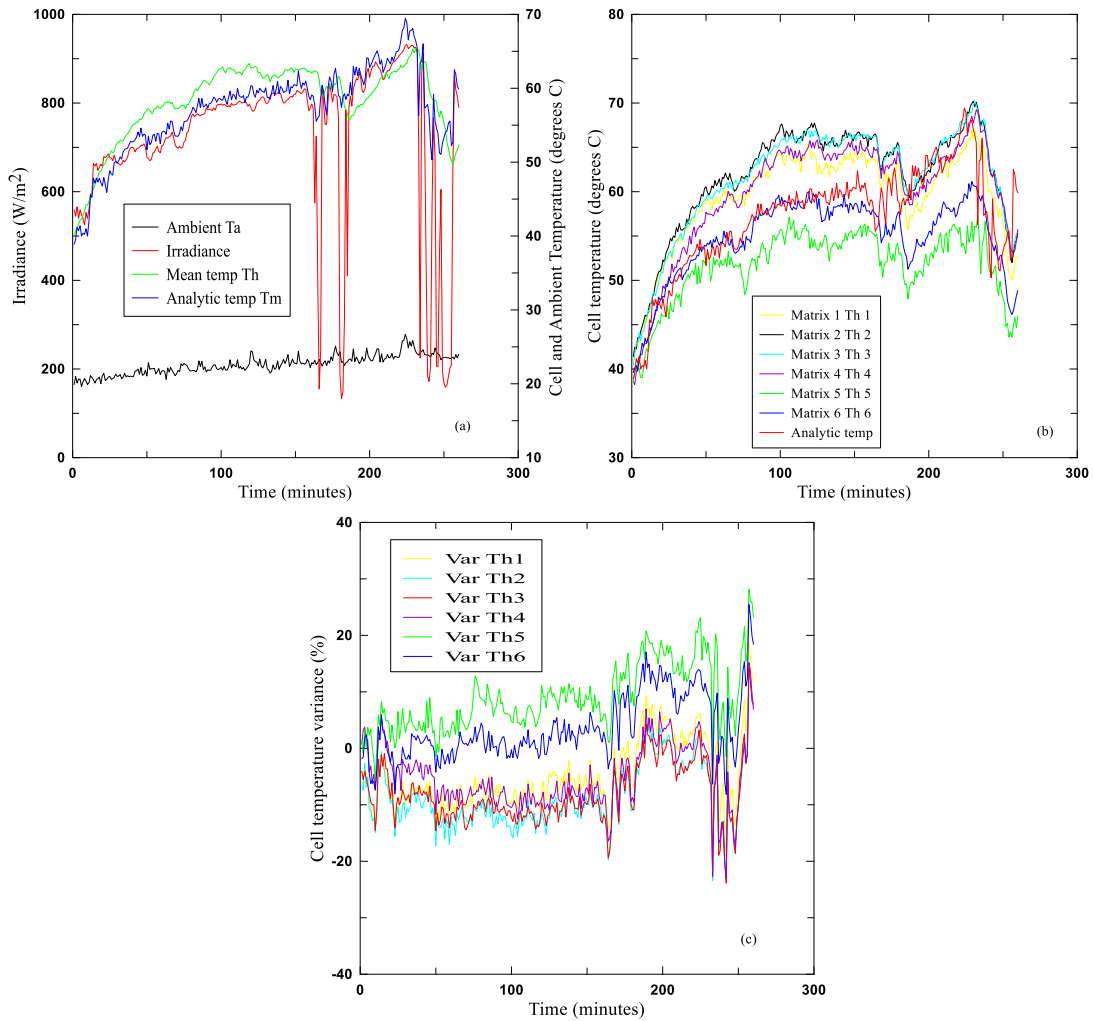


Figure 4.12: (a) Irradiance & temperatures, (b) Measured & numerical temperature (c) Matrix temperature variance.

Table 4.2: Bare cell matrix temperature variance

Matrix Number	Variance (%)	Total Variance (%)
Matrix 1 Th 1	-19.39 to 18.88	38.28
Matrix 2 Th 2	-23.39% to 15.2	38.59
Matrix 3 Th 3	-23.86 to 14.16	38.02
Matrix 4 Th 4	-23.06 to 15.12	38.18
Matrix 5 Th 5	-5.78 to 28.16	33.94
Matrix 6 Th 6	-7.4 to 25.44	32.84

As observed in Table 4.2, there is high temperature variance between the cell matrix temperatures and the analyzed cell temperature with variances ranging from 32.84% on matrix 6 to a high of 38.59% on matrix 2. This cell matrix temperature variance is expected to create a corresponding variance in the operating temperature gradient ΔT of the TEG modules that are coupled to the PV cells making them generate voltages at different MPPs (Montecucco et al., 2014) due to their varying hot side temperatures, T_h as in Equations 2.7 and 3.3.1. When the generated voltages and currents are different, series strings and parallel interconnections of TEG modules results in voltage conflicts and current mismatches that lead to power losses just like in PV and battery systems. In principle, the higher potential TEG string shall drive current towards the lower potential string until the two voltages become equal (Royne et al., 2005). Based on this observation, it is therefore beneficial to make the cell temperatures at the hot side of the TEG modules as uniform as possible. This would ensure the TEG modules generate uniform or near uniform voltage resulting in reduced or no interconnection power losses (J. Zhang et al., 2020b).

4.4.2 Systematic PV Cell Temperature Measurement under TIMs

In this sub-section, the temperature responses of three thermal interface materials are examined experimentally following the observations made from temperature variance between the bare PV cells in the preceding setups. Figure 4.13 shows the temperature response of the PV cells under the TIMs with the PV modules being subjected to the same irradiance. The mean of the measured cell matrix temperatures from each module,

is used to determine the percentage temperature variance of each cell matrix. Results obtained from this experiment show the cells under graphite TIM having a temperature variance ranging between -5.17% and 4.59% adding up to 9.76% and graphically presented in Figure 4.13 (a), the heat spreader has a variance ranging between -3.45% and 2.25% adding up to 5.7% {Figure 4.13 (b)} and the aluminum foil has a variance ranging between -8.81% and 6.41% adding up to 15.22% as also presented in Figure 4.13 (c) graphically. The variances observed under the TIMs are way below what was observed when the temperatures were measured on bare cells where the variance was ranging between 32.84% and 38.59% also measured under normal open air-cooling conditions. This translated to PV cell temperature mismatch mitigation of 70.3% - 74.7%, 82.6% - 88.2% and 53.7% - 60.6% for the three TIMs, respectively.

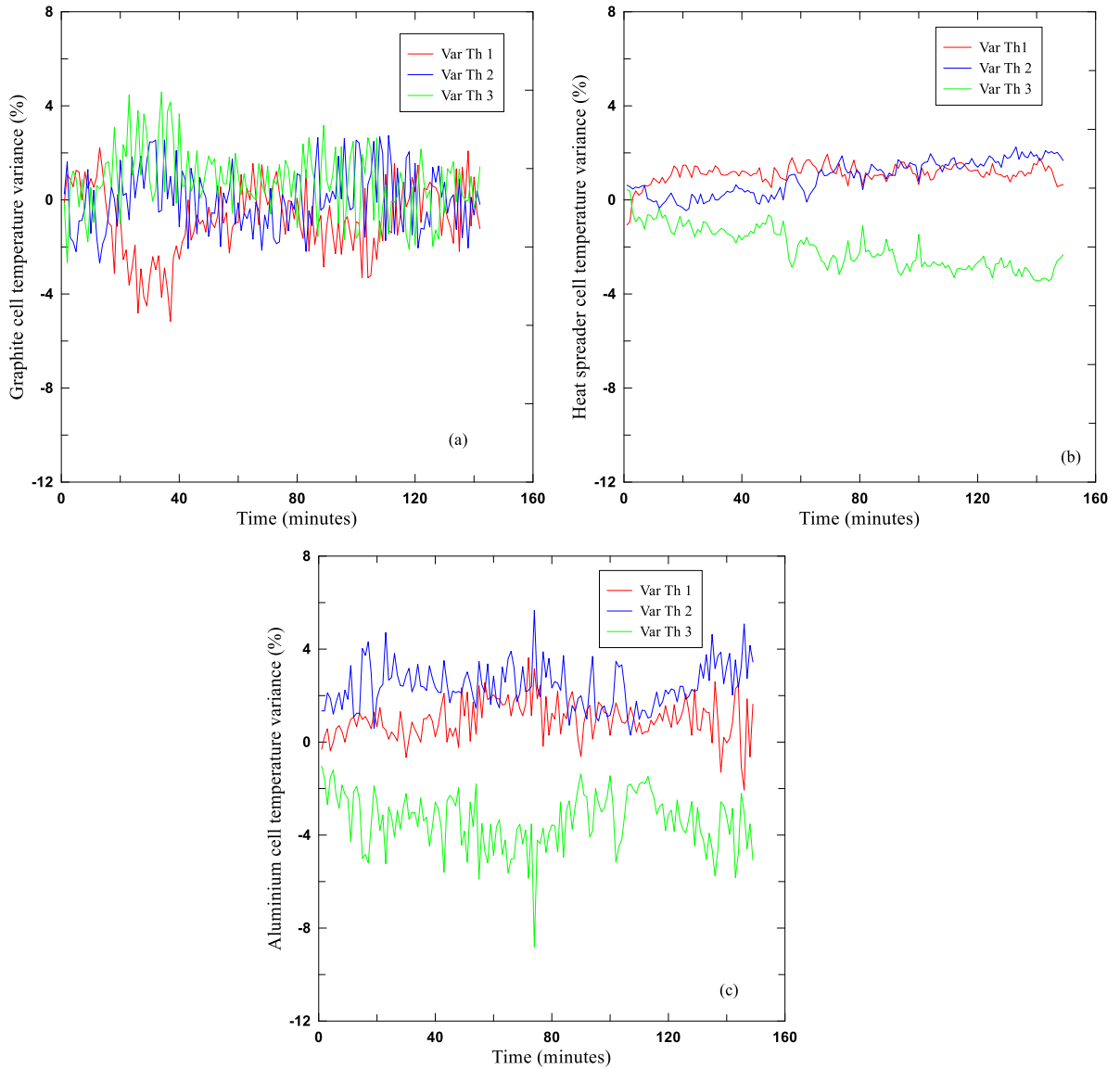


Figure 4.13: Variance on PV cell temperature distribution under different TIMs (a) graphite sheet (b) heat- spreader (c) aluminum foil

It is observed that among the TIMs used, the heat spreader presented the lowest cell temperature variance followed by the graphite sheet and the aluminum foil presented the highest variance. The thermal conductivity of the TIMs contributed a lot to the observed temperature variance though the aluminum TIM did not behave as was expected. The divergent performance of the aluminum TIM could have been attributed to surface

texture and presence of micro-scale roughness (Y. Chen & Xuan, 2015) and probably the difference in the Coefficient of Thermal Expansion (CTE) of the three materials where say, for aluminum, α is $(21-24)\times 10^{-6}/^{\circ}\text{C}$ and $(4-8)\times 10^{-6}/^{\circ}\text{C}$ for graphite (J. K. Chen & Huang, 2013). With the reduced cell temperature variance by the TIMs, it is expected that the temperature distribution on the TEG modules shall subsequently be uniform and/or almost equal. This temperature uniformity is also expected to create a uniform ΔT across the TEG modules that will generate uniform voltages.

4.4.3 PV cell temperature and TEG voltage measurements under TIMs.

In this sub-section, the effects of module temperature on TEG voltage generation under three thermal interface materials are examined experimentally following the observations made in the preceding setups where the TIMs improved the temperature distribution at the back of the PV cells.

4.4.3.1 PV-TIM-TEG under Air cooled environments

In these setups, the variance in both temperature and voltages is calculated as a percentage difference of the actual measured values to the mean of the measured values. During this experiment, the sky was partially clear with some cloud casts and fluctuating irradiance that started at 990 W/m^2 then briefly dropped to 466 W/m^2 and later rose to a peak of 988 W/m^2 . By the end of the measurements period, irradiance had reduced to 287 W/m^2 maintaining an average irradiance of 735.3 W/m^2 . The bare cells setup presented the highest temperature and voltage variance, at $\pm 8.7\%$ for temperature and $\pm 28.64\%$ for voltage as shown in Figures 4.14 (a) and 4.15 (a), respectively due to the setup intervention conditions and dominant weather as compared with the open-air conditions in section 4.4.1. The heat spreader setup on the other hand, presented the lowest temperature variance at $\pm 0.98\%$ and a voltage variance of $\pm 1.71\%$ as shown in Figures 4.14 (c) and 4.15. (c), respectively. The graphite sheet setup presented temperature variance of $\pm 2.19\%$ and a voltage variance of $\pm 5.49\%$ as shown in Figures

4.14 (b) and 4.15 (b), respectively. Finally, the aluminum foil setup presented temperature variance of $\pm 2.31\%$ and a voltage variance of $\pm 7.83\%$ as shown in Figures 4.14 (d) and 4.15 (d), respectively.

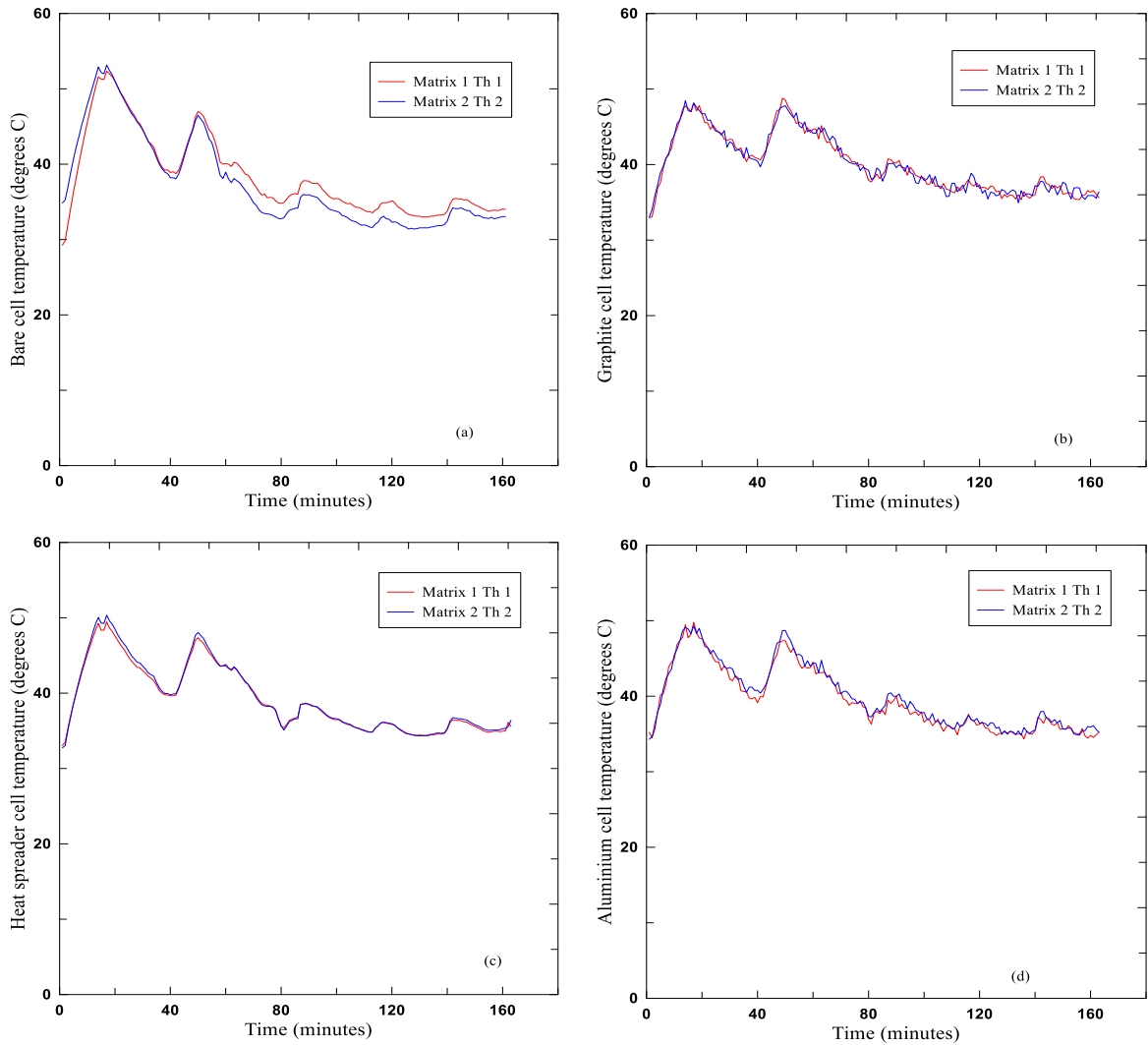


**Figure 4.14: PV-TEG Cell temperature distribution under air-cooled environments
(a) bare cell (b) graphite sheet (c) heat spreader (d) aluminum foil**

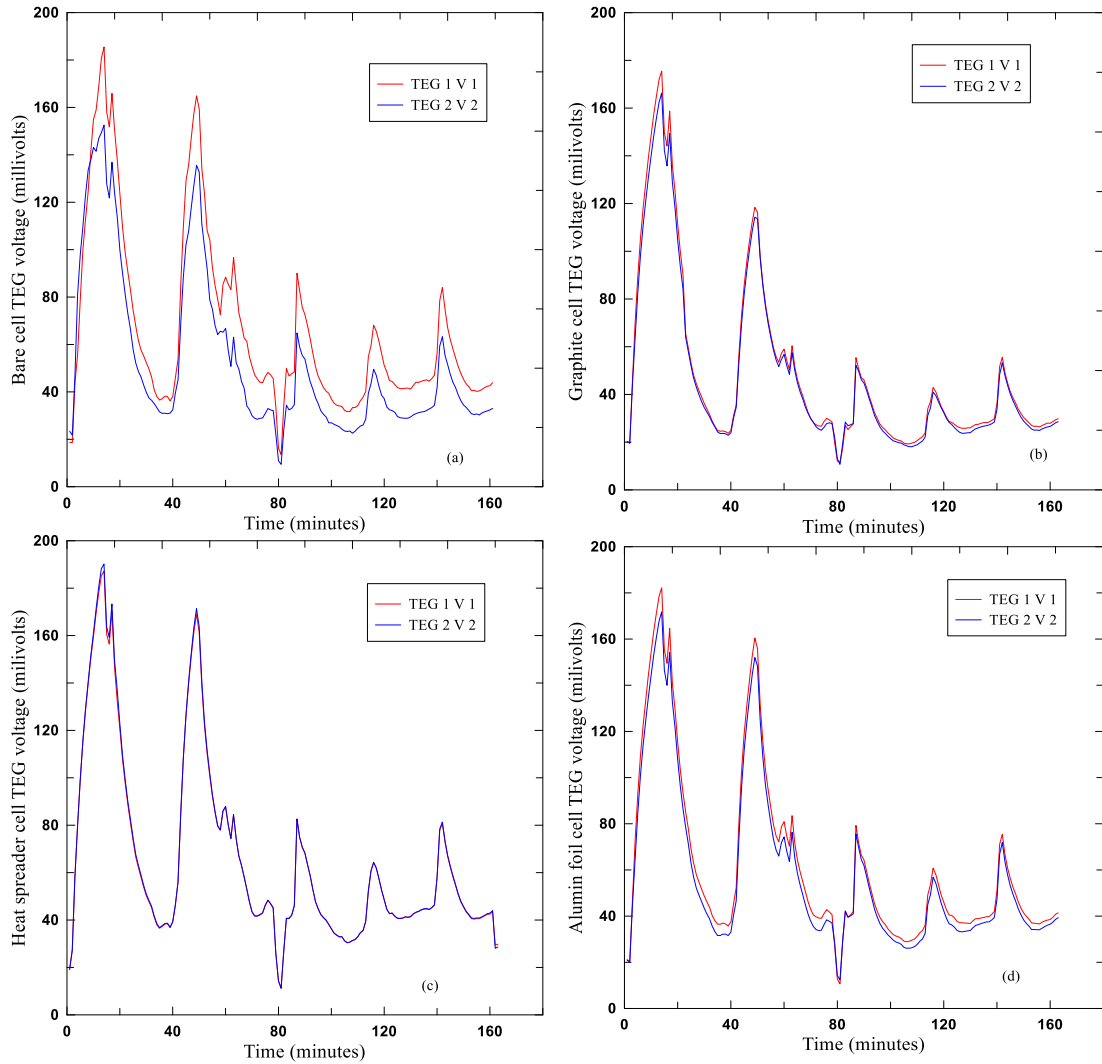


Figure 4.15: TEG voltages under air cooled TIMs (a) bare cell (b) graphite (c) heat spreader (d) aluminum foil

The results in Figures 4.14 and 4.15 confirm that temperature mismatch reduced significantly when thermal interface materials are used. The temperature mismatch for the TIM modules was much lower with the lowest being a total variance of 1.96% with the heat spreader. This low variance when using the TIMs resulted into a total TEG voltage variance of 3.42% compared with that of the bare cells of 56.8%. The observed

high voltage variance in the bare cell TEGs is due to the micro scale roughness of the PVF and the ceramic surface of the TEGs

(J. K. Chen & Huang, 2013; J. Zhang et al., 2020a; X. Zhang & Zhao, 2015). Once again the aluminum foil presented higher variances than the graphite sheet for reasons cited earlier on surface texture and CTE, but still far better than the bare cell variances (J. K. Chen & Huang, 2013; Y. Chen & Xuan, 2015).

The results obtained in this setup are a clear disclosure that when PV-TEG hybrid systems are well coupled using the right TIM with the lowest Thermal Contact Resistance (TCR), the performance of the TEG voltage output is significantly improved (K. Li et al., 2014; Lin et al., 2015; J. Zhang et al., 2020a).

4.4.3.2 PV-TIM-TEG under water cooled environments

Similarly, in this measurement, the variance in both temperature and voltages is calculated as a percentage difference of the actual measured values to the mean of the measured values. During these measurements, the temperature of the cooling water rose from 22.8 °C at the start to 24.7 °C by the end of measurements. The sky was very clear most of the time and the average irradiance was generally above 860 W/m² starting from 868 W/m² and rising to a high of 905 W/m² and later rising above 936 W/m². Once again in this setup, the bare cells setup had the highest temperature and voltage variance at ±5.58% and ±19.77%, respectively as shown in Figures 4.16 (a) and Figure 4.17 (a). The heat spreader once again exhibited the lowest temperature variance at ±0.82% and a voltage variance of ±1.62% as shown in Figures 4.16 (c) and Figures 4.17 (c). While the graphite sheet presented temperature variance of ±1.96% and a voltage variance of ±2.86% as shown in Figures 4.16 (b) and Figures 4.17 (b). Here also the aluminum foil presented higher temperature variance of ±2.17% and a voltage variance of ±3.18% as shown in Figures 4.16 (d) and Figures 4.17 (d) despite the fact that aluminum has a higher thermal conductivity than the graphite sheet. This performance is attributable to

reasons cited earlier on surface texture and effects of CTE in section 4.3.1 (J. K. Chen & Huang, 2013; Y. Chen & Xuan, 2015).

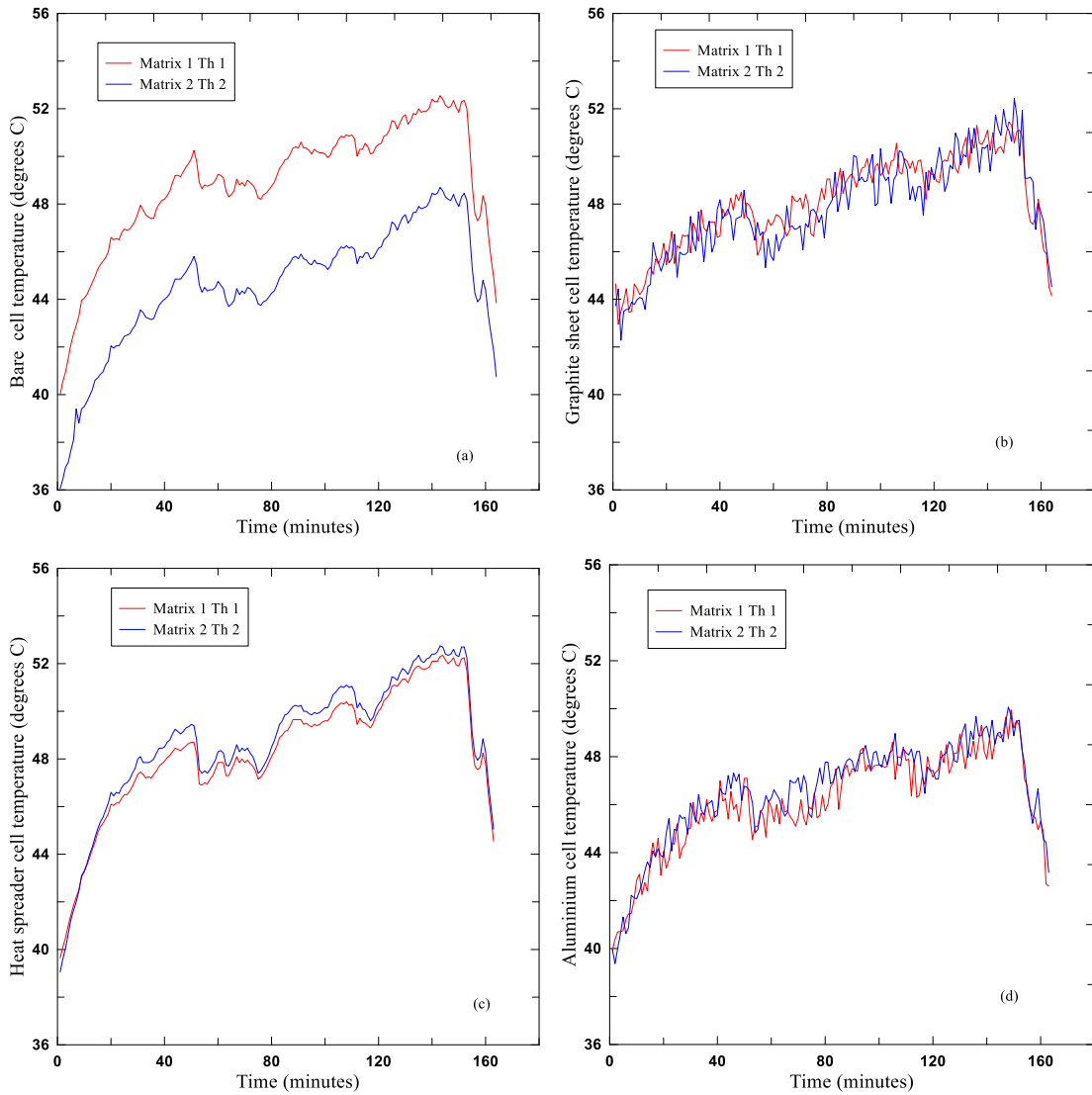


Figure 4.16: Cell temperature distribution under water-cooled environment (a) bare cell (b) graphite (c) heat spreader (d) aluminum foil

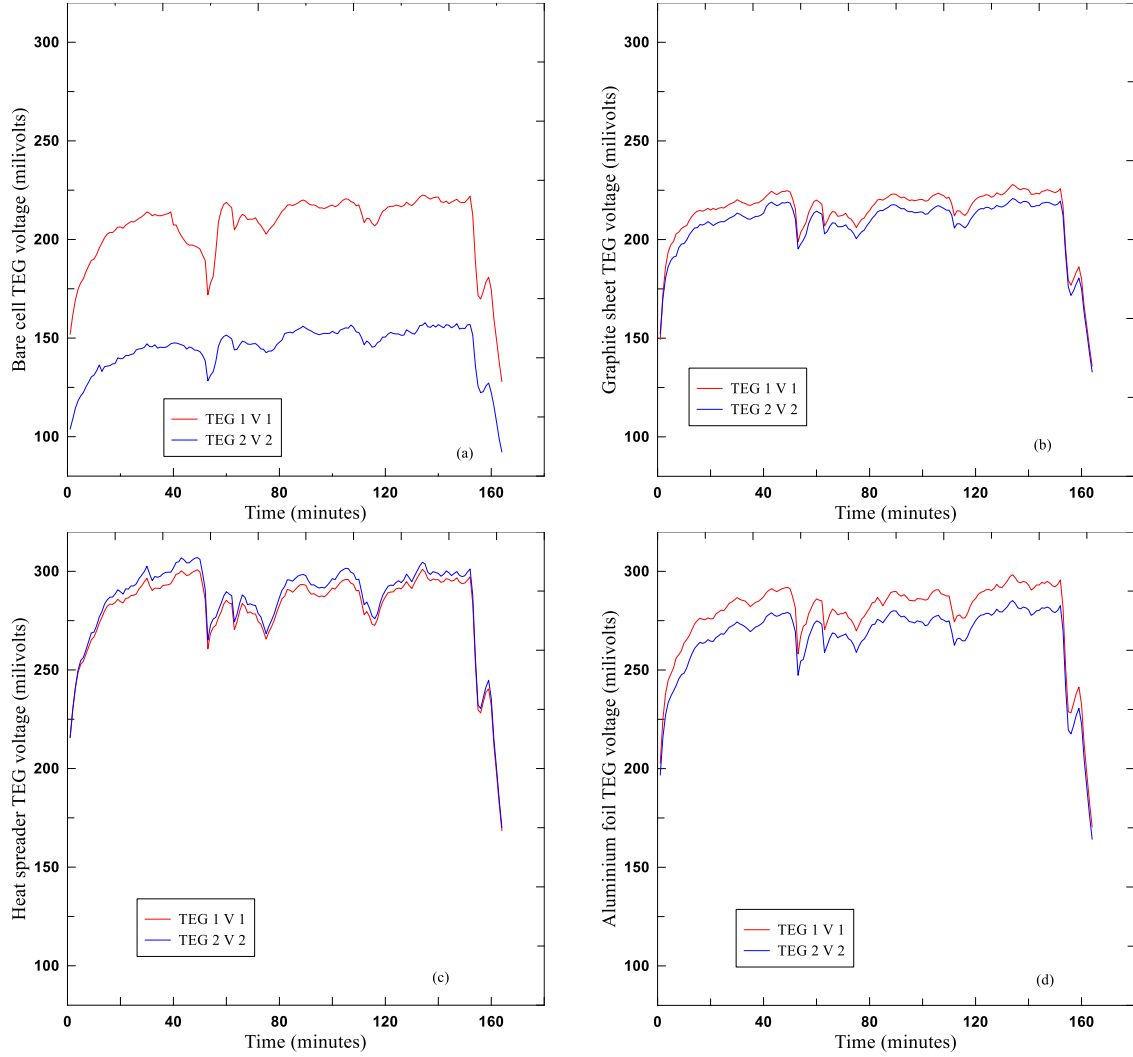


Figure 4.17: TEG voltages under water cooled TIMs (a) bare cell (b) graphite (c) heat spreader (d) aluminum foil

Results obtained in 4.4.3.1 and 4.4.3.2 show that temperature mismatch results in a proportional mismatch on TEG voltage output such that as the mismatch increases, the voltage difference also increases. Figures 4.14 (a), Figure 4.15 (a), Figure 4.16 (a) and Figure 4.17 (a) reveal the usual effect of the temperature gradient, ΔT in PV-TEG systems on the TEG voltage output (Engin ÖZBAŞ, 2019). The cooling water temperature maintained a higher ΔT that resulted in higher voltage output in the water cooling as compared to the air cooling setups and this confirms that water has better

cooling properties (J. Zhang et al., 2020a). In the water-cooled setup, the highest total TEG voltage was 604.14 mV peak is generated under the heat spreader as compared to a high of 377.4 mV for the air-cooled setup generated under the heat spreader.

With the PV module physical dimensions (L×W×H) as 325 mm × 325 mm × 20 mm and those of the TEG module (L×W×H) being 40 mm×40 mm×3.4 mm and while accounting 25% dead space between TEGs and PV edges, the PV module would comfortably accommodate 49 TEG modules on its back plate. From the best results obtained under air cooling with TIM (H.S), the total TEG voltage for each PV-TEG assembly shall be 9.31 V (V_{oc}) at an irradiance of 972 W/m² and a temperature of 50.05 °C, while the PV module alone generates about 19.41 V (V_{oc}) under the same conditions, calculated using the manufacturer's Temperature Coefficient of Voltage (TCV) of -0.0875 V/°C. The water-cooled system under the same TIM (H.S) on the other hand would yield a TEG voltage of 15.03 V (V_{oc}) at an irradiance of 905 W/m² and temperature of 49.05 °C, while the PV module generates about 19.5 V (V_{oc}) under the same conditions. Therefore, an additional 47.96% voltage is realized from the TEG system when HS is used under air cooling and an additional 77.08% voltage under water cooling.

Without any mode of cooling, at irradiance of 933 W/m² the PV bare cells temperature rose to 63.32 °C and the ambient temperature was 26.1 °C, while at an irradiance of 908 W/m² the cell temperature corresponded to 62.62 °C and the ambient temperature was around 23.65 °C, from the results obtained in section 4.4.1. Using a TCV of -0.0875 V/°C, the PV (V_{oc}) is calculated to be 18.25 V (V_{oc}) at 63.32 °C and 18.31 V (V_{oc}) at a cell temperature of 62.62 °C. So, the voltage gains on air cooling under HS at irradiance of 933 W/m² at a cell temperature of 44.65 °C as in section 4.3.1, is 8.93%. While the voltage gains under water cooling on HS at irradiance of 907 W/m² at a cell temperature of 48.8 °C, is 6.96%. On average both the methods of cooling save above 5% of the bare cell PV open circuit voltage.

The three investigated TIMs offered relatively similar improvements in temperature distribution under the PV that resulted in voltage gain compared with the bare cell PV. The main factor that affected the performance of the TIMs was their texture, surface roughness and the thermal conductivity as observed by (K. Li et al., 2014) the performance of the graphite sheet and aluminum foil could probably improve if some silica-gel (with tolerance of 200 °C) is used on the surface to reduce the air trapped between the surfaces (K. Li et al., 2014).

Overall, the PV-TIM-TEG system realized an additional power gain of 1.8% and 2.5% from the PV module under air and water cooling, respectively, when HS TIM is used compared with a no cooling scenario. The total additional power improvements from the PV-TIM-TEG assembly under water-cooled environment is 24.85% based on the best output, while with air cooling, a gain of 19.7% at best output was realized.

4.5 Economic Analysis of the PV-TEG Hybrid System

The total cost of materials for the system is Ksh.9197857 as in Table 3.5.1 while the cost of engineering design and project managements is evaluated as a percentage to Ksh.19019.91, the installation labor cost is also evaluated as a percentage to Ksh.810896.13 and the freight and packaging cost is Ksh.270298.71 making the total cost of the project to be Ksh.10297071.75. This total cost of the project and the Operation and Maintenance (O&M) including other costs like land rates are used for the economic and financial evaluation of the project. The annual energy delivery by the PV-TEG system is 35,344 kWh and the kilowatts peak output of the plant is 19.8 kW.

(i) Net Present Value

The NPV is evaluated using the total cost of the project and the CBK discount rate of 15% for the period so as to observe the response of the project. The inflation rate used was obtained from the Kenya National Bureau of Statistics (KNBS) as 5.71%. The O&M cost has been provided including the cost of replacement of components that will

need replacement in the mid-term before the 25-year project life period. It is observed that the project returns a negative NPV at the CBK discount rate of 15% but returns a positive NPV at a lower discount rate of 8.94% which is a possible negotiable discount rate. The cost of the project has been influenced mostly by the cost of storage, TEG component and their auxiliary accessories. It is expected that with continuous development of these technologies, their costs and even sizes shall reduce with increased efficiencies. The PV-TEG technology and Lithium-ion storage are at the horizon of future electricity generation and will be immensely embraced as cost and efficiency issues get resolved.

(ii) Internal Rate of Return

The internal rate of return is evaluated using the total cost of the project against the avoided costs as project revenues and IRR of 8.94% is obtained as the discount rate that returns a zero NPV. The IRR is also lower than the CBK discount rate of 15%, but on economic terms the IRR is acceptable because the project has other national and social benefits that are not considered in the evaluation because of the scope of study.

(iii) Payback Period

The payback period for the project has been evaluated as 12.85 years making the project attractive and also leaving the remaining 14 years as a net benefit to the developer.

(iv) The Profitability Index

The PI obtained is less than one and also negative making the project appear unprofitable.

This occurrence is quite common in new technologies due to the cost of initial development and intellectual monopoly.

CHAPTER FIVE

CONCLUSIONS AND RECOMMENDATIONS TO FURTHER WORK

5.1 Conclusions

The conclusions to this research work are presented in section format according to the findings made during the study. But largely, from the results obtained in this study, solar PV+TEG hybrid systems have been observed to be technically very viable and have a promising future as the technology improves as a result of concerted research in the area of PV cells, TEG figure of merit and thermal interface materials. In the Nyalenda 20 kWp PV+TEG system, the system is capable of generating an additional 2.35% to 6.85% as a result of PV cell cooling alone, and an additional 18% to 22.5% or 4400 W to 3600 W from the TEG system alone under water cooling environment and Heat spreader thermal interface materials sandwiched between the PV and TEGs. This power gain then results into a total PV+TEG system efficiency improvement of 24.85%.

5.1.1 Data Collection at JKUAT –IEET for PV-TEG Hybrid System Development

In this section the main aspects under study are PV module cell temperature on a conventional and cooled module condition and later effects of cooling on the PV module open circuit voltage. An Alucore honey comb cooling panel is used to enhance the PV module cooling and also provide a means of sandwiching thermoelectric generators to create adequate temperature gradient that would enable the TEGs generate electricity. A weather station was installed to collect 24 hours' irradiance and temperature data for a period of one year that would be used to assess the available annual irradiation and guide the PV-TEG hybrid design. Four (4) specific setups are also fabricated for measurement of temperature and voltage under varying environmental conditions. The results show that going by the average annual irradiation of 4.6 kWh/m² observed at the IEET-JKUAT site, there will be adequate solar irradiation at the Kisumu site considering that Kisumu is closer to the equator than IEET-JKUAT. The results also confirm that some

considerable power is lost due to the rise in the PV cell temperature. 3 specific setups show cell temperature difference ranging from 10.8% to 12.6% and a corresponding PV module voltage difference ranging between 3% and 3.95%. The fourth specific setup that was fabricated for battery charging, has a temperature difference of 10.84% and a power difference of 14.09%. From the results, it is apparent that the proposed PV-TEG hybrid system shall result in substantial power saving compared to a convention PV system, saving up to 5% on PV alone. The TEGs generated 1.1 volts in SS-2 and 2.11 volts in SS-3 implying that the TEG system shall also contribute some considerable amount of power harvested from the PV waste heat.

5.1.2 Site Studies for Design of the PV-TEG Hybrid System to Run the Autonomous Aquaculture System

In this section, the same aspects studied in section 3.1 of the chapter were being studied further but this time under actual site weather conditions. From the results obtained, it is concluded that there is adequate solar irradiation on site as an annual average DNI value of 6.02 kW/m^2 was recorded. The average ambient temperature observed on site is higher than that observed at the IEET-JKUAT site hence justifying the use of the PV-TEG hybrid system under such environmental conditions. The results from the two setups fabricated for measurement of PV temperature and output voltage confirm that the PV-TEG hybrid system results in considerable higher voltage output compared to its conventional counterpart with a higher mean difference of 3.87 % and a peak of 13.36 %. Some additional power shall also be generated by the TEG system that harvests the PV system waste heat. The average percentage PV cell temperature difference of 2.24 % observed with a peak difference of 3.15 % would result in considerable PV power loss on the conventional system. The TEG voltage generation output was very encouraging but still lower than expected at 50 % of the PV module value. Therefore, further investigations are performed to enhance the TEG system performance. These investigations are based on the main aspects of TEG string interconnections and PV cell temperature distribution whose enhancement shall enable a selection that will lead to an improved performance of the designed PV-TEG hybrid system.

5.1.3 TEG Modeling and Test Bench Fabrications

In this section, a TEG numerical model has been developed and simulated in MATLAB Simulink and test bench fabrications made for specific setup measurements. It has been shown both numerically and experimentally following a simulation approach that;

When TEG modules' internal resistance is matched to the load impedance, maximum power output and efficiency of up to 9% is achievable and when the PV system operating temperature is reduced by the TEG and cooling panels, about 1% of the PV power is gained. Further it has been shown that when TEG modules are stuck under PV modules especially in a tropical environment with PV temperatures ranging from 50 °C to 69.2 °C, between 18% and 22.5% of the PV power, that is equal to 4400 watts and 3600 watts in the Kisumu system, can be generated by the TEG system array resulting in substantial additional amounts of power to the PV system. Also, the performance efficiency of the whole PV+TEG system increases by 24.85% due to the cooling effect of the TEG with water on the cold side.

These results demonstrate that when TEGs are connected in an initial series adding voltage formation to form a string and then in parallel adding currents formation while their total internal resistance is matched to the load, they can be relied on in generating considerable electrical power. These findings confirm that PV+TEG power generation is highly attractive and promising with better efficiencies and that the developed system for the Kisumu Nyalenda autonomous RAS can also be replicated in other sites with similar environmental conditions.

5.1.4 Evaluation of Thermal Interface Materials in Mediating PV Cell Temperature Mismatch in PV-TEG Power Generation Systems

Investigations on temperature mismatch show that bare cells have higher temperature variance of $\pm 8.7\%$ with a corresponding higher voltage variance of $\pm 28.64\%$ under air

cooling and temperature variance of $\pm 5.58\%$ and a voltage variance of $\pm 19.77\%$ under water cooling.

Use of TIMs significantly mediates PV cell temperature variance resulting in remarkable TEG voltage output improvements in the PV-TIM-TEG system setup. Furthermore, the efficient heat transfer also results in considerable reduction of the PV cell temperature improving its voltage and power output. For the three investigated TIMs, the heat spreader, PH-3, showed the lowest temperature and voltage variance under both air and water-cooled conditions. The effect of using TIMs (HS) in cooling the PV cells resulted in additional power of 19.7% under air cooling and 24.85% when water-cooled with the benefits increasing at higher temperatures. Hence remarkable results have been realized in this study with a sum total gain of 19.7% with air cooling and 24.85% with water cooling when heat spreader is used, which gives an opportunity to investigate other emerging TIMs.

5.1.5 Economic Analysis and Viability of the PV-TEG Hybrid System

The economic analysis has been carried out on a 19.8 kW_p solar PV-TEG power generation plant designed to supply power to the autonomous RAS at Nyalenda in Kisumu. The PV-TEG system has been designed to meet the RAS energy requirements 8 hours a day full capacity and 16 hours running essential equipment like the hatcheries and pond water circulation. The PV system consists of 72, 275 W_p modules, 43200 TEG modules, 7 charge controllers, 12 *2.5 kWh lithium-ion batteries and a 20 kW_p inverter. The project has obtained a negative NPV at CBK rate, but a positive NPV at 8.94% discount rate evaluated using the inflation effects, nominal cash flow and nominal discount rate. The discount rate is lower than the CBK rate but it is a possible negotiable rate. The payback period is attractive at 12.85 years though using the PI the project appears unprofitable with a PI of less than one.

5.2 Recommendations for Future Work

Many diverse methods have been used to analyze and simulate the solar PV-TEG systems and the economic analysis has been carried out on it as an autonomous standalone system used to supply power to a RAS. The system and technology used to hybridize with solar PV is fairly current and still developing. The battery storage technology (Lithium ion) is also fairly current and also still developing.

Future work in the field of PV+TEG hybrid systems shall involve mainly, improving the PV cell uniform temperature distribution mainly on the back plate- Tedlar, development of thermal interface materials that shall provide uniform temperature distribution under the back PV module plate. Further work shall involve development of thermoelectric material that have higher figure of merit so as to improve the TEG power efficiency and development of cheaper heat sinking cooling panels will also enhance wide spread development of PV-TEG systems.

REFERENCES

- Abu-Rahmeh, T. M. (2017). Efficiency of Photovoltaic Modules Using Different Cooling Methods: A Comparative Study. *Journal of Power and Energy Engineering*, 05(09), 32–45.
- Adeeb, J., Farhan, A., & Al-Salaymeh, A. (2019). Temperature Effect on Performance of Different Solar Cell Technologies. *Journal of Ecological Engineering*, 20(5), 249–254.
- Al Siyabi, I., Khanna, S., Sundaram, S., & Mallick, T. (2018). Experimental and Numerical Thermal Analysis of Multi-Layered Microchannel Heat Sink for Concentrating Photovoltaic Application. *Energies*, 12(1), 122.
- Alami, A. H. (2014). Effects of evaporative cooling on efficiency of photovoltaic modules. *Energy Conversion and Management*, 77, 668–679.
- Ali, M., Ali, Hafiz. M., Moazzam, W., Babar Saeed, M., & Mechanical Engineering Department, University of Engineering and Technology Taxila, Pakistan. (2015). Performance enhancement of PV cells through micro-channel cooling. *AIMS Energy*, 3(4), 699–710.
- Ali, N., Teixeira, J. A., & Addali, A. (2018). A Review on Nanofluids: Fabrication, Stability, and Thermophysical Properties. *Journal of Nanomaterials*, 2018, 1–33.
- Al-Shohani, W. A. M., Al-Dadah, R., & Mahmoud, S. (2016). Reducing the thermal load of a photovoltaic module through an optical water filter. *Applied Thermal Engineering*, 109, 475–486.
- Atsu, D., & Dhaundiyal, A. (2019). Effect of Ambient Parameters on the Temperature Distribution of Photovoltaic (PV) Modules. *Resources*, 8(2), 107.

- Bayrak, F., Oztop, H. F., & Selimefendigil, F. (2020). Experimental study for the application of different cooling techniques in photovoltaic (PV) panels. *Energy Conversion and Management*, *212*, 112789.
- Bernard Muok & Debajit Palit. (2015). *Solar PV for enhancing electricity access in Kenya*.
- B.S Dallon, J. Schumann, & F. Lesage. (2015). Performance evaluation of a photoelectric–thermoelectric cogeneration hybrid system. *Solar Energy*, *118*, 276–285.
- Chandrasekar, M., & Senthilkumar, T. (2015). Experimental demonstration of enhanced solar energy utilization in flat PV (photovoltaic) modules cooled by heat spreaders in conjunction with cotton wick structures. *Energy*, *90*, 1401–1410.
- Chen, A., & Wright, P. (2012). *Medical Applications of Thermoelectrics* (pp. 1–22).
- Chen, J. K., & Huang, I. S. (2013). Thermal properties of aluminum–graphite composites by powder metallurgy. *Composites Part B: Engineering*, *44*(1), 698–703.
- Chen, Y., & Xuan, Y. (2015). The influence of surface roughness on nanoscale radiative heat flux between two objects. *Journal of Quantitative Spectroscopy and Radiative Transfer*, *158*, 52–60.
- Cuce, E., Bali, T., & Sekucoglu, S. A. (2011). Effects of passive cooling on performance of silicon photovoltaic cells. *International Journal of Low-Carbon Technologies*, *6*(4), 299–308.
- D. Rowe. (1999). Thermoelectrics and environmentally friendly sources of electrical energy. In *Thermoelectrics and environmentally friendly sources of electrical energy*, *16*, 1251–1256).

- Dalala, Z. M. (2016). Energy harvesting using thermoelectric generators. *2016 IEEE International Energy Conference (ENERGYCON)*, 1–6.
- Dalla Longa, F., & van der Zwaan, B. (2017). Do Kenya's climate change mitigation ambitions necessitate large-scale renewable energy deployment and dedicated low-carbon energy policy? *Renewable Energy*, *113*, 1559–1568.
- David M Rowe. (2006). Thermoelectric materials. In *Thermoelectrics Hand book, Macro to Nano* (First, pp. 1–6 to 1–10). Taylor and Francis group.
- Deng, S., Cai, X., Zhang, Y., & Li, L. (2019). Enhanced thermoelectric performance of twisted bilayer graphene nanoribbons junction. *Carbon*, *145*, 622–628.
- Deng, Y., Zhu, W., Wang, Y., & Shi, Y. (2013). Enhanced performance of solar-driven photovoltaic–thermoelectric hybrid system in an integrated design. *Solar Energy*, *88*, 182–191.
- Divya Mittal¹, Bharat Kumar Saxena¹, & Rao¹, K.V.S. (2017). Floating Solar Photovoltaic Systems: An Overview and their Feasibility at Kota in Rajasthan. *2017 IEEE. 2017 International Conference on Circuits Power and Computing Technologies [ICCPCT]*.
- Dousti, M. J., Petraglia, A., & Pedram, M. (2015). *Accurate Electrothermal Modeling of Thermoelectric Generators*. 1603–1606.
- Duffie, J. A., & Beckman, W. A. (2013). *Solar Engineering of Thermal Processes: Duffie/Solar Engineering*. (4 ed.). John Wiley & Sons, Inc.
- Enescu, D. (2019). Thermoelectric Energy Harvesting: Basic Principles and Applications. In D. Enescu (Ed.), *Green Energy Advances*. IntechOpen.

- Engin ÖZBAŞ. (2019). Experimental Investigation of Passive Water Cooling in Solar Heating Thermoelectric Generator. *Journal of Polytechnic*. Retrieved from <http://dergipark.gov.tr/politeknik>
- Ewa Klugmann-Radziemska & Patrycja Wcisło-Kucharek. (2017). *Photovoltaic module temperature stabilization with the use of phase change materials*.
- F. Kawtharani, M. Hammoud, A. Hallal, A. Shaito, & A. Assi, I. Assi. (2017). Cooling P.V Modules using phase change materials. *2017 29th International Conference on Microelectronics (ICM)*. 29th International conference on microelectronics (ICM0, Beitut, Lebanon.
- Fattouh, B., Poudineh, R., & West, R. (2019). The rise of renewables and energy transition: What adaptation strategy exists for oil companies and oil-exporting countries? *Energy Transitions*, 3(1–2), 45–58.
- Ferrara, C., & Philipp, D. (2012). Why Do PV Modules Fail? *Energy Procedia*, 15, 379–387.
- Filip Grubišić-Čabo, Sandro Nižetić, & Tina Giuseppe Marco. (2016). Photovoltaic Panels: A Review of the Cooling Techniques. *Transactions Of Famena*, XL(Special issue).
- Fisac, M., Villasevil, F. X., & López, A. M. (2014). High-efficiency photovoltaic technology including thermoelectric generation. *Journal of Power Sources*, 252, 264–269.
- Frobenius, F., Gaiser, G., Rusche, U., & Weller, B. (2016). Thermoelectric Generators for the Integration into Automotive Exhaust Systems for Passenger Cars and Commercial Vehicles. *Journal of Electronic Materials*, 45(3), 1433–1440.

- Geisz, J. F., France, R. M., Schulte, K. L., Steiner, M. A., Norman, A. G., Guthrey, H. L., & Moriarty, T. (2020). Six-junction III–V solar cells with 47.1% conversion efficiency under 143 Suns concentration. *Nature Energy*, 5(4), 326–335.
- Giaretto, V., & Campagnoli, E. (2020). The Elusive Thomson Effect in Thermoelectric Devices. Experimental Investigation from 363 K to 213 K on Various Peltier Modules. *Metals*, 10(2), 291.
- H. Gichungi. (2012). *Solar Potential in Kenya*. Retrieved from https://www.sv.uio.no/iss/english/research/projects/solar-transitions/announcements/Kenya-Henry_Gichungi.pdf
- H. Nagayoshi & T. Kajikawa. (2006). Mismatch Power Loss Reduction on Thermoelectric Generator Systems Using Maximum Power Point Trackers. *International Conference on Thermoelectrics*.
- Hashim, H., Bomphey, J. J., & Min, G. (2016). Model for geometry optimisation of thermoelectric devices in a hybrid PV/TE system. *Renewable Energy*, 87, 458–463.
- Hsu, C.-T., Huang, G.-Y., Chu, H.-S., Yu, B., & Yao, D.-J. (2011). An effective Seebeck coefficient obtained by experimental results of a thermoelectric generator module. *Applied Energy*, 88(12), 5173–5179.
- Hussien, H. A., Hasanuzzaman, M., Noman, A. H., & Abdulmunem, A. R. (2013). *Enhance Photovoltaic/Thermal System Performance by Using Nanofluid*. 5.
- Jakhrani A.Q, Othman A.K, Rigit R.A.H, & Samo S.R. (2011). Comparison of Solar Photovoltaic Module Temperature Models. *World Applied Sciences Journal 14 (Special Issue of Food and Environment)*.

- Joshua Hill. (2019). *Africa Solar PV market by 2030* [Solar PV Market]. German Solar Association (BSW-Solar) and the Becquerel Institute;
- Jradi, M., Ghaddar, N., & Ghali, K. (2012). Experimental and theoretical study of an integrated thermoelectric-photovoltaic system for air dehumidification and fresh water production. *International Journal of Energy Research*, 36(9), 963–974.
- Kai Sun, & Zhaoxin Qiu, Hongfei Wu. (2016). *Evaluation on High-efficiency Thermoelectric Generation Systems Based on Differential Power Processing*. IEEE Transactions on Industrial Electronics.
- Kane, A., & Verma, V. (2013). Characterization of PV cell-environmental factors consideration. *2013 International Conference on Power, Energy and Control (ICPEC)*, 26–29.
- Kanimba, E., & Tian, Z. (2016). Modeling of a Thermoelectric Generator Device. In S. Skipidarov & M. Nikitin (Eds.), *Thermoelectrics for Power Generation—A Look at Trends in the Technology*. InTech.
- Karami, N., & Moubayed, N. (2014). New modeling approach and validation of a thermoelectric generator. *2014 IEEE 23rd International Symposium on Industrial Electronics (ISIE)*, 586–591.
- Energy Act*, Energy and petroleum regulatory commission (2019) (testimony of Kenya government).
- Kerr, G., & Benard Muok. (2014). *Dissemination of Solar Energy Technologies in Kenya for Rural Electrification: Challenges & Opportunities*.
- Kidegho G.Guyo, Kinyua Robert, Muriithi Christopher, & Njoka Francis. (2020). Innovative Solar Photovoltaic and Thermoelectric Power Generator for a

Recirculating Aquaculture System. *International Journal of Renewable Energy Research-IJRER*, 10(3)

Kishi, M., Nemoto, H., Hamao, T., Yamamoto, M., Sudou, S., Mandai, M., & Yamamoto, S. (1999). Micro thermoelectric modules and their application to wristwatches as an energy source. *Eighteenth International Conference on Thermoelectrics. Proceedings, ICT'99 (Cat. No.99TH8407)*, 301–307.

Kituu G.M, Shitanda D, Kanali C.L, Mailutha J.T, Njoroge C.K, Wainaina J.K, & Bongyereire J.S. (2010). A Simulation Model for Solar Energy Harnessing By the Tunnel Section of a Solar Tunnel Dryer. *CIGR Ejournal, Vol. XII*.

Kolambekar, R. B., & Bhole, K. (2015). Development of prototype for waste heat energy recovery from thermoelectric system at Godrej vikhroli plant. *2015 International Conference on Nascent Technologies in the Engineering Field (ICNTE)*, 1–6. <https://doi.org/10.1109/ICNTE.2015.7029943>

Kwan, T. H., & Wu, X. (2017). TEG Maximum Power Point Tracking Using an Adaptive Duty Cycle Scaling Algorithm. *Energy Procedia*, 105, 14–27.

Lashin, A., Al Turkestani, M., & Sabry, M. (2019). Concentrated Photovoltaic/Thermal Hybrid System Coupled with a Thermoelectric Generator. *Energies*, 12(13), 2623.

Li, G., Chen, X., & Jin, Y. (2016). Analysis of the Primary Constraint Conditions of an Efficient Photovoltaic-Thermoelectric Hybrid System. *Energies*, 10(1), 20.

Li, G., Chen, X., & Jin, Y. (2017). *Analysis of the Primary Constraint Conditions of an Efficient Photovoltaic-Thermoelectric Hybrid System*. 12.

- Li, K., Liu, C., & Chen, P. (2014). A 1 KW Thermoelectric Generator for Low-temperature Geothermal Resources. *Thirty-Ninth Workshop on Geothermal Reservoir Engineering*, 12.
- Li, Y.-R., Su, C.-C., & Chang, S.-H. (2019). Applying Aluminum–Vertically-Aligned Carbon Nanotube Forests Composites for Heat Dissipation. *Nanomaterials*, 9(5), 758.
- Lin, J., Liao, T., & Lin, B. (2015). Performance analysis and load matching of a photovoltaic–thermoelectric hybrid system. *Energy Conversion and Management*, 105, 891–899.
- Lincot, D. (2017). The new paradigm of photovoltaics: From powering satellites to powering humanity. *Comptes Rendus Physique*, 18(7–8), 381–390.
- Lv, S., Qian, Z., Hu, D., Li, X., & He, W. (2020). A Comprehensive Review of Strategies and Approaches for Enhancing the Performance of Thermoelectric Module. *Energies*, 13(12), 3142.
- Maturi, L., Belluardo, G., Moser, D., & Del Buono, M. (2014). BiPV System Performance and Efficiency Drops: Overview on PV Module Temperature Conditions of Different Module Types. *Energy Procedia*, 48, 1311–1319.
- MOE. (2018). *Kenya National electrification strategy; Key highlights* (Key Highlights, p. English) [Highlights]. ministry of energy.
- Montecucco, A., Siviter, J., & Knox, A. R. (2014). The effect of temperature mismatch on thermoelectric generators electrically connected in series and parallel. *Applied Energy*, 123, 47–54.

- Musthafa, M. M. (2015). Enhancing Photoelectric Conversion Efficiency of Solar Panel by Water Cooling. *Journal of Fundamentals of Renewable Energy and Applications*, 05(04).
- Nabil Karami and Nazih Moubayed. (2014). New Modeling Approach and Validation of a Thermoelectric Generator. *IEEE*.
- Nejad, A. R., Nejad, A. R., Abedi, M. E., & Nejad, A. R. (2017). Production of electrical power in very extreme-temperature environmental conditions: A new implementation of thermoelectric generators. *2017 IEEE 6th International Conference on Renewable Energy Research and Applications (ICRERA)*, 468–472.
- Newell, P., Phillips, J., Pueyo, A., Kirumba, E., Ozor, N., & Urama, K. (2014). The Political Economy of Low Carbon Energy in Kenya. *IDS Working Papers, 2014*, 445, 1–38.
- N.K.Kasim, Hazim H.Hussain, & Alaa N.Abed. (2019). Performance Analysis of Grid-Connected CIGS PV Solar System and Comparison with PVsyst Simulation Program. *International Journal of Smart Grid*, 3(4), 172–179.
- Olaya, D., Tseng, C.-C., Chang, W.-H., Hsieh, W.-P., Li, L.-J., Juang, Z.-Y., & Hernández, Y. (2019). Cross-plane thermoelectric figure of merit in graphene—C60 heterostructures at room temperature. *FlatChem*, 14, 100089.
- Paraskevas, A., & Koutroulis, E. (2016). A simple maximum power point tracker for thermoelectric generators. *Energy Conversion and Management*, 108, 355–365.
- Peng, Z., Herfatmanesh, M. R., & Liu, Y. (2017a). Cooled solar PV panels for output energy efficiency optimisation. *Energy Conversion and Management*, 150, 949–955.

- Peng, Z., Herfatmanesh, M. R., & Liu, Y. (2017b). Cooled solar PV panels for output energy efficiency optimisation. *Energy Conversion and Management*, *150*, 949–955.
- Radwan, A., & Ahmed, M. (2017). The influence of microchannel heat sink configurations on the performance of low concentrator photovoltaic systems. *Applied Energy*, *206*, 594–611.
- Rajkumar, V. A., Weijers, C., & Debije, M. G. (2015). Distribution of absorbed heat in luminescent solar concentrator lightguides and effect on temperatures of mounted photovoltaic cells. *Renewable Energy*, *80*, 308–315.
- Razak, A., Irwan, Y. M., Leow, W. Z., Irwanto, M., Safwati, I., & Zhafarina, M. (2016). Investigation of the Effect Temperature on Photovoltaic (PV) Panel Output Performance. *International Journal on Advanced Science, Engineering and Information Technology*, *6*(5), 682.
- Reiss H, Fuller C.S, & Morrid F. J. (n.d.). Chemical interactions among defects in germanium and silicon. *Citation Classis, August 1979. J35, :535-636*
- Robert Freer & Anthony V. Powell. (2019). Realising the potential of thermoelectric technology: A Roadmap. *Journal of Materials Chemistry C*.
- Roger A Messenger (last) & Jerry Ventre. (2010). *Photovoltaic systems engineering* (3rd ed.). Taylor and Francis group. Retrieved from <http://www.crcpress.com>
- Rosa-Clot, M., Rosa-Clot, P., Tina, G. M., & Ventura, C. (2016). Experimental photovoltaic-thermal Power Plants based on TESPI panel. *Solar Energy*, *133*, 305–314.
- Rose, A., Stoner, R., & Pérez-Arriaga, I. (2016). Prospects for grid-connected solar PV in Kenya: A systems approach. *Applied Energy*, *161*, 583–590.

- Royne, A., Dey, C., & Mills, D. (2005). Cooling of photovoltaic cells under concentrated illumination: A critical review. *Solar Energy Materials and Solar Cells*, 86(4), 451–483.
- Saima Siouane, Slaviša Jovanović, & Philippe Poure. (2016). A Novel Identification Method of Thermal Resistances of Thermoelectric Modules Combining Electrical Characterization Under Constant Temperature and Heat Flow Conditions. *Transactions On Environment And Electrical Engineering*, 1(4)
- Samoita, D., Nzila, C., Østergaard, P. A., & Remmen, A. (2020). Barriers and Solutions for Increasing the Integration of Solar Photovoltaic in Kenya's Electricity Mix. *Energies*, 13(20), 5502.
- Saqr, K. M., Mansour, M. K., & Musa, M. N. (2008). Thermal design of automobile exhaust based thermoelectric generators: Objectives and challenges. *International Journal of Automotive Technology*, 9(2), 155–160.
- Sargunanathan, S., Elango, A., & Mohideen, S. T. (2016). Performance enhancement of solar photovoltaic cells using effective cooling methods: A review. *Renewable and Sustainable Energy Reviews*, 64, 382–393. <https://doi.org/10.1016/j.rser.2016.06.024>
- Sark, W. G. J. H. M. van. (2011). Feasibility of photovoltaic – Thermoelectric hybrid modules. *Applied Energy*, 88(8), 2785–2790.
- Selvan, K. V., Hasan, M. N., & Mohamed Ali, M. S. (2019). State-of-the-Art Reviews and Analyses of Emerging Research Findings and Achievements of Thermoelectric Materials over the Past Years. *Journal of Electronic Materials*, 48(2), 745–777.

- Shen, Z.-G., Tian, L.-L., & Liu, X. (2019). Automotive exhaust thermoelectric generators: Current status, challenges and future prospects. *Energy Conversion and Management*, *195*, 1138–1173.
- Soliman, A. M. A., Hassan, H., Ahmed, M., & Ookawara, S. (2020). A 3d model of the effect of using heat spreader on the performance of photovoltaic panel (PV). *Mathematics and Computers in Simulation*, *167*, 78–91.
- Soltani, S., Kasaeian, A., Sarrafha, H., & Wen, D. (2017). An experimental investigation of a hybrid photovoltaic/thermoelectric system with nanofluid application. *Solar Energy*, *155*, 1033–1043.
- Tang, Z. B., Deng, Y. D., Su, C. Q., Shuai, W. W., & Xie, C. J. (2015). A research on thermoelectric generator's electrical performance under temperature mismatch conditions for automotive waste heat recovery system. *Case Studies in Thermal Engineering*, *5*, 143–150.
- Temaneh-Nyah, C., & Mukwekwe, L. (2015). An investigation on the effect of operating temperature on power output of the photovoltaic system at University of Namibia Faculty of Engineering and I.T campus. *2015 Third International Conference on Digital Information, Networking, and Wireless Communications (DINWC)*, 22–29
- Tina, G. M., & Abate, R. (2008). Experimental verification of thermal behaviour of photovoltaic modules. *MELECON 2008 - The 14th IEEE Mediterranean Electrotechnical Conference*, 579–584.
- Trapani, K., & Redón Santafé, M. (2015). A review of floating photovoltaic installations: 2007-2013: A review of floating photovoltaic installations. *Progress in Photovoltaics: Research and Applications*, *23*(4), 524–532.

- UNEP. (1981). *New and renewable sources of energy*. 878501 UN conference on new and renewable sources of energy 1981, Nairobi, Kenya.
- Wang, R., Wang, J., & Yuan, W. (2019). Analysis and Optimization of a Microchannel Heat Sink with V-Ribs Using Nanofluids for Micro Solar Cells. *Micromachines*, *10*(9), 620.
- Xu, Y., X., Y., & Yang, L. (2015). Full-spectrum photon management of solar cell structures for photovoltaic–thermoelectric hybrid systems. *Energy Conversion and Management*, *103*, 533–541.
- Yadav, N., Gupta, M., & Sudhakar, K. (2016). Energy assessment of floating photovoltaic system. *2016 International Conference on Electrical Power and Energy Systems (ICEPES)*, 264–269.
- Yang, R. L., Tiepolo, G. M., Tonolo, É. A., Urbanetz Junior, J., & Souza, M. B. de. (2019). Photovoltaic Cell Temperature Estimation for a Grid-Connect Photovoltaic Systems in Curitiba. *Brazilian Archives of Biology and Technology*, *62*(spe), e19190016.
- Yazawa, K., & Shakouri, A. (2016). Thermoelectric topping cycles with scalable design and temperature dependent material properties. *Scripta Materialia*, *111*, 58–63.
- Yin, E., Li, Q., & Xuan, Y. (2017). Thermal resistance analysis and optimization of photovoltaic-thermoelectric hybrid system. *Energy Conversion and Management*, *143*, 188–202. <https://doi.org/10.1016/j.enconman.2017.04.004>
- Zeraatpisheh, M., Arababadi, R., & Saffari Pour, M. (2018). Economic Analysis for Residential Solar PV Systems Based on Different Demand Charge Tariffs. *Energies*, *11*(12), 3271.

- Zhang, J., Xuan, Y., & Yang, L. (2014). Performance estimation of photovoltaic–thermoelectric hybrid systems. *Energy*, *78*, 895–903.
- Zhang, J., Zhai, H., Wu, Z., Wang, Y., Xie, H., & Zhang, M. (2020a). Enhanced performance of photovoltaic–thermoelectric coupling devices with thermal interface materials. *Energy Reports*, *6*, 116–122.
- Zhang, J., Zhai, H., Wu, Z., Wang, Y., Xie, H., & Zhang, M. (2020b). Enhanced performance of photovoltaic–thermoelectric coupling devices with thermal interface materials. *Energy Reports*, *6*, 116–122.
- Zhang, T., Wu, S., Yang, R., & Zhang, G. (2017). Graphene: Nanostructure engineering and applications. *Frontiers of Physics*, *12*(1), 127206.
- Zhang, X., & Zhao, L.-D. (2015). Thermoelectric materials: Energy conversion between heat and electricity. *Journal of Materiomics*, *1*(2), 92–105.
- Zhou, J., Yi, Q., Wang, Y., & Ye, Z. (2015). Temperature distribution of photovoltaic module based on finite element simulation. *Solar Energy*, *111*, 97–103.
- Zhou, J., Zhang, Z., Liu, H., & Yi, Q. (2017). Temperature distribution and back sheet role of polycrystalline silicon photovoltaic modules. *Applied Thermal Engineering*, *111*, 1296–1303.
- Zoui, M. A., Bentouba, S., Stocholm, J. G., & Bourouis, M. (2020). A Review on Thermoelectric Generators: Progress and Applications. *Energies*, *13*(14), 3606. <https://doi.org/10.3390/en13143606>

APPENDICES

Appendix I: Contribution of the Thesis

1.7.1 Patents Applied

- Patent application for the “Enhanced Photovoltaic and Thermoelectric Power Generator” at “*Kenya Industrial Property Institute-Nairobi*” KE/P/2021/3788. Applied in January 2021, paid for on 16th February 2021 and corrections on the defects to the patent application submitted on 15th March 2021 to Kenya Industrial Property Institute-Nairobi. The payment for publication of the patent was made on June 14th 2021.

1.7.2 Journal Papers

1. Gideon Kidegho, Robert Kinyua, Christopher Muriithi, Francis Njoka, “*Innovative Solar Photovoltaic and Thermoelectric Power Generator for a Recirculating Aquaculture System*” Published by IJRER Vol. 10, No 3, 2020
2. Gideon Kidegho, Francis Njoka, Christopher Muriithi, Robert Kinyua, “*Evaluation of Thermal Interface Materials in Mediating PV Cell Temperature Mismatch in PV-TEG Power Generation*” Published by Elsevier Energy Reports Vol. 7 (2021) 1636–1650

1.7.3 Conference Papers

1. Gideon Kidegho, Robert Kinyua, Christopher Muriithi, Wolfgang Hornig, “*Enhancement of Solar Photovoltaic (PV) Power Generation Efficiency Using Thermoelectric Generator (TEG) Modules*” 2018 Annual Sustainable Research and Innovation (SRI) Conference.
2. Gideon Kidegho, Robert Kinyua, Christopher Muriithi, “*The Benefits of Cooling Solar Photovoltaic Modules and TEG for Efficient Power Generation in Battery Charging Systems*” 14th JKUAT conference 2019

Appendix II: Instruments Sensors and Components

During the preliminary data collection at JKUAT-IEET various instruments, sensors and electrical components were used in different locations and for different applications. Some instruments and sensors were physically mounted to collect continuous data while others were used every time a specific setup is fabricated. The main instruments used are presented.

B.1 Data Loggers

A COMBILOG 1022 data logger from Theodor Friedrichs & Co. was used for the 24-hour irradiance and ambient temperature measurements. The same data logger was used for measurement of PV module back plate temperature. Figure A1 shows the Data logger wall mounted at the JKUAT-IEET site on one of the laboratory walls. The KEYENCE NR500 data logger in Figure B 2 was used for specific setups daily data collection.



Figure B 1. COMBILOG 1022 Data logger

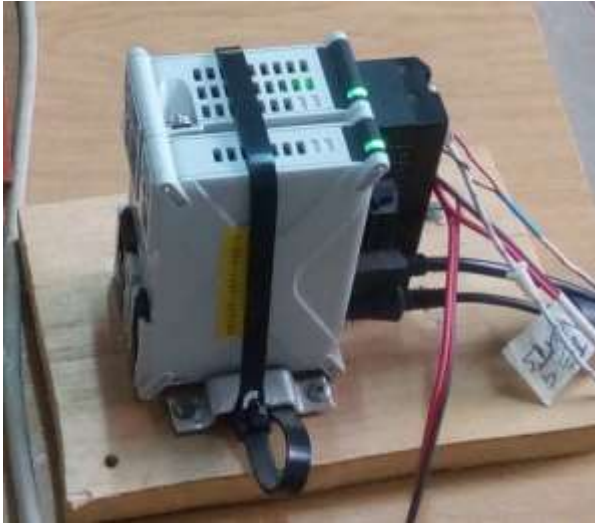


Figure B 2. KEYENCE NR500 Data logger

B2. Pyranometer

A model CMP-3 Pyranometer from KIPP & ZONEN was used for the measurement of irradiance. The pyranometer was factory calibrated by Theodor Friedrichs & Co. to a sensitivity of $11.94 \mu\text{V}/\text{W}/\text{m}^2$ as per the calibration certificate supplied. Figure B 3 shows the pyranometer used for measuring the irradiance data.



Figure B 3. CMP-3 Pyranometer

B 3 Thermocouples

Ambient and PV module temperatures for the weather station were measured using thermocouple sensors type PT 100 and the data was logged using the COMBILOG 1022 data logger. Figure A4 shows one of the K-type thermocouples used in the specific setups (SS).



Figure B 4. K-type thermocouples

B 4 Solar Power Meter

For spot irradiance measurements, a hand-held solar power meter TENMARS TM-208 was used. Figure B 5 shows the meter in use on site.



Figure B 5. TENMARS solar power meter

B 5 Thermometers

For spot PV cell temperature measurements, a hand-held A&D infrared thermometer type AD-5615 was used and for water temperature measurements, a hand-held mercury thermometer was used. The AD-5615 infrared thermometer is shown on Figure B 6 in use measuring the PV module surface temperature on site.



Figure B 6. Infrared thermometer

B 6 Multi-Meters

Multi-meters were used to make spot measurements of AC/DC current and voltage and also confirm component values like resistors, continuity and insulation. Figure B 7 shows one of the multi-meters used in the measurements.



Figure B 7. HIOKI 3287 Multi-meter

B 7 Photovoltaic Module

Table B 1 shows the technical specifications of the type of photovoltaic module that was used. This module appears on Figure B 6

Table B 1. Specifications of the PV module

Manufacturer	Ubbink East Africa Ltd	
Performance	At 1000 W/m ² and 25 °C	
Parameter		Values/Units
Number/type of cells	Polycrystalline	36-cells
Maximum power	P _{mPP}	13 Watts
Open circuit voltage	V _{oc}	21.6 Volts DC
Maximum voltage	V _{max}	18.0 Volts DC
Maximum current	I _{max}	0.75 Amperes DC
Short circuit current	I _{sc}	0.80 Amperes DC

System voltage	V_s	715 Volts DC
Fuse rating	F	2 Amperes

B 8 Thermoelectric Generator Module

The thermoelectric generator type used is shown in Figure B 8 and the technical specifications of the thermoelectric generator are presented in Table B 2.



Figure B 8. Thermoelectric generator Module

Table B 2. Thermoelectric generator specifications

SP1848 -27145 SA L*W*H = 40mm*40mm*3.4mm		
Δt	V_{oc} in Volts	I in mA
20°C	0.97	225
40°C	1.8	368
60°C	2.4	469

80°C	3.6	558
100°C	4.8	669

B 9 Aluminum ALUCORE Honey Comb Cooling Panel

The honey comb aluminum cooling panel was used for cooling the PV modules. The cobweb aluminium cooling panel is manufactured using stiff aluminium material ‘Alucore’, by BPE -3A composites GmbH’ in Germany. The Alucore cooling panel is used while clamped to the back plate of the PV using aluminium brackets to avoid any reaction with the cooling water. The cooling panel has a section thickness of 65 mm enough to make the PV module plus the cooling panel clamped together to be buoyant in a water. Figure A 9 shows a cut section and the cooling panel ready for clamping on the PV-PVF back plate.



Figure B 9. Alucore cooling panel (RHS) ready for mounting

B 10 Additional Meters Used on Site and the sample PV module

Figure B 10 shows an additional multi-meter that are used on site besides the ones brought from JKUAT. Figure B 11 shows a voltmeter being used on site. These instruments are mainly used for specific setups to make spot measurements of AC/DC current and voltage. Figure B 12 shows the manufacturers' specifications as indicated on the PVF back sheet of the design size PV module selected.



Figure B 10. Multi-meter Type VOLT-CRAFT-VO220



Figure B 11. Voltmeter Type VOLT-CRAFT PM-60-A



Figure B 12. Design Size Sample PV Module Specifications -Nyalenda Kisumu

Appendix III: Heat Spreader Catalogue Extract

PH3n

High Performance Heat Spreader

Features

Gives a typical junction temperature reduction of 20°C

Gives design flexibility

Die cut for custom shapes

Applications

Electronic components: IC / CPU / MOS

LED / M/B / P/S / Heat Sink / LCD-TV / Notebook PC / PC / Telecom Device / Wireless Hub etc....

DDR II Module / DVD Applications / Hand-Set applications etc...

REACH Compliant

RoHS Compliant

Properties

Property	PH3n			Test Method	Unit
Colour	Black	Black	Black	Visual	-
Thickness	0.062	0.07	0.1	-	mm
Metal layer	CU foil	CU foil	CU foil	-	-
PET layer thickness	0.025	0.025	0.025	ADTM D374	mm
Coating layer thickness	0.025	0.025	0.025	-	mm
Metal layer thickness	0.012	0.02	0.02	-	mm
Filler	Nano tube	Nano tube	Nano tube	-	-
Application temperature	-30 to 120	-30 to 120	-30 to 120	-	°C
Short time temp. @ 30sec	200	200	200	-	°C
Low molecular weight Siloxane content	0	0	0	-	ppm
Heat emissivity coefficient	0.96	0.96	0.96	ADTM D149	1

Dielectric strength (AV)	>2	>2	>2	ADTM D149	kV
Metal layer thermal conductivity	400	400	400	ADTM D5470	W/mk
Coated layer thermal conductivity	1.2	1.2	1.2	ADTM D5470	W/mk

1. Part Number

2. Size X-Y-Z

PH3n 15 20 0.062/0.07

Tel: +44 20 8133 2062 Email: sales@tglobaltechnology.com Web: www.tglobaltechnology.com Skype: tglobal. technology

Appendix IV: Coefficients of Linear Thermal Expansion for some common materials:

ENGINEERING TOOLBOX Site visited 6th October 2020-16.00hrs

Product	Linear Temperature Expansion Coefficient - α - ($10^{-6} m/(m\ ^\circ C)$)	
	ABS (Acrylonitrile butadiene styrene) thermoplastic	72 - 108
ABS -glass fiber-reinforced	31	
Acetal - glass fiber-reinforced	39	
Acetals	85 - 110	
Acrylic	68 - 75	
Alumina (aluminium oxide, Al ₂ O ₃)	8.1	
Aluminum	21 - 24	
Aluminum nitride	5.3	
Amber	50 - 60	
Antimonial lead (hard lead)	26.5	

- $10^{-6} m/m^\circ C = 1 \mu m/m^\circ C$
- $m/m = \text{meter per meter, in/in} = \text{inches per inches}$

Most values for **temperature** 25 °C (77 °F). The span in the values may be caused by the variation in the materials themselves - or by the variation in the sources used.

Appendix V: Graphite Sheet Technical Specifications

TFO-S-CB consists of more than 98% pure natural graphite. Due to the flake-like shape they show anisotropic

Thermal conductivities in-plane (x-y-plane) and in through direction (z-direction). Their softness allows for a good compliance to the contact surfaces. Thus, the total thermal resistance is minimized. Their low densities compared to copper (15%) or aluminum (50%) make them ideal for applications where low weight is required. The very high temperature resistance allows for the use in extreme hot environments.

Measurement technique according to: 1ASTM D 5470. All data without warranty and subject to change. Please contact us for further data and information.

Shelf life adhesive: 6 months when stored in original packaging at room temperature and 50% relative humidity.

Thicknesses: 0.13 mm / 0.25 mm / 0.5 mm

GRAPHITE FOIL TFO-S-CB

Anisotropic

PROPERTIES

Maximum contact through good surface compliance, very low weight, silicone-free, very high temperature resistance, EMI-shielding through high electrical conductivity

Optional with/without UL VO

AVAILABILITY

Sheet 300 x 500 mm

Roll 300 mm x 50 m

Non adhesive

(TFO-SXXX-CB)

Die cut parts

Sheet 457 x 609 mm

Roll 609 mm x 50 m

Adhesive on one side

(TFO-SXXX-CB-UL-A1)

Die cut parts

With UL VO

(TFO-SXXX-CB-UL)

APPLICATION EXAMPLES

Thermal link of:

CPUs to heat sinks

Power modules

Semiconductors

IGBTs

For use in Power inverters /

Laptops / Automotive power

Supplies /Industrial PCs

Rth vs. N/cm² (PSI)

TFO-S-CB

0.0

0.1

0.2

0.3

0.4

0.5

0.6

0 20 40 60 80 100

N/cm²

0.13 mm

0.25 mm

0.50 mm

PSI

0 20 40 60 80 100 120 140

Rth [°C-inch²/W] mm

PSI

0 20 40 60 80 100 120 140

Property Unit TFO-S130-CB TFO-S250-CB TFO-S510-CB

Material Natural Graphite 98% Natural Graphite 98% Natural Graphite 98%

Colour Grey Grey Grey

Thickness mm 0.13 0.25 0.5

Hardness Shore A 85 85 85

UL Flammability UL 94 V0 (for TFO-S130-CB-UL) V0 (for TFO-S250-CB-UL) V0 (for TFO-S510-CB-UL)

RoHS Conformity 2011 / 65 / EU Yes Yes Yes

Thermal

Resistance1 @ 150 PSI °C-inch²/W 0.06 0.10 0.16

Resistance1 @ 30 PSI °C-inch²/W 0.09 0.16 0.23

Resistance1 @ 10 PSI °C-inch²/W 0.12 0.24 0.40

Thermal Conductivity

(Z Direction)

W/mK 8, 8, 8

Thermal Conductivity

(X-Y Direction)

W/mK 140, 140, 140

Operating Temperature Range °C - 250 to + 400 - 250 to + 400 - 250 to + 400

Electrical

Volume Resistivity Ohm - cm 11.0×10^{-4} 11.0×10^{-4} 11.0×10^{-4}

Dielectric Constant @ 1 MHz < 0.001 < 0.001 < 0.001

Appendix VI: Kenya Electricity Schedule of Tariffs 2018

"Units Purchased": means electricity measured in kWh generated by the Company's Power Plants or Electric Power Producers Power Plants delivered to and purchased by the Company;

PART II

SCHEDULE OF NON-FUEL TARIFFS FOR ELECTRICAL ENERGY SUPPLIED BY THE COMPANY

Part II -Effective from 1st July 2018

The Tariffs to be applied by the Company for the supply of electrical energy from both the Interconnected System and the Off-Grid Systems, in each Post-paid Billing Period or Pre-paid Units Purchase Period shall be as detailed below:

METHOD DC-LIFELINE: Applicable to Domestic Consumers for supply provided and metered by the Company at 240 or 415 volts and whose consumption does not exceed 10 Units per Post-paid Billing Period or Pre-paid Units Purchase Period.

- a) Energy charges of KSh.12.00per Unit for Units consumed;

METHOD DC-ORDINARY: Applicable to Domestic Consumers for supply provided and metered by the Company at 240 or 415 volts and whose consumption is greater than 10 units but does not exceed 15,000 Units per Post-paid Billing Period or Pre-paid Units Purchase Period.

- a) Energy charges of KSh.15.80per Unit for Units consumed;

METHOD SC: Applicable to non-domestic Small Commercial Consumers for supply provided and metered by the Company at 240 or 415 volts and whose consumption does not exceed 15,000 Units per Post-paid Billing Period or Pre-paid Units Purchase Period.

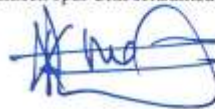
- a) Energy charge of KSh.15.60per Unit for all Units consumed.

METHOD CII: Applicable to Commercial and Industrial Consumers for supply provided and metered by the Company at 415 volts three phase four-wire and whose consumption exceeds 15,000 Units per Post-paid Billing Period.

- a) Energy charge of KSh.12.00 per Unit consumed.
- b) Energy charge of KSh.6.00 per unit for supply metered during off-peak hours as prescribed in Note 2.
- c) Demand charge of KSh. 800.00 per kVA.

METHOD CI2: Applicable to Commercial and Industrial Consumers for supply provided and metered by the Company at 11,000 volts, per Post-paid Billing Period.

- a) Energy charge of KSh.10.90per Unit consumed.



3